2018

Thermal Solitary Waves

Simon A. Louis
University of Wollongong

UNIVERSITY
OF WOLLONGONG
AUSTRALIA

Thermal Solitary Waves

Simon A. Louis

This thesis is presented as part of the requirements for the conferral of the degree:

Doctor of Philosophy

Supervisors:
Prof. Tim Marchant, Prof. Noel Smyth

The University of Wollongong
School of School of Mathematics and Applied Statistics

August, 2018

This research has been conducted with the support of an Australian Government Research Training Program Scholarship.

Declaration

I, *Simon A. Louis*, declare that this thesis is submitted in partial fulfilment of the requirements for the conferral of the degree *Doctor of Philosophy*, from the University of Wollongong, is wholly my own work unless otherwise referenced or acknowledged. This document has not been submitted for qualifications at any other academic institution.

Simon A. Louis

14th January 2019

Abstract

Optical solitary waves are supported in various nonlinear optical media. The mechanism for the formation of a solitary wave is a balance between nonlinear effects (which change the refractive index), and the dispersion or diffraction of the beam. In thermal media the nonlinearity arises due to the temperature dependent refractive index of the material. The optical beam heats the material and causes an increase in temperature, which changes the refractive index. Heat flux via the cell boundaries can also heat the medium, representing a different mechanism for changing the refractive index. The amplitude, position and stability of the solitary wave may all be changed by altering the boundary temperatures and other parameters. One dimensional solitary waves are stable for all parameter choices. As the medium is nonlocal the temperature response of the material extends far beyond the waist of the optical beam, which can stabilise two dimensional solitary waves for some parameter choices.

In Chapter 1 we review the literature on optical solitary waves, including an overview of different types of solitary waves and the various nonlinear media that support solitary waves. We derive the governing system of equations for an optical beam travelling in a nonlinear thermal medium, and provide an outline of the work undertaken in this thesis.

In Chapter 2 we outline three different numerical schemes for finding steady state solutions of the governing equations, including imaginary time evolution methods and Newton-conjugate gradient methods. Using the one-dimensional case we investigate various options for implementing these schemes, including using different order spatial discretizations, preconditioning matrices and stopping conditions. We find that the Newton-conjugate gradient method is the quickest and most stable method for this application.

In Chapter 3 we calculate and characterize steady state solitary waves in a nonlinear thermal medium, for both the one-dimensional and two-dimensional forms of the governing equations. We demonstrate that fundamental and higher order solitary wave types are able to be found using the Newton conjugate gradient method. We find that applying different temperatures at the cell boundaries causes the steady state solitary wave to migrate towards the warmer cell boundary(s). Adjusting the heat loss at the boundaries also affects the steady state position of the beam, with the beam migrating towards boundaries with lower heat loss. For the one dimensional case we find the amplitudes and positions of the steady state solitary wave in the parameter space of cell boundary temperatures and Biot-numbers. For the two dimensional case we provide diagrams showing the amplitude and position of the steady state solution for different temperatures at adjacent boundaries.

In Chapter 4 we investigate the stability of the steady state solitary wave solutions using three approaches. We test for stability using the Vakhitov-Kolokolov criterion, by performing a spectral stability analysis, and by numerical evolution of steady solitary waves perturbed by noise. We find that the fundamental steady state solution is stable for all parameter choices in the one dimensional case. The two dimensional solitary waves can be stable or unstable, depending on the combination of boundary temperatures and propagation constant. Smaller amplitude waves tend to be stable, while large amplitude waves are often unstable.

Understanding the behaviour of steady state solitary waves of this type may have applications in optical transmission, optical switching and optical computing, as the ability to exercise control over a solitary wave's position via the cell boundaries allows for information to be controlled within optical systems.

Acknowledgements

I would like to gratefully acknowledge the support of my supervisors, Tim Marchant and Noel Smyth. Undertaking a thesis part time while juggling family and work commitments has meant that progress has been slow at times, but Tim and Noel have been understanding and remained supportive and patient throughout. I would like to thank Tim for providing the opportunity to attend a conference on nonlinear waves in Marrakech, and to present the results from my first published paper at a conference in Beijing. Noel Smyth, from the University of Edinburgh, has provided valuable input and many comments on drafts of the two papers and this thesis.

This thesis would also not have been possible without the support of my family, and in particular my wife, Danielle Louis, who has been willing to provide me the time and space to work on it. Working around a full-time job as well as starting a family, has meant giving up nights and weekends at times and not being able to spend as much time with my children as I would like. Their patience and understanding means the world to me and I am extremely grateful and thankful for it.

Publications for this thesis

S.A. Louis, T.R. Marchant and N.F. Smyth. "2-D solitary waves in thermal media with non-symmetric boundary conditions". In: Stud. Appl. Math. (2018).

S.A. Louis, T.R. Marchant and N.F. Smyth. "Optical solitary waves in thermal media with non-symmetric boundary conditions". In: J. Phys. A.:Math. Theor. 46.055201 (2013).

Unrelated publications

S.A. Louis. "Gridded return values of McArthur Forest Fire Danger Index values across New South Wales". In: Aust. Meteorol. Ocean. 64(4), 243-260 (2014).

S.A. Louis. "A warm-front triggered nocturnal tornado outbreak near Kiama, NSW, Australia". In: J. So. Hemisph. Earth (forthcoming) (2018)

Contents

Chapter 1

Introduction

Solitary waves are a type of nonlinear dispersive wave which are unchanging in form and localized. The earliest observations of solitary waves were made in the nineteenth century in the context of fluid mechanics, by John Scott Russell, who first observed a solitary wave travelling on the surface of a Scottish canal [99]. At around the same time, George Stokes developed a theory describing the propagation of nonlinear periodic surface water waves, using a Taylor expansion around the flat non-perturbed surface [104]. The Stokes weakly nonlinear model was only applicable for small amplitude waves, and this theory could not explain the solitary waves observed by Russell. These could not be explained until later in the century, when nonlinear Boussinesq-type equations were developed that allowed for the description of solitary waves with long wavelength compared to the depth of the water [24]. This was further extended in the 1890s with the development of the Korteweg-de Vries (KdV) shallow water wave equation, which has exact solitary wave solutions. The non-dimensional form of the KdV equation is

$$u_t + 6uu_x + u_{xxx} = 0, \tag{1.1}$$

where u represents the height of the shallow water wave as it propagates in the spatial dimension x. The KdV equation is the generic integrable nonlinear dispersive wave equation [111], with the solitary wave solution being

$$u(x,t) = A\,\mathrm{sech}^2\,\frac{\sqrt{A}}{2}\,(x - 2At)\,. \tag{1.2}$$

Many other equations exhibiting solitary wave solutions were subsequently derived, some of them integrable. The key equation in the context of optical solitary waves is the nonlinear Schrödinger (NLS) equation

$$iu_t + \frac{1}{2}u_{xx} \pm |u|^2 u = 0, \tag{1.3}$$

which was first written down in the early sixties as an asymptotic reduction of Maxwell's equations [32]. The NLS equation models the evolution of the complex valued amplitude envelope of a plane wave propagating in a weakly nonlinear dispersive medium with a Kerr response. The NLS equation has two forms, the NLS+ equation where the sign of the nonlinear Kerr response is positive so that the nonlinearity is focussing, and the NLS- equation for a defocussing medium where the sign of the nonlinear response is negative. The NLS equation is a also a special case of the complex Ginzburg-Landau equation, which describes the amplitude evolution of waves near a threshold for instability. The Ginzburg-Landau equation first arose from earlier work in the fifties into superconductivity and superfluidity [46, 47]. One particularly important application for the NLS equation is modelling the transmission of solitary waves through nonlinear optical fibres, as introduced in a pair of seminal papers by Hasegawa and Tappert [50, 51] in the early seventies.

The NLS equation has found applications in many other physical contexts, including work in the late sixties on surface water waves where the water depth is large compared to the wavelength [117], and pressure waves in the atmosphere. An important finding in the late sixties was that periodic water waves of the form described by Stokes experience a type of instability, known as Benjamin-Feir instability or modulational instability (MI), where small perturbations at a frequency near the carrier frequency can exponentially grow via a transfer of energy from the main carrier frequency to the side bands [19, 20].

The NLS equation is exactly integrable via the inverse scattering method [118], so that solitary waves are unchanged on interaction with other solitary waves, apart from a shift in position and phase. Solitary waves with this property of elastic collisions are termed solitons.

In section 1.1 we will provide more detail on the NLS equation and review the early work into optical solitary waves, then briefly outline different types of solitary

waves in the literature. In section 1.2 we give an outline of some of the different nonlinear materials in which solitary waves have been discovered, while in section 1.3 we review the work that has been done on thermal nonlinear media, which is the application that we focus on in this thesis. In sections 1.4 and 1.5 we give a brief review of numerical methods used to study the NLS-type equations that support solitary waves and methods for analysing their stability. In section 1.6 we provide details of the form of the equations governing optical beams, propagating in a thermal medium, used throughout this thesis.

1.1 NLS Equation and Optical Solitary Waves

The potential for self-focussing optical solitary waves was first proposed in the early sixties. Askar'yan [12] proposed that a beam propagating in a dispersive medium with a nonlinear response would affect the polarization of the medium, which would in turn would affect the propagation of the beam. Chiao et al. [32] discussed various nonlinear mechanisms that could result in self-trapping, including high frequency Kerr effects, electrostriction and electronic polarisation, expressing a model for the propagation of a solitary wave in the form governed by the NLS equation.

In Kerr media the change in refractive index is proportional to the intensity of the wave, i.e. $n = n_0 + n_2|E|^2$, where n_0 is the refractive index in the absence of an electric field, n_2 is the nonlinear index of refraction and E is the electrical field of the optical beam. In this type of medium the nonlinearity is local in the sense that the change in refractive index does not extend far beyond the region in which the optical beam is propagating.

The electromagnetic wave equation describes the propagation of optical waves through any medium, and derives directly from Maxwell's equations on certain assumptions. In homogenous media, for which the index of refraction is uniform, this is a linear wave equation which can not support solitary waves. The local nature of solitary waves requires a superposition of component wave frequencies, and dispersion or diffraction will result in these component waves travelling at different velocities. In Kerr media the dependence of the refractive index on the electrical

beam intensity results in a modified form of the electromagnetic wave equation [59]

$$\nabla^2 \overrightarrow{E} - \frac{\epsilon_0}{c^2}\frac{\partial^2 \overrightarrow{E}}{\partial t^2} - \frac{\epsilon_2}{c^2}\frac{\partial^2 |E|^2 \overrightarrow{E}}{\partial t^2} = 0, \tag{1.4}$$

where the electric field vector can be expressed as $\overrightarrow{E} = \frac{1}{2}(E'(x,y,z)e^{\imath(kz-\omega t)} + c.c.)$, E' is the slowly varying envelope of the electric field and $e^{\imath(kz-\omega t)}$ represents the carrier wave. Substituting this into (1.4), eliminating higher order terms, assuming that the second derivative in z can be neglected (the paraxial approximation [111]), and putting in non-dimensional form, we obtain the NLS equation

$$\imath\frac{\partial E}{\partial z} + \frac{1}{2}\nabla^2 E \pm |E|^2 E = 0, \tag{1.5}$$

where E is the complex valued envelope of optical electric field. The Laplacian in the NLS equation represents the group velocity dispersion and the cubic term represents the Kerr nonlinearity, where this can be focussing or nonfocussing. For Kerr media there are no stable solutions for the (2+1)-D form of the equation, but stable solutions exist in the (1+1)-D geometry.

The (1+1)-D form of the NLS+ equation has an exact solution via the inverse scattering method [118], with four free constants describing the amplitude, velocity, center coordinate, and phase. Zakharov and Shabat [118] found the simplest form of this exact solution [50]

$$E(x,t) = \eta \,\mathrm{sech}\left(\eta(x - x_0 + 2\xi z)\right) e^{-\imath(\xi x + (\xi^2 - \eta^2)z + \phi}, \tag{1.6}$$

where η is the amplitude, ξ gives the velocity, x_0 is the centre coordinate and ϕ is the phase. In a subsequent paper Zakharov and Shabat [119] provided the analytic solution for the NLS- equation (a defocussing medium),

$$E(x,t) = \eta \tanh\left(\eta x\right) e^{2\imath\eta^2 z}, \tag{1.7}$$

and examined soliton interactions and collisions in this regime, noting that in this case solitons behave like repelling one-dimensional particles.

In general the propagation of an optical solitary wave requires an input beam to be over a critical power threshold, or else the nonlinear focussing response will

be insufficient to overcome the natural dispersion of the beam [4]. For the NLS equation this critical power threshold is shown by the inverse scattering analytic solution, as a discrete eigenfunction exists only if the initial beam power is over a critical threshold. Chiao et al. [32] provided a table of nonlinear coefficients of refraction and critical beam powers for self-trapping in a number of different optical materials.

Lallemand and Bloembergen [68] performed early experiments with self-focussing laser beams in liquids, providing experimental comparisons against predicted results. Kelley [59] examined the case where the self-focussing mechanism is not offset by diffraction, so that the (2+1)-D radially symmetric solitary wave in a Kerr media is unstable, and that self-focussing would lead to an unbounded increase in beam intensity and subsequent filamentation of the beam as the nonlinearity saturates. An early analysis of this filamentation process presented by Bespalov and Talanov [21] shows that the filamentations develop from perturbations of the beam with wavenumber below a critical threshold, and that the power of these filamentations does not depend on the input beam power. As a result, as the input beam power increases it is the number of filamentations rather than the intensity of the filament beams that increases. Akmanov et al. [4] provided an early analysis of the self-focussing and self-trapping of light in a generic non-linear material, using a stationary solution approximation. The paper focussed on the low-inertia nonlinear electronic polarization and high-frequency Kerr effect mechanisms, and identified a critical power above which self-focussing could occur, as well as a relationship between the optical beam power and the focal cross-section of the beam.

Khokhlov [60] gave an overview of the various combinations of nonlinear wave equations arising in dispersive and non-dispersive systems, and dissipative or focussing nonlinearities. After this early work in the sixties and seventies this self-focussing mechanism was subsequently studied in a wide variety of different contexts, such as Bose-Einstein condensates (see [105] for a review of bright solitons in BECs) and biological suspensions [23], and found a number of unusual applications, such as focussing of gravitational waves [86]. One interesting recent application of a coupled NLS-Poisson equation is in the field of dark matter, where it has been proposed that solitons of dark matter particles can form [48]. In this dark matter framework the

Poisson equation describes the gravitational field and the NLS equation describes a BEC of axion particles. Paredes and Michinel [87] examined the interaction dynamics of these dark matter soliton, finding that these led to effective forces that could potentially be resolved in astrophysical observations, regardless of the interactions between the dark matter constituent particles. This model allows for the possibility of laboratory simulation of the dark matter solitons with nonlinear optical materials.

In an important piece of work Suter and Blasberg [106] showed that media where the response of the refractive index to the optical beam extended beyond the region of the beam, termed a nonlocal response, could act to stabilise (2+1)-D solitary waves, which otherwise break up into filaments. They demonstrated this both numerically and experimentally using an optical beam propagating in atomic sodium vapour, where the nonlocal response derives from diffusion of the sodium atoms. Research into various other optical media supporting solitary wave propagation will be covered in the following subsections.

1.1.1 Other Solitary Wave Types

Most of the initial work into the transmission of solitary waves focussed on so-called bright solitons, where the Kerr nonlinearity is self-focussing and acts against the dispersion of the wave to support a pulse of high optical intensity relative to the background. However, from the seventies onwards a range of other optical solitary wave forms were identified.

Another type of solitary wave that arises as an analytic solution of the NLS equation is a grey or dark soliton, which is a local region of low optical intensity against a bright uniform background intensity. Hasegawa and Tappert [51] provided analytic solutions for (1+1)-D dark solitons propagating in a nonlinear optical fibre with normal dispersion, noting that there was a fundamental solution where the amplitude drops to zero (a black soliton), and a more general family of grey solitons where the minimum amplitude is non-zero.

Tomlinson et al. [108] numerically simulated the propagation of dark solitons of even and odd type on a broader, but finite width background pulse, for a (1+1)-D optical fibre geometry. As the medium was defocussing, the bright background pulse experienced rapid diffraction. However, the modelled dark solitons retained

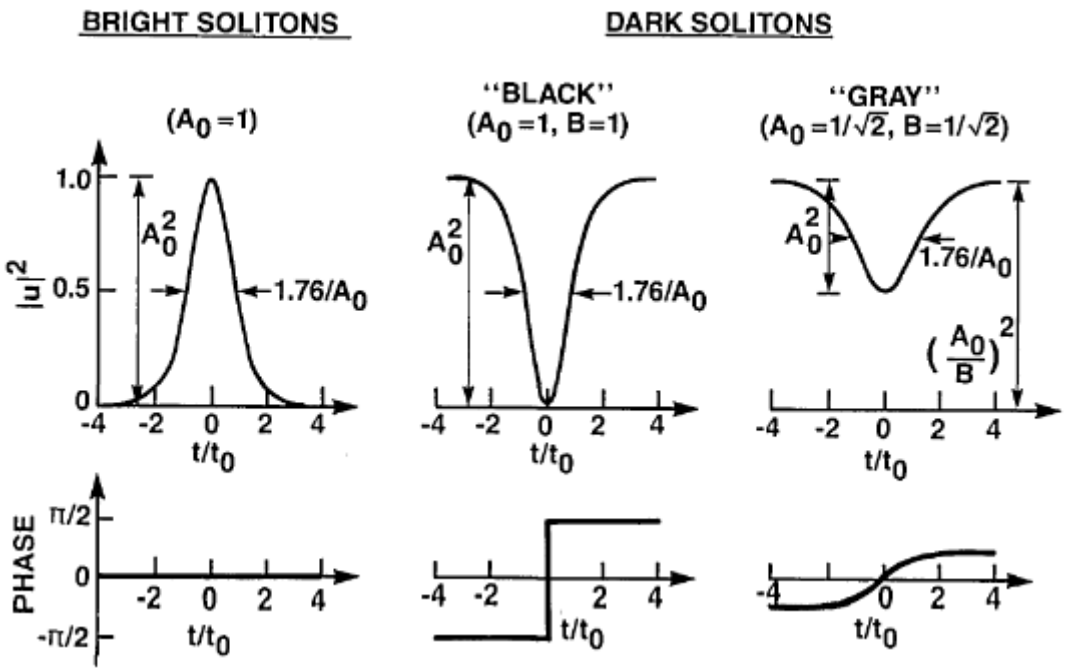

Figure 1.1: Figure 1 from Tomlinson et al. [108] - intensity and phase as functions of normalized time for bright and dark solitons.

enough of their energy through interaction with the background to propagate as a solitary wave. The dark solitary wave of even phase broadened but remained in the same position in the centre of the background pulse. The solitary wave with odd phase split into two grey solitons which migrated towards the edge of the broadening background pulse. Figure 1.1 (their Figure 1) shows the intensity and phase profiles for bright, dark and grey solitons propagating in an optical fibre, where A_0 represents the maximum intensity in the profile, B is a parameter determining the intensity minimum relative to A_0 and the x-axis is presented in units of normalised time. One key difference between bright and dark solitons is the non-uniform phase, with a change in sign at the point of minimum intensity for dark and grey solitons.

Swartzlander et al. [107] performed the first experiments demonstrating the stable propagation of dark spatial structures within a self-defocussing medium, using a mesh across the input beam to generate local intensity minima within an broad high-intensity input beam. In this case the widths of the minima patterns decreased even as the overall size of the high intensity output beam increased due to the combination of diffraction and the defocussing nature of the material. Kivshar and Luther-Davies [63] give a detailed review of this early work on dark solitons.

Experimental observations of solitons also initially focussed on spatially coherent optical beams, where the phase is the same at any point of the beam cross-section. In contrast, a spatially incoherent optical beam will have a phase that varies randomly with position along the cross section, leading to a 'speckled' appearance. Mitchell et al. [83] performed an experiment in which a partially spatially incoherent input beam was generated and demonstrated self-trapping of the beam within a strongly nonlinear photorefractive medium. The key requirement is that the medium should have a slow nonlocal response time relative to the rate of change of the beam speckle pattern, so that small spatial scale waveguides do not develop. Subsequent experiments provided the first demonstration of a trapped completely incoherent 'white-light' solitary wave [84], and a demonstration of a incoherent dark soliton [31].

The fundamental soliton mode is characterised by a single wave structure. Higher order soliton structures are also possible, and can take a number of different forms, including vortex solitons, multipole and necklace solitons. Kruglov [66] outlined the possibility for stable beams with a circular intensity profile, where the phase of the beam possessed a rotating vortex structure. Quiroga-Teixeiro and Michinel [94] investigated the stability and behaviour of dark vortex solitary waves in a type of medium that simultaneously exhibits both focussing and nonfocussing responses to the refractive index. They identified a critical value of the propagation constant, both analytically and numerically, above which the vortex soliton would be stable and below which the beam would split into filaments. They also numerically simulated and classified elastic and destructive interactions between two dark vortex solitary waves of this type.

Desyatnikov et al. [38] introduced a class of solitons called azimuthons with a ring shaped intensity profile containing a number of local peaks and possessing angular momentum. The rotation of the intensity peaks arises from modulation of the energy flow along the ring, and can be suppressed to produce stationary multipole type solitons. Izdebskaya et al. [55] reported an experimental observation of a stably propagating two-component vector soliton, with one component wavelength a fundamental soliton and the other component a vortex at different wavelength, in a nematic liquid crystal medium. In isolation the vortex soliton broke up into

two solitary waves as the result of a mode 2 azimuthal instability. By propagating the components simultaneously, the fundamental soliton at higher powers was able induce a nonlocal potential in the nematic medium that stabilised the vortex. Buccoliero et al. [29] performed a numerical analysis showing that in a generalised Kerr-type medium with a Gaussian nonlocal response, a high degree of nonlocality would stop the azimuthal instabilities that tend to break up higher order solitons such as vortex and multipole solitons in media with a local nonlinearity.

1.2 Nonlinear Optical Materials

1.2.1 Optical Fibres and other Kerr Media

Solitary waves with a self-focussing nonlinearity can be temporal, balanced by dispersion, or spatial, balanced by diffraction. Optical fibres represent a space constrained (1+1)-D realisation of the NLS equation, with Kerr type nonlinearity, for which the solitary wave is of temporal type. Optical fibres are typically in the normal dispersion regime, where the local refractive index change is defocussing, and bright solitary waves are not possible. However, optical fibres in the anomalous dispersion regime can be manufactured. In this case, the defocussing influence is group-velocity dispersion of the optical pulse, with focussing provided by a local refractive index change proportional to the light intensity.

In a pair of papers Hasegawa and Tappert [50, 51] provided an analytical and numerical analysis outlining the potential for self-focussing to offset dispersive spreading of a optical pulse within a fibre, comparing with the linear case for which pulses disperse over time and interfere with each other. Examples were provided of both bright solitons in a medium with anomalous (self focussing) dispersion [50] and dark solitons in a normal (defocussing) fibre [51]. The effect of adding noise or absorption was investigated numerically and found to have no effect on soliton stability, while increasing the input power well above the amount required to balance the dispersion leads to oscillations of the pulse, and a break up into multiple solitons. Mollenauer et al. [85] performed an early experimental observation of temporal solitons (of both fundamental and higher orders) within a silica-glass optical fibre, and found good agreement with numerical results from the NLS equation [100]. As the laser power

was increased the output profile moved from a broad beam width resulting from dispersion alone, to a self-focussed narrow beam, to splitting into higher order soliton modes.

Maneuf et al. [74] showed experimentally that spatial (1+1)-D solitary waves can propagate in a planar waveguide with a liquid (CS_2) transmission medium, finding stable fundamental solitons, as well as higher order solitons up to the third order. The higher order solitons had oscillatory behaviour in the propagation direction, in agreement with the analytic solution. Aitchison et al. [2] performed a similar experiment in a glass Kerr-type medium for spatial solitons, demonstrating stable transmission of spatial solitary waves in a solid-state waveguide medium. They investigated the power levels required for self-focussing, finding quite high powers (100kW-1MW) were necessary, and measured the nonlinear response time, finding that this was in the order of picoseconds, and thus that the nonlinear mechanism was unlikely to be a thermal response.

Vanin et al. [110] analysed the Maxwell-Bloch equations and found that temporal type solitary wave structures can exist for group velocity dispersion balancing a Kerr nonlinearity. These dissipative solitary wave structures are self-accelerating, with a continuous shift towards greater group velocities, and their existence does not depend on the sign of the group velocity dispersion. Akhmediev et al. [3] provided an exact solution for another temporal type of dissipative soliton, where the nonlinearity is provided by the gain and loss within a laser cavity medium. In this case the solitary wave was co-located with the gradient of the absorption curve, and the existence of the solitary wave depended on the sign of the parameter defining amount of loss or gain on one side of the absorption curve. When this gain parameter is negative, solitary waves only exist when medium exhibits anomalous dispersion, and when the gain parameter is positive solitary waves exist for either normal or anomalous dispersion.

1.2.2 Photorefractive Media

In photorefractive media the focussing effect is produced by an internal dc field, which produces an anisotropic response in the refractive index. In dimensionless form the governing equations are the coupled system [65].

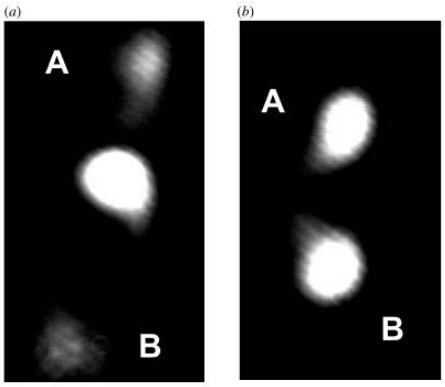

Figure 1.2: Figure 4 from Krolikowski et al. [65] - three soliton interaction demonstrating dependence on relative phase. $P_A = P_B = 0.4\mu W, P_C = 1.7\mu W$; a) relative phase between A and $C \approx \pi/2$; b) relative phase between A and $C \approx -\pi/2$.

$$\imath\frac{\partial E}{\partial z} + \frac{1}{2}\nabla^2 E + \frac{\partial \phi}{\partial x}E = 0, \quad \nabla^2\phi + \ln(1+|E|^2).\nabla(\phi) = \frac{\partial}{\partial x}\ln(1+|E|^2), \qquad (1.8)$$

where the electrostatic field is applied along the x axis, E is the complex valued envelope of the optical electric field and ϕ is the induced electrostatic potential.

Segev et al. [101] proposed a model for spatial solitons in a photorefractive medium and provided a prediction for the voltage range in which shape preserving solitons are possible. Duree et al. [41] performed the first observation of self-trapping of an optical beam in this type of medium, noting that the nonlocal nature of the response meant that solitons can be observed with much lower beam powers than in Kerr media. They observed that for some applied voltages the soliton shape was independent of the input power, and could thus maintain their profile when there was loss or gain in the media.

Krolikowski et al. [65] performed experiments aimed at understanding the interaction of coherent and noncoherent photorefractive solitary waves. They demonstrated that for the case of a small angle collision of coherent solitary waves, the interaction was inelastic, with in phase solitary waves consolidating into a single solitary wave and out of phase solitary waves repelling each other. They also demonstrated that the energy transfer associated with two solitary wave interaction could either create or destroy a third solitary wave in the region of the collision. For the case of incoherent solitary waves, they demonstrated that repulsive solitary wave in-

teraction was possible in contrast to most isotropic nonlinear media where incoherent solitary waves always experience attraction. Figure 1.2 (Figure 4 from [65]) shows an experimental demonstration of a three solitary wave interaction in a photorefractive medium. In Figure 1.2a the relative phase between the two side solitary waves and the central solitary wave is approximately $\pi/2$ and energy is transferred to the central solitary wave. In Figure 1.2b the relative phase is $\pi/2$ and energy is transferred from the central solitary wave to the side solitary waves, resulting in the annihilation of the central solitary wave.

1.2.3 Nematic Liquid Crystals

A nematic liquid crystal is a material consisting of rod shaped organic molecules which exhibit orientational, but not positional order, and which can rotate under the influence of an electric field due to the electric field inducing a dipole in the molecules [61]. This rotation increases the refractive index, so that self-focusing results and a bulk solitary wave, termed a nematicon, can then form [14]. Typical non-dimensional governing equations for nematicons are the coupled system [6]

$$\imath\frac{\partial E}{\partial z}+\frac{1}{2}\nabla^2 E+2E\theta=0,\ \nu\nabla^2\theta-2q\theta+2|E|^2=0, \tag{1.9}$$

where E is the complex valued envelope of optical electric field, θ is the nematic tilt angle (relative to a pre-tilt angle $\hat{\theta}$), ν is a parameter representing the medium elasticity, and q is related to the static electric field that pre-tilts the nematic dipoles. This form of the equation applies when the deviation of the tilt angle relative to the pre-tilt angle is small, i.e. $|\theta| \ll 1$. The pre-tilt angle, $\hat{\theta}$, is the tilt angle in the absence of the optical beam. This is usually experimentally achieved by the application of a static electric field, or by rubbing the boundaries of the cell, in which case $q = 0$.

Braun et al. [26] performed an experimental study on the self-focussing of a laser beam within a nematic liquid crystal, for both cylindrical and spherical cell geometries. Their experiments found that at large beam intensities undulation of the beam and filament structures were observed that could not be explained by the Kerr effect alone. McLaughlin et al. [79] used a paraxial model to replicate certain observed

behaviours of solitary waves in nematic liquid crystals in the (1+1)-D case, and were able to produce self-focussing, undulation and filamentation in numerical models of the system. Experiments have been performed demonstrating the practical applications of nematicons [35, 36] for optical transmission and switching [61, 62]. Peccianti et al. [89] made an observation of MI of a periodic wave travelling within a liquid crystal with a nonlocal response, finding a good fit between the observed maximally amplified harmonic and that predicted from theory. One particular complication for nematicons is that a minimum electric field is required to rotate the molecules (the Freedericksz transition). Peccianti et al. [92] investigated the transverse dynamics induced by this low frequency field experimentally and numerically, finding that this induced a transverse oscillation in the nematicon position. They also demonstrated that the input beam can be launched with a compensatory phase tilt that will eliminate the transverse beam motion. Peccianti et al. [90] showed experimentally that nematicons with different propagation angles relative to the cell axis can be generated by adjusting the voltage bias across the cell, and also demonstrated that filaments produced by MI under a voltage bias result in the filaments propagating at an angle. In a later paper Peccianti et al. [91] showed that solitons launched with a transverse momentum and sufficiently high beam power are able to escape from a trapping refractive index profile. Hutsebaut et al. [53] demonstrated the transmission of single component higher order soliton modes within a nematic planar waveguide.

The evolution of a solitary wave in a nonlocal medium is also affected by the boundaries of the cell, with the beam to cell width ratio a key parameter [5, 8]. For a biased nematic liquid crystal cell, for which the molecules are pre-tilted by an external electric field, the response of the molecules decays exponentially away from the beam, so the effect of the boundaries can be ignored in a cell which is wide compared with the beam width [36]. However, for an unbiased cell the response decays linearly in $(1 + 1)$-D and logarithmically in $(2 + 1)$-D, so the effect of the boundaries is important [5, 80].

1.2.4 Colloidal Media

In colloidal media, the nonlinear refractive index response is a result of an increase in the packing fraction (concentration) of nanometre sized colloidal particles in suspension. The increased concentration is due to electrostriction, which causes the nanoparticles to be attracted to the higher intensity part of the optical beam. Typical non-dimensional governing equations of solitary waves in colloidal media are [78]

$$\begin{aligned} &\imath\frac{\partial E}{\partial z} + \frac{1}{2}\nabla^2 E \pm (\eta - \eta_0)E = 0,\ |E|^2 \pm (g(\eta) - g(\eta_0)) = 0, \\ &g(\eta) = \frac{3-\eta^3}{1-\eta} + \ln(\eta) \end{aligned} \tag{1.10}$$

where E is the complex valued envelope of optical electric field, η is packing fraction of colloidal particles, η_0 is the unperturbed packing fraction, and $g(\eta)$ is a general function describing the compressibility. The form of g is from the common model for compressibility based on the Carnahan-Starling approximation [49].

Ashkin et al. [11] created an artificial Kerr media from a suspension of nanoparticles as a test bed for observing the self-focussing and self-trapping of laser beams, demonstrating the independence of the critical power from beam diameter for the first time. Yashin et al. [116] carried out an experiment to measure the beam width of a solitary wave within a suspension of spherical polystyrene nanoparticles, finding a beam width not much above the minimum predicted by theory. For a given particle concentration, saturation of the nonlinearity above a certain power threshold led to a lower bound on the observed solitary wave beam diameter.

Matuszewski et al. [78] proposed a model in which particle interaction is taken into account (via a hard sphere potential model), which can subsequently resolve the nonlinear behaviour in the high optical intensity regime and produce stable solitary waves. They provided an analytical and numerical analysis of the (1+1)-D model, showing that stable solitary waves are produced by the model and identified a region of bistability, i.e. where two stable solitons of the same power are possible. In a subsequent paper [77], this work was extended to look at the properties of the solitons on each stable branch, finding that for a given power the soliton on the upper stable branch much narrower in width, and tended to be more robust in collisions with

other solitons. Various modes of interactions between solitons including collision, deflection and switching between branches was investigated numerically.

Lee et al. [69] performed a diagnostic experiment to investigate which of a number of nonlinearity models showed best agreement, finding that including the effects of non-compressibility via the non-ideal gas model gave better results than exponential nonlinearity or Kerr nonlinearity. Marchant and Smyth [76] used a semi-analytical approach to find solutions for the colloidal system equations and investigated the stability of the (1+1)-D and (2+1)-D solitary waves, finding that for the (1+1)-D case there was a bistable region for low values of background packing fraction, in good agreement with earlier numerical work, and that in the (2+1)-D case there was one stable solution only above a critical power threshold for low background packing fraction. In both cases, increasing background packing fraction eliminated the unstable region.

1.3 Thermal Media

In a thermal medium the refractive index changes due to it absorbing thermal energy from the optical beam or the cell boundaries. The equations describing this system are an NLS-type equation describing the propagation of the optical wave, and a steady state thermal diffusion (Poisson) equation for the temperature [97]

$$2\imath k\frac{\partial E}{\partial z} + \nabla^2 E + 2k^2\frac{\beta\Delta T}{n_0}E = 0,\ \nu\nabla^2 T + |E|^2 = 0, \tag{1.11}$$

where E is the complex valued envelope of optical electric field, T is temperature of the thermal medium, n_0 is the unperturbed refractive index in the absence of the optical beam, k is the wavenumber of the optical beam, β is the thermal coefficient of the refractive index change and ν is the thermal diffusivity of the medium. There is a linear relationship between the change in temperature and the change in refractive index, $\Delta n = \beta\Delta T$. Further details of the thermal medium system equations are outlined in Section 1.6.

In thermal materials the refractive index of the material undergoes a nonlinear response that leads to the self-focusing (or defocusing) of the light beam, counter-balancing its natural diffraction (dispersion). For thermal media, the response of

the material to the light beam extends far beyond the beam, as measured by its width, termed waist in optical applications [36], the response then being termed nonlocal. This nonlocal response is due to the nonlinear optical response of the medium being coupled to a heat-diffusion equation, which is elliptic [1]. This elliptic medium response means that the medium responds over the entire domain, not just in the vicinity of the optical beam. The nonlocal response can also arrest the usual catastrophic collapse of $(2+1)$-D solitary waves governed by NLS-type equations [62], where self-focussing leads to an unbounded increase in the amplitude of the wave over a finite distance (or time). Bang et al. [16] examined the case of a general nonlocal NLS type equation and proved that for all physically reasonable nonlocal response functions collapse was prevented in all dimensions.

Litvak [70] proposed the mechanism by which self-focussing within a material based on heating of the material can be achieved. For bright solitary wave propagation within a thermal medium the key requirement is that the index of refraction increases with increasing temperature. He provided an analysis on the quasilocal case, where the time of the laser pulse is much shorter than the time in which heat conduction within the medium reaches a quasi-equilibrium state. Dabby and Whinnery [37] performed an early experiment demonstrating the propagation and self-focussing of an argon laser beam through a lead glass thermal medium, obtaining photographs of the trapped solitary wave.

Carman et al. [30] performed an experiment in a Neodymium doped thermal glass medium, focussing on measuring the transient response and finding that the beam diameter decreased approximately linearly before reaching a minimum of around $65ms$. Thermal conduction allowed an equilibrium steady state temperature profile to be reached in the order of one second or less. Litvak et al. [71] performed a numerical analysis of the steady-state response of a wave within a weakly ionised plasma with thermal nonlinear response, looking at the characteristics of the resulting optical beam and conditions for instability in the nonlocal case. Dreischuh et al. [40] performed experimental measurements of (dark) optical vortex solitons within a self defocussing thermal medium, finding that saturation of the nonlinearity was able to reduce, but not eliminate, the azimuthal instability.

Rotschild et al. [97] demonstrated the first experimental observations of stable

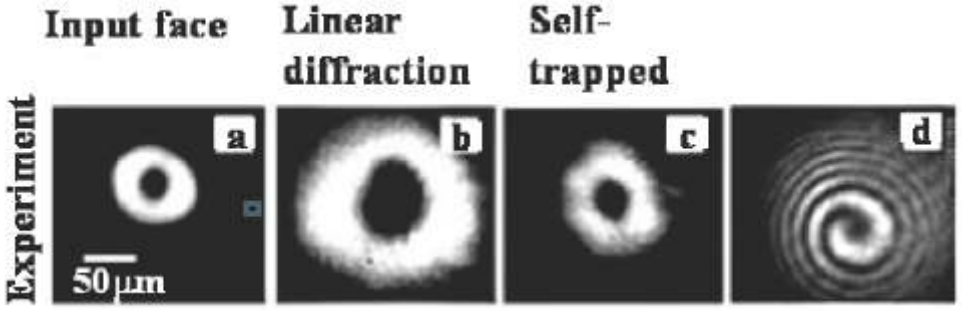

Figure 1.3: Figure 4 from Rotschild et al. [97] - experimental results showing a) input vortex beam, b) diffracted output beam at low power after 28 mm propagation, c) output soliton beam at high power, and d) the vortex phase structure of the output soliton.

vortex solitons in a thermal medium, and also showed that rectangular cell geometries would lead to elliptic solitons in response to an input circular beam. Figure 1.3 (their Figure 4) shows observed results from an experiment with a 488nm laser beam passing through a lead glass thermal medium. The left plate shows the shape of the input laser beam, while the middle two plates show the shape of the beam after propagating 28 mm through the lead glass. For a low power (10 mW) input (b) the nonlinear response is insufficent to overcome the diffraction and the beam grows in size and becomes more diffuse, while for a high power (1 W) input (c) self-trapping means that the beam approximately maintains its size and shape.

Barsi et al. [17] performed experiments on a liquid ethanol cell doped with iodine, which is a defocussing thermal medium. These experiments showed that initial sharp gradients or discontinuities in temperature are smoothed by a dispersive shock wave whose leading edge consists of dark solitary waves. Similar experiments in a defocusing thermal medium, in this case a solution of rhodamine-B in methanol, were performed by Conti et al. [34] following theoretical work on both focusing and defocusing thermal media [45]. It has also been found experimentally that, for elliptical and toroidal light beams in a focusing thermal medium, nonlocality results in the elimination of the azimuthal instabilities associated with such an elliptical or toroidal input beam [97]. This nonlocal suppression of instabilities in a toroidal beam also occurs in a nematic liquid crystal [82, 112].

Rotschild et al. [96] examined the interaction between solitons in a nonlocal

thermal media at long range, showing that the nonlocality of the medium permitted interaction at much greater range, with the force of the soliton interaction following an inverse square law analagous to interacting particles. An example of spiralling soliton behaviour with two input solitons separated by more than five times their beam width was provided. They also provided a demonstration that soliton interaction could occur at much greater distances, up to 50 times their widths, by using a non-optical mediator. In this case, a metal wire connecting the two samples transmitted thermal energy, providing a differential temperature at the cell boundary of each sample and resulting in attraction of the solitons. Figure 1.4a (Figure 4 from [96]) shows a schematic of the experimental setup, with a strip of metal foil connecting two lengths of transmission media with square cross section. Figures 1.4b and 1.4c show the input beams and Figures 1.4d and 1.4e show the unchanged position of the output beams when launched separately. Figures 1.4f and 1.4g show the displacement of the two output beams when heat generated by the beams accrues on the foil and leads to higher ambient temperatures on the adjacent boundaries. Nematic solitary waves can also interact at long distances, due to nonlocal effects. In a subsequent paper Rotschild et al. [98] also experimentally demonstrated that incoherent spatial soliton modes can propagate through a thermal lead glass medium, with an effectively instantaneous nonlocal response.

Alfassi et al. [9] examined solitary wave trajectories in a lead glass thermal medium for off-centre initial conditions and non-symmetric boundary conditions, finding good agreement between numerical and observational beam displacement as the boundary temperature difference was varied. Analytical and numerical work applicable to both unbiased liquid crystal cells and thermal media found that the boundaries are repulsive, resulting in an oscillatory solitary wave trajectory before any steady state is achieved [6], in agreement with previous studies [5, 8].

Buccoliero et al. [28] modelled the propagation of higher order thermal solitary waves (both quadrupole and double ring vortex), investigating the effect of different cell geometries (circular or square) and initial launching locations, finding that the propagation dynamics resulted in transitions into different soliton modes. Other findings were that the cell geometry also constrained the types of soliton modes that were possible, and an initial soliton location near the boundary or at

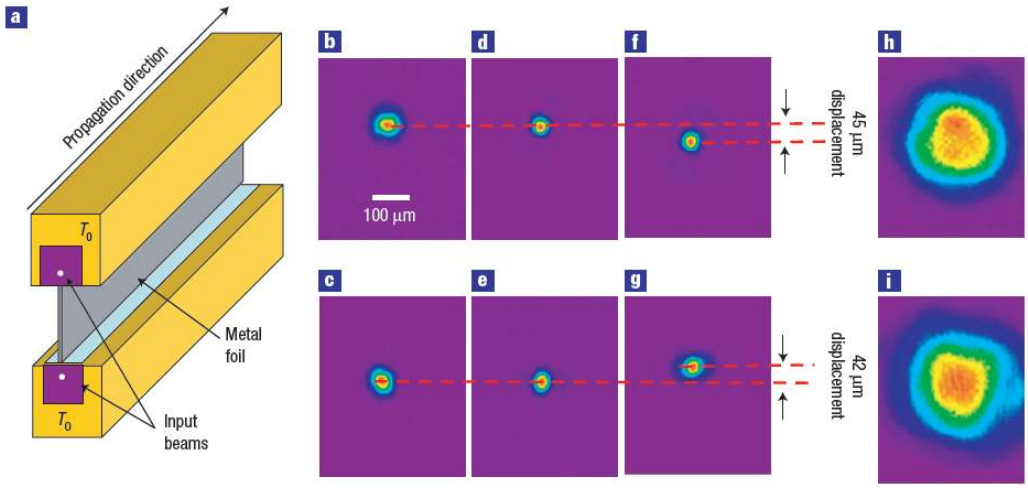

Figure 1.4: Figure 4 from Rotschild et al. [96] - experimental demonstration of the interaction between two solitons propagating in separate samples, with the interaction mediated by wiring. a, Experimental scheme. b,c, Input beams. d,e, Inividually launched output solitons. f,g, Simultaneously launched output solitons exhibiting strong attraction. h,i, At low power, the beams diffract and broaden.

the edge of the cell would result in an oscillatory trajectory. Huang [52] also numerically examined the stability of dipole mode solitons in thermal media, finding that incoherent attraction of the beams led to a more stable overall structure. Bekenstein and Segev [18] numerically investigated the behaviour of self-accelerating Airy-type waves propagating within a thermal media in an accelerating invariant frame of reference, finding complex dynamical behaviours in the case with strongly self-focussing non-linearity, including a trajectory that did not follow the parabolic accelerating frame of reference, and decomposition into two beams. Alberucci et al. [7] investigated a cylindrical symmetrical thermal media model with absorption and longitudinal nonlocality terms, finding that modelling the longitudinal nonlocality was important for cases where there was a boundary discontinuity at either end of the transmission medium, and that as higher absorption led to stronger self-focussing, a balance between the magnitude of the trapping thermal profile and the amount of power loss from absorption was required.

1.4 Analytical and Numerical Methods

For an optical thermal medium the governing equations are a coupled system of an NLS-type equation and a Poisson equation for the medium response (1.11). Assuming that the thermal diffusivity is large, Conti et al. [36] derived an approximate asymptotic analytical solution in the particular case of nematic liquid crystals, including an investigation of the transition between the local regime and the highly nonlocal general regime. However, analytical solutions do not exist for the experimentally interesting case of large, but finite, ν.

For this reason, approximate and numerical methods for determining solitary wave solutions are of great interest. To model the evolution of NLS solitons, Kath and Smyth [58] used the Lagrangian formulation of the NLS equation and a variational method to derive approximate equations for the transient evolution on an initial condition to a steady solution. A typical trial function used is

$$u = q \operatorname{sech} \frac{x}{w} e^{\imath\theta} + \imath g e^{\imath\theta}, \tag{1.12}$$

where q is the amplitude, w is the width, θ is the phase and g is radiation loss. (1.12) has the form of an NLS soliton but allows the width to vary. This approach has the benefit that it can also be used for problems with no analytical solutions, such as coupled NLS-type equations [103]. Much previous work [6, 76] has used modulation theory [111] as an approximate, variational approach [10], finding good agreement with full numerical solutions [6, 76]. Minzoni et al. [81] extended this method to derive approximate modulational equations for the case of a strongly nonlocal liquid crystal medium, including terms that modelled the effect of radiative loss, finding that strong non-locality decreased radiative loss from the nematicon as it evolved. Of relevance to the present work, Alberucci et al. [6] examined the boundary induced motion of an optical solitary wave using both numerical and variational based approaches.

Various numerical schemes have been used to solve the NLS equation and coupled NLS-type equations. Stationary solutions of coupled solitary wave equations can be derived via the substitution of a separable solution that splits the transverse and down cell components, where the solution is written as $u(x, y, z) = u(x, y)e^{\imath\mu z}$.

Rasmussen et al. [95] used this technique to investigate the interaction of multiple solitary waves for a range of values of the nonlocality parameter. Pelinovsky and Stepanyants [93] investigated the convergence of Petviashvili's iteration method when applied to finding solitary wave solutions, providing constraints including the important limitation that solitary waves with zero crossings (higher order solitons) lead to divergence of the method. Skupin et al. [102] investigated thermal soliton stability on an infinite domain using a numerical scheme that made use of the fact that in the highly nonlocal limit, the equation for the propagation vector was a symmetric band matrix which would permit fast iterative computation of the eigenvectors to obtain approximate solutions.

An imaginary time evolution method (ITEM) attempts to find the stationary solution to a time dependent equation by replacing the time variable with $\imath t$ before integrating, and normalizing to a fixed power after each iteration. Chiofalo et al. [33] demonstrated the application of this type of method to a NLS-type nonlinear system, finding that the method would converge to the ground state solutions.

A series of papers by Yang et al. [113, 114, 115] evaluated the stability and performance of numerical schemes for solving NLS-type equations. Yang and Lakoba [115] developed three forms of iteration methods based on squaring the linearized system operator to ensure convergence for all types of solitary waves. Yang and Lakoba [114] introduced an accelerated imaginary time evolution (AITE) method for improving the performance of ITEM by introducing a preconditioning operator. Yang and Lakoba [114] found convergence conditions for these methods, noting that the method would diverge for higher order solitons, and that convergence for ground states occurred if and only if the wave was linearly stable.

Yang [113] also adapted the conjugate gradient method for solving linear systems of equations for use with nonlinear equations, including the NLS equation. The approach is to combine an outer loop where the solution is updated by linearizing the solitary wave equation around an approximate solution and solving the resulting linear operator equation, with an inner loop where the efficient conjugate gradient method is used to solve this linear equation. He called this method the Newton-conjugate gradient (Newton-CG) method, and found that this method typically converged much faster than other available numerical schemes, such as squared

operator methods or the Petviashvili method. There are some challenges to using Newton methods to find solitary wave solutions [25], however Louis et al. [73] found that Newton-CG methods are stable and efficient in finding (1+1)-D steady state solutions of the coupled NLS equations describing optical solitary wave propagation in thermal media. Further details on the ITEM, AITE and Newton-CG methods are given in section 2.1.

1.5 Stability

Kuznetsov et al. [67] provides an overview of methods for analysing soliton stability for a range of equations, including the NLS equation. The review includes an overview of the variational approach and also of perturbation analyses. Krolikowski et al. [64] performed a linear perturbation analysis of MI in the (1+1)-D case for a general nonlinear response function. The analysis notes that for local response functions the presence of modulational stability (MS) depends only on whether the nonlinearity is focussing (MI exists) or defocussing (no MI exists). In the highly nonlocal case the response function is approximately linear, so there is no MI. Gain profiles were computed for a set of different response profiles, showing that increasing the degree of nonlocality tended to suppress the MI growth rates, with the exception of profiles that have discontinuities, such as a rectangular response function.

Yakimenko et al. [112] used a linear perturbation analysis to investigate the stability of vortex solitons governed by nonlocal NLS-type equations, finding that stable solutions are possible in a strongly nonlocal media. Briedis et al. [27] conducted a numerical analysis of the stability of vortex solitons, also finding that a strongly nonlocal response acts to stabilise these soliton modes. Skupin et al. [102] numerically investigated the stability of solitary waves for a number of different nonlocality models, including that arising from a thermal medium in a cylindrical symmetric geometry or an infinite domain. They found that in themal media stable azimuthon type solitons can be found at power levels for which the equivalent non-rotating vortex soliton type would be unstable, suggesting that rotating vortex solitons may be easier to produce experimentally.

Ilan et al. [54] demonstrated that for NLS type equations, the solitary wave

solution was unstable if there are negative eigenvalues of the fourth order linearised operator. They also showed that the nature of the instability can be inferred from the eigenvectors corresponding to the negative eigenvalues, with symmetric eigenvectors indicative of an amplitude instability and asymmetric eigenvectors indicating a drift instability.

Vakhitov and Kolokolov [109] derived a stability criterion (the V-K stability criterion) for the stationary solutions of a generalised form of the NLS equation using spectral operator theory, finding that a solitary wave power versus propagation constant curve with positive slope is needed for stability. Bang et al. [15] examined the applicability of the V-K stability criterion for more general quadratic and cubic nonlinearities. They found that the V-K criterion was applicable in the generalised NLS case, but was a necessary, but not sufficient, condition for the more general quadratic nonlinearity, providing an example where V-K predicted stability, but a numerical simulation showed the wave was unstable. Matuszewski et al. [78] used the V-K stability criterion to demonstrate bistable soliton solutions in the (1+1)-D case of the colloidal medium equations. Kartashov et al. [57] used a linear perturbation analysis to examine the stability of vortex solitons in thermal media with a cylindrically symmetrical geometry, finding that flatting of the refractive index profile provided a limit to the topological charge that allowed stable propagation. Only vortex solitons with topological charge of $m \leq 2$ were found to be stable, while those with charge $m \geq 3$ eventually broke down and reverted to a ground state soliton.

1.6 Thermal Media Governing Equations and Cell Boundary Conditions

In this thesis we consider the propagation of an input Gaussian, coherent, polarised light beam of wavelength λ, wavenumber $k = 2\pi/\lambda$, power P_0 and width W_B through a $(1+1)-D$ or $(2+1)-D$ nonlinear optical medium whose refractive index depends linearly on temperature change, so that $\Delta n = \beta \Delta T$, where Δn is the change in refractive index due to a temperature change ΔT [97]. Let us take Z to be the direction of propagation of the beam and we impose a coordinate system with the Z coordinate in the direction down the cell, with the X coordinate in the direction of

polarisation of the light beam, with Y completing the coordinate triad. The electric field of the optical beam will be denoted by E. In the slowly varying paraxial approximation, the dimensional equations governing the propagation of the beam are then [36, 67, 97]

$$2\imath k\frac{\partial E_x}{\partial Z} + \nabla^2 E_x + 2k^2\frac{\Delta n}{n_0}E_x = 0, \quad \kappa\nabla^2\Delta T = -\alpha|E_x|^2. \tag{1.13}$$

The parameter κ is the thermal conductivity of the medium, n_0 is the linear refractive index and α is the absorption coefficient. We have made use of the paraxial approximation, i.e. that the Z terms in the full 3D Laplacians, (i.e. $\nabla^2 = \frac{\partial^2}{\partial X^2} + \frac{\partial^2}{\partial Y^2} + \frac{\partial^2}{\partial Z^2}$) are negligible compared to the X and Y terms, so that the Laplacian ∇^2 is in the transverse plane (X, Y) to the propagation direction only. This system of equations can be set in non-dimensional form via the variable transformations

$$X = Wx, \quad Y = Wy, \quad Z = C_z z, \quad E_x = C_e E, \quad \Delta T = C_T\theta, \tag{1.14}$$

$$\text{where} \quad \mathrm{W}^2 = \frac{2\mathrm{n}_0}{\beta \mathrm{C_T k}^2}, \quad \mathrm{C_z} = \frac{2\mathrm{n}_0}{\beta \mathrm{C_T k}}, \quad \mathrm{C_e^2} = \frac{2}{\pi \mathrm{W_B^2}}\mathrm{P}_0$$

and C_T is a typical temperature change. The non-dimensional system of equations governing the propagation of the optical beam in the thermal medium are then

$$\imath\frac{\partial E}{\partial z} + \frac{1}{2}\nabla^2 E + 2E\theta = 0, \quad \nu\nabla^2\theta + 2|E|^2 = 0, \tag{1.15}$$

with the non-dimensional thermal conductivity

$$\nu = \frac{\pi K C_T}{\alpha P_0}\left(\frac{W_B}{W}\right)^2. \tag{1.16}$$

Typical parameter values are $C_T = 10K$, $n_0 = 1.8$, $\kappa = 0.7W/(mK)$, $\beta = 14 \times 10^{-6}K^{-1}$, $\alpha = 1m^{-1}$, $P_0 = 1W$, $\lambda = 488nm$ and $W_B = 50\mu m$ for lead glass [97]. These values give a non-dimensional thermal conductivity $\nu = 354$. The non-dimensional thermal conductivity is then large, $O(100)$, so that the optical response of the thermal medium is termed nonlocal [36, 88]. This nonlocal response is vital as it can stabilise (2+1)-D solitary waves propagating in the thermal medium, noting that (2+1)-D waves are unstable in local media [62]. Equation (1.15) also governs

the propagation of an optical beam in a nematic liquid crystal, when the static biasing electric field $q = 0$ in (1.9) [36, 88]. In this case θ is the rotation of the nematic molecules due to the optical beam.

For simplicity, we take the thermal medium to be a square cell of dimension L. We consider differential heating at the medium boundaries. For temperature, a Dirichlet boundary condition is applied to some of the boundaries, while a mixed boundary condition is applied to the other boundaries. The electric-field cell boundary conditions are

$$(\mathbf{E} - \mathbf{E_0}) \times \mathbf{n} = 0, \quad (\mathbf{D} - \mathbf{D_0}).\mathbf{n} = 0, \tag{1.17}$$

where $\mathbf{E}$ is the electric field and $\mathbf{D}$ the electric displacement in the cell and $\mathbf{E_0}$ and $\mathbf{D_0}$ are the same quantities in free space. Assuming a transverse beam $\mathbf{E} = E_1(x, y, z)\mathbf{i}$ we get $E_1 = E_{01}$ on $y = \pm 1$ and $E_1 = \frac{\epsilon_0}{\epsilon} E_{01}$ on $x = \pm 1$, by using $\mathbf{D} = \epsilon \mathbf{E}$, where ϵ is the electrical permittivity.

For simplicity is is assumed that the beam is confined to the cell and is a bulk beam so that there is no field outside it. Hence we get,

$$E_1 = 0 \quad \text{on} \quad x = \pm 1, \quad y = \pm 1. \tag{1.18}$$

While in experiments there is some beam leakage from the cell, the inclusion of this external field would be a much more complicated problem requiring further extensive study. The boundary conditions are then

$$E_1 = 0 \quad \text{at} \quad x = \pm \frac{L}{2}, \quad y = \pm \frac{L}{2}, \tag{1.19}$$

$$\theta = 0 \quad \text{at} \quad x = \frac{L}{2}, \quad y = \frac{L}{2}, \tag{1.20}$$

$$\theta_x - \beta_x (\theta - \theta_{B,x}) = 0 \quad \text{at} \quad x = -\frac{L}{2}, \tag{1.21}$$

$$\theta_y - \beta_y (\theta - \theta_{B,y}) = 0 \quad \text{at} \quad y = -\frac{L}{2}, \tag{1.22}$$

where β_x and β_y are the Biot numbers and $\theta_{B,x}$ and $\theta_{B,y}$ are the ambient temperatures at the relevant cell boundaries. The cell geometry is shown in Figure 1.5. The mixed condition represents Newton cooling, with $\beta_x = \beta_y = 0$ corresponding to perfectly insulated boundaries and $\beta_x, \beta_y \to \infty$ to fixed temperature boundary

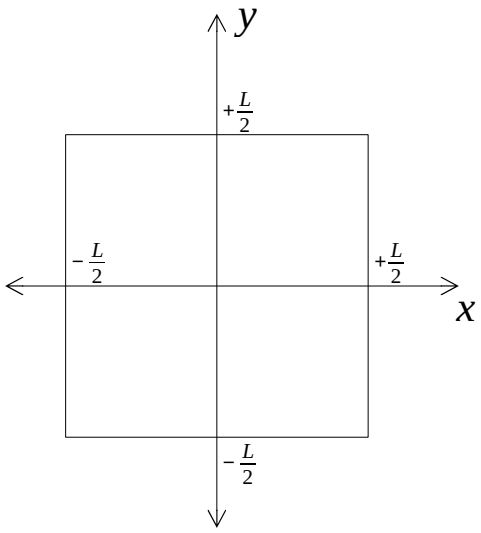

Figure 1.5: Schematic showing the cell geometry and boundaries, where L is the non-dimensional cell width.

conditions $\theta = \theta_{B,x}$ and $\theta_{B,y}$.

To find solitary wave solutions of the governing equations (1.15)–(1.22) we seek a travelling wave solution of the form $E(x, y, z) = u(x, y)e^{i\mu z}$, where u is real and μ is the propagation constant of the solitary wave. Inserting this form reduces the NLS equation for E and the Poisson equation for θ in (1.15) to

$$\frac{1}{2}\nabla^2 u + 2u\theta - \mu u = 0, \quad \nu\nabla^2\theta + 2u^2 = 0, \tag{1.23}$$

with the boundary conditions

$$u = 0 \quad \text{at} \quad x = \pm\frac{L}{2}, y = \pm\frac{L}{2} \tag{1.24}$$

and the boundary conditions for θ are as in (1.20)–(1.22). In the (1+1)-D case (1.23) and (1.24) reduce to

$$\frac{1}{2}\frac{\partial^2 u}{\partial x^2} + 2u\theta - \mu u = 0, \quad \nu\frac{\partial^2\theta}{\partial x^2} + 2u^2 = 0, \tag{1.25}$$

$$u = 0, \quad \theta_x - \beta_x(\theta - \theta_{B,x}) = 0, \quad \text{at} \quad x = -\frac{L}{2}, \tag{1.26}$$

$$u = \theta = 0, \quad \text{at} \quad x = \frac{L}{2} \tag{1.27}$$

1.7 Thesis Plan

In this thesis we investigate thermal solitary waves and their stability in an optical thermal medium with finite line and square domains, as described above. We will explore properties of the waves, with respect to changes in the boundary conditions and propagation constant. Motivation for this work is provided by the experimental results by Rotschild et al. [96] and Alfassi et al. [9] demonstrating the ability to control the trajectory and steady state position of the solitary wave within a sample by using non-zero boundary conditions, as well as the possibility for very remote interaction of solitons.

In Chapter 2 we outline three different numerical schemes for finding steady state solutions of the governing equations, including imaginary time evolution methods and Newton type methods. Using the (1+1)-D case we investigate various options for implementing these schemes, including using different order spatial discretizations, preconditioning matrices and stopping conditions. We find that the Newton-CG method is the quickest and most stable method for this application, and use this for derivation of results in subsequent sections.

In Chapter 3 we calculate and describe steady state solitary waves in a non-linear thermal medium, for both the (1+1)-D and (2+1)-D forms of the governing equations. We demonstrate that fundamental and higher order solitary waves can be found using the Newton-CG method. We find that applying a differential temperature at the cell boundaries causes the steady state solution to migrate towards the warmer cell boundary or boundaries. For the (1+1)-D case we find the amplitudes and positions of the steady state solitary wave solution in the phase space of different boundary temperatures and heat loss. For the (2+1)-D case we provide diagrams showing the amplitude and position of the steady state solution for different boundary temperatures at adjacent boundaries.

In Chapter 4 we investigate the stability of the thermal solitary wave solutions using the VK stability criterion, a spectral stability analysis, and by numerical simulation of the time-dependent thermal medium equations. We find that the fundamental solitary wave is stable for all boundary temperatures and for different propagation constants in the (1+1)-D case, but that solitary waves are only stable for some combinations of these parameters in the (2+1)-D case.

Chapter 2

Numerical Methods

A variety of different numerical schemes have been used to find steady solitary wave solutions [113]. In this thesis three of these schemes are implemented for the $(1+1)$-D case and benchmarked to check that consistent solutions are generated and to gauge which is the most efficient for solving the coupled system (1.23). Considered are the ITEM [39, 114], the AITE method [114] and the Newton-CG method, each following the implementations used by Yang [113]. One main difference between the implementations used here and in Yang is that we use a direct fourth-order spatial discretization, whereas Yang used a Fourier transform to derive a spectral discretization. Also, the examples considered by Yang did not include the coupled system (1.23) and (1.24) of interest here. In the following descriptions of the numerical schemes we consider $v(x)$ where $v = u$ for the ITEM and AITE methods, and $v = (u, \theta)^T$ for the Newton-CG method. All the solvers were iterated until the maximum difference between successive iterations, $\epsilon = ||v_n - v_{n-1}||_2$, reached the stopping condition $\epsilon \leq 10^{-10}$, see Section 2.5 for details on how this value was chosen. All quoted computation times are based on an Intel Core i5-2500K processor running at 3.3GHz. Programs were written in Python 2.6 and NumPy 1.6.1 for the (1+1)-D cases and Julia 0.6 for the (2+1)-D cases [22]. A selection of the code written to implement the fourth order Newton-CG method for this coupled system is included as Appendix A.

2.1 Description of iterative methods

To implement the ITEM and AITE methods, equation (1.25) for a steady solitary wave is written in the form

$$L_{00}v(x) = \mu v(x), \quad \text{where } L_{00} \equiv \frac{1}{2}\frac{\partial^2}{\partial x^2} + 2\theta. \tag{2.1}$$

In the discussion below, L, L_0, L_{00} and M are all operators, which correspond to matrices once a finite difference approximation for $\frac{\partial^2}{\partial x^2}$ is applied. For the ITEM method we consider the equation $v_t = L_{00}v$ obtained by replacing z with $-it$. This equation is numerically integrated using the Euler method. At each iteration v_n the solution must be normalized to a fixed power to prevent the solution from diverging to infinity or decaying to zero. The ITEM iterative method can be written as

$$v_n^* = \frac{P}{< v_n, v_n >} v_n, \quad v_n = (1 + L_{00}\Delta t)v_{n-1}^*, \quad < u, v >= \int_{L/2}^{L/2} uv dx, \tag{2.2}$$

where P is the fixed power of the converged solitary wave solution and Δt is the size of the discretization step. Note that Δt is not a time step. The system (2.2) is iterated until the solution converges. The AITE method iterates the equation $v_t = M^{-1}(L_{00}v - \mu v)$, where M is a a preconditioning matrix to improve the rate of convergence of the scheme by modifying its condition number. We choose $M = c - \partial^2/\partial x^2$, with $c = 1.5$, as the preconditioning matrix.

The threshold value of the disctretization step Δt at which instability begins to occur for the AITE and ITEM schemes depends on the eigenvalues of the operator

$$L\Psi = M^{-1}\left(L_1\Psi - \frac{\langle L_1\Psi, M^{-1}v\rangle}{\langle v, M^{-1}v\rangle}v\right), \tag{2.3}$$

where L_1 is the linearisation operator of Lv with respect to v. Yang [114] derived the relation $\Delta t_{max} = -2/\Lambda_{min}$, where Λ_{min} is the minimum eigenvalue of the operator L, to give the maximum value of Δt for which the imaginary time method converges.

To implement the Newton-CG method, we consider (2.1) in the form $L_0 v(x) = 0$, where $L_0 = L_{00} - \mu$. Given an approximate solution v_n, we can write $v = v_n + e_n$, where v is the exact solution and e_n is the error. Substituting this into (2.1) and

Method	Number of Grid Points	Computation Time (secs)
Second Order	106	31.3
Fourth Order	36	2.9

Table 2.1: Number of discretization grid points and amount of computation time required to converge to stopping condition $\epsilon \leq 1 \times 10^{-10}$

Method	Iterations	Computation Time (mins)
ITEM	135316	3.89
AITE	222643	9.15
Newton-CG	65049	0.09

Table 2.2: Number of iterations and computation time required to reach stopping condition $\epsilon \leq 1 \times 10^{-10}$ for the three numerical schemes.

neglecting higher-order terms in e, we obtain

$$L_{1n}\Delta v_n = -L_0 v_n, \tag{2.4}$$

where the next approximation is $v_{n+1} = v_n + \Delta v_n$ and L_{1n} is the linearised operator evaluated at the iterate v_n. Equation (2.4) is solved for Δv_n using the conjugate gradient method. In general, the convergence of the conjugate gradient method requires that the matrix L_{1n} be self-adjoint, which is not the case here. To circumvent this, we pre-multiply both sides of (2.4) by L_{1n}^T prior to solving. This has the effect of greatly increasing the condition number of the matrix $(L_{1n}^T L_{1n})$ and also increases the computation time, but does not change the solution, and ensures that the method converges.

One drawback of the AITE and ITEM methods is that they do not converge to the correct solution if the method is implemented to solve for a single solution vector $v = (u, \theta)^T$. To successfully implement these methods, the numerical scheme was then applied to the NLS-type equation only (where $v = u$) and after each iteration a number of Gauss-Seidel iterations of the Poisson equation were applied to solve for θ.

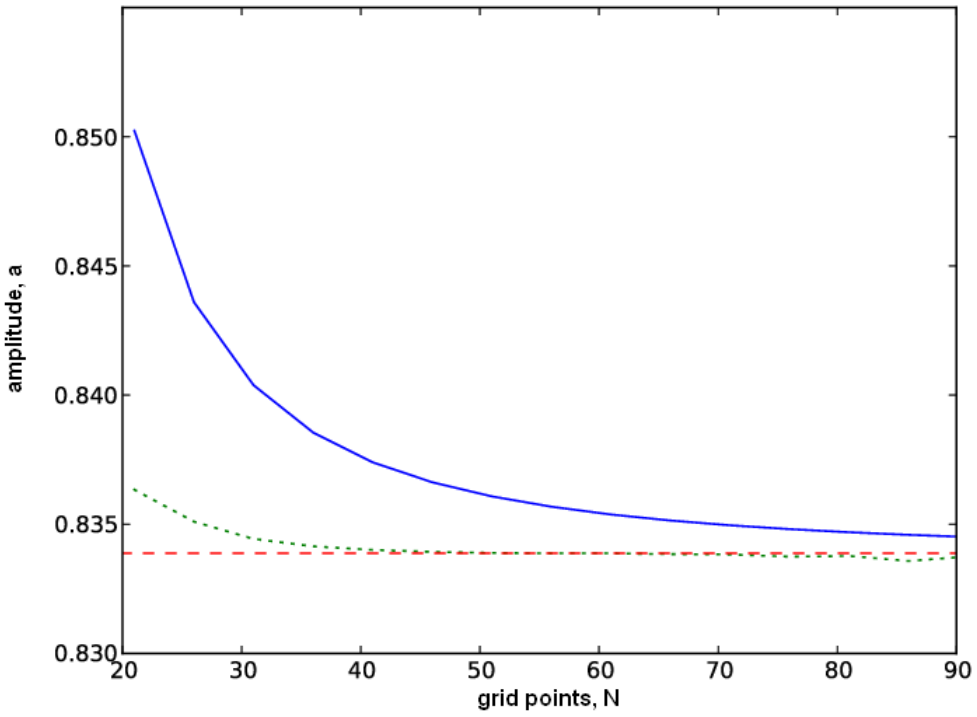

Figure 2.1: Amplitude of the solitary wave, a, versus the number of grid points N. Shown are results for the second-order discretization (solid line, blue), fourth-order discretization (dotted line, green) and the Richardson extrapolation fifth order estimate for the converged solution (dashed line, red). The other parameters are $\beta_x = 100$, $\theta_{B,x} = 0.2$, $\mu = 1$, $\nu = 100$.

2.2 Order of the spatial discretization

The performances of the second and fourth-order finite difference implementations of the Newton-CG will now be compared. To implement the fourth-order scheme a non-symmetric finite difference stencil was used for the second of (1.25) at the first interior point and for the boundary condition

$$\begin{aligned} &48\theta_1 - 3\theta_4 + 16\theta_3 - 36\theta_2 - 25\theta_0 - 12\beta_x\Delta x(\theta_0 - \theta_{B,x}) = 0, \\ &\theta_0 - 15\theta_1 - 4\theta_2 + 14\theta_3 - 6\theta_4 + \theta_5 + 24\Delta x^2|u_1|^2 = 0. \end{aligned} \tag{2.5}$$

Figure 2.1 shows the amplitude of the solitary wave, a, versus the number of grid points, N. The other parameters are $\beta_x = 100$, $\theta_{B,x} = 0.2$, $\mu = 1$ and $\nu = 100$. Both the second and fourth-order implementations asymptotically approach the exact solution as the number of discretization points is increased. Also shown in Figure

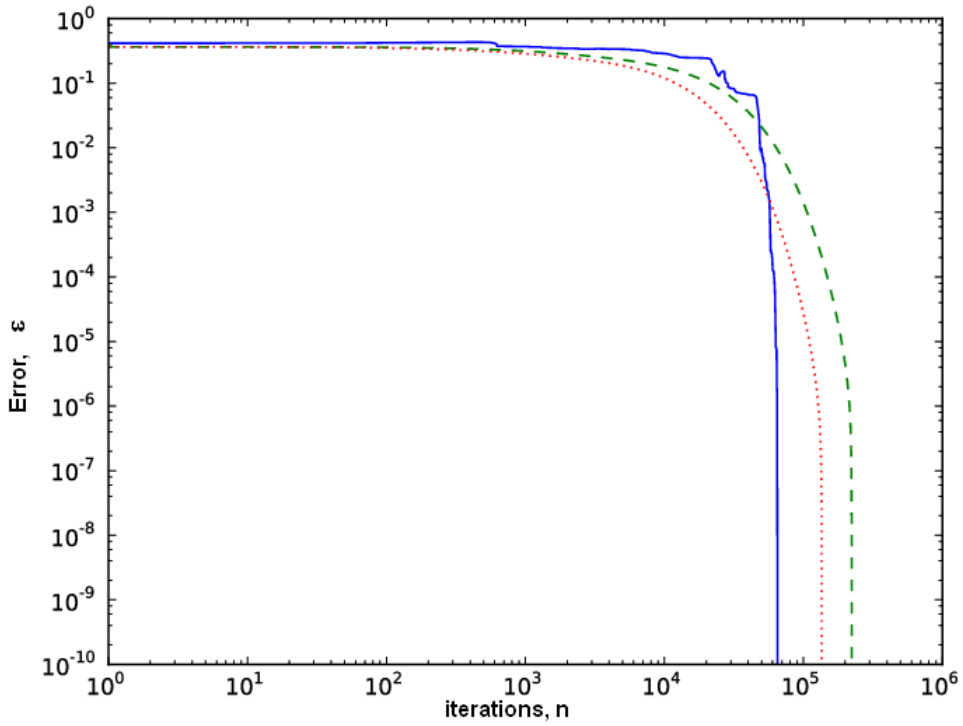

Figure 2.2: Comparison of convergence rates for the numerical schemes, with the maximum difference between successive iterations, $\epsilon = ||v_n - v_{n-1}||_2$, versus the number of iterations, n. Shown are the results for the Newton-CG method (solid line, blue), AITE method (dotted line, green) and ITEM (dashed line, red).

2.1 is a fifth order approximation to the exact solitary wave amplitude derived using Richardson extrapolation, discussed in Section 2.5.

Table 2.1 shows the number of grid points and computation time needed to achieve a fixed accuracy. The parameters considered are those used in Figure 2.1 and the chosen accuracy for the solitary wave amplitude a is an error of less than 1×10^{-4}. It can be seen that the fourth-order method requires far fewer grid points to obtain the same accuracy as the second order method. Due to the reduction in grid points, the fourth-order method is an order of magnitude faster than the second-order method. This increased efficiency, while useful for the $(1+1)$-D geometry, is of vital importance for the implementation of the method in $(2+1)$-D.

Method	Iterations	Computation Time (seconds)
No Preconditioning	68490	13.5
Diagonal Elements of L_1	44672	13.0
Diagonal Scale Matrix	55517	9.4
Diagonal Elements of $L_1 - \theta$	45674	12.4

Table 2.3: Number of iterations and computation times required for the Newton-CG method to reach the stopping condition $\epsilon \leq 1 \times 10^{-10}$ for a number of different preconditioning matrices.

2.3 Convergence rates

To check the convergence rates it is first necessary to make sure the methods are converging to the same solution, as a solitary wave is a one parameter solution. The propagation constant μ can be chosen as this parameter. One of the differences between the imaginary time and the Newton-CG methods is that in the imaginary time method the power of the solitary wave is scaled to a fixed value to ensure that the numerical scheme does not diverge, so that a solution for a pre-determined value of μ is not found, but the method chooses its own value of μ. In contrast, for the Newton-CG method the solution power is controlled by the propagation constant μ. The power of the solitary wave

$$P = \int_{-L/2}^{L/2} |u|^2 \, dx \tag{2.6}$$

using the Newton-CG method $P = 3.246$ for $\mu = 1$. When this value of the power is used to scale the AITE and ITEM methods, the three iterative methods converge to the same solution.

Figure 2.2 shows a comparison of convergence rates for the three numerical schemes, with the maximum difference between successive iterations, $\epsilon = ||v_n - v_{n-1}||_2$, versus the number of iterations, n. Shown are the results for the Newton-CG method, AITE method and ITEM. The parameters are $\theta_{B,x} = 0.2$, $\nu = 100$, $\mu = 1$, $\beta_x = 100$, $\Delta x = 0.33$ and $\Delta z = 0.003$. Table 2.2 shows the number of iterations and computation times for convergence with $\epsilon < 1 \times 10^{-10}$, for the examples of Figure 2.2. The curve for the Newton-CG method shows both the Newton and CG iterations. The ITEM and AITE methods converge smoothly to the solution, whilst the Newton-CG method does not. However, the figure and table show that

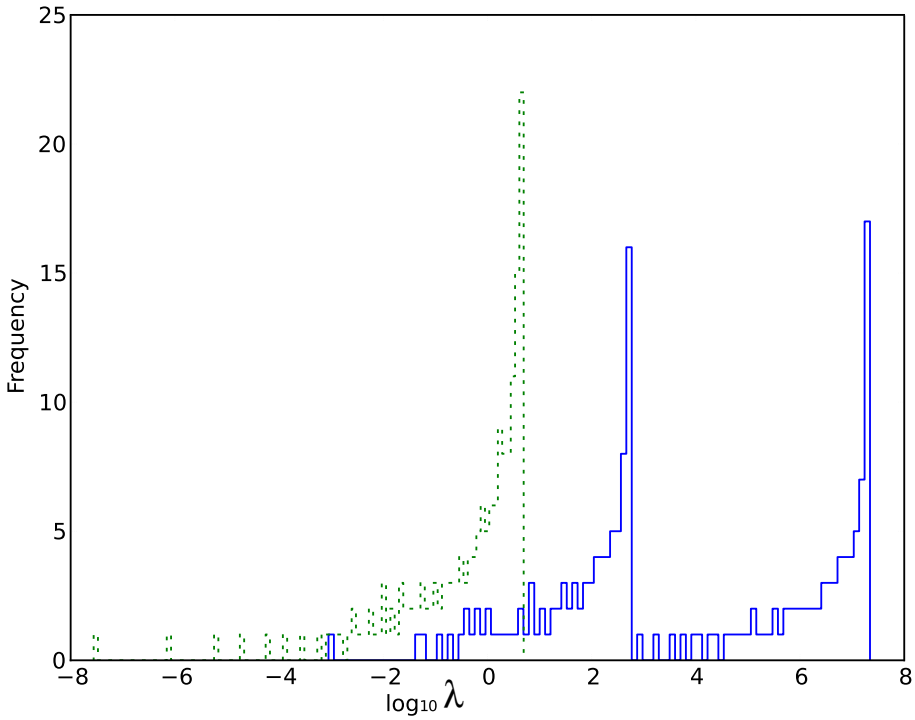

Figure 2.3: Newton-CG scheme eigenvalue distributions as frequency versus $\log(\lambda)$ for no preconditioning (solid line, blue) and preconditioning matrix containing diagonal elements of L_1 (dotted line, green).

the Newton-CG method is several orders of magnitude faster than the other methods, due to the lower number of total iterations and the lower computational cost of the conjugate gradient iterations. For the Newton-CG method the total number of iterations is comprised of 294 Newton iterations, with on average around 221 inner conjugate gradient steps. Also note that the AITE method is actually slower than the ITEM, because the performance gain due to preconditioning does not offset the extra computational overhead associated with this method.

We then conclude that the Newton-CG method is clearly the most natural and efficient choice for finding the steady solitary wave solution of (1.25), due to its ability to solve the coupled equations for u and θ in a unified manner, and its faster (a factor of over 100 times) convergence time.

2.4 Preconditioning

To increase the speed of convergence of the Newton-CG method a number of different preconditioning matrices M^{-1} for the numerical scheme (2.4) were used. The computation speeds for the different choices of matrices are shown in Table 2.3. All of the preconditioning matrices yielded only slight performance differences, if any. The most beneficial of those tested was the matrix for which M contains the diagonal elements of L_0. However, the performance increase was slight. When the preconditioning matrix and pre-multiplication by the transpose are both applied, the numerical scheme (2.4) becomes

$$(M^{-1}L_1)^T M^{-1}L_1 v_{1n} = -(M^{-1}L_1)^T M^{-1} v_n. \tag{2.7}$$

Figure 2.3 shows the Newton-CG scheme eigenvalue distributions as frequency versus $\log(\lambda)$ for no preconditioning and preconditioning matrix containing diagonal elements of L_1. Note that the set of eigenvalues changes with each iteration, but approaches a fixed set of values as the numerical method converges and the changes in L_0 and L_1 become small. The figure shows the eigenvalue distribution for the iterations immediately prior to convergence. For the case with no pre-conditioning there are two clusters of eigenvalues, with peaks in the distribution around $\lambda = 2 \times 10^7$ and 5.5×10^2, and a condition number $\kappa = 2.5 \times 10^{10}$. For the pre-conditioned case there is a single cluster of eigenvalues, with a peak in the distribution around $\lambda = 4.5$ and a lower condition number $\kappa = 1.8 \times 10^8$. The coupled nature of the equations means that in the non-preconditioned version of the scheme, corresponding to $M = I$, there is a bimodal distribution of eigenvalues and a large condition number. Once the diagonal pre-conditioner has been applied, the bimodal distribution is eliminated and there is a much smaller condition number, with corresponding performance gains for the numerical scheme.

2.5 Stopping Condition

Selecting a suitable discretization scheme for the iterative methods requires some care, as there is limited benefit in setting the stopping condition for the scheme at

a lower level than the error introduced by the discretization. The amplitude of the solitary wave can be expanded in the series

$$a = a(\Delta x) + a_1 \Delta x^4 + O(\Delta x^6), \tag{2.8}$$

as the fourth order Runge-Kutta method is used, where a is the exact solution, $a(\Delta x)$ is the numerically derived solution and a_1 the fourth-order error term. Taking $\Delta x = 0.33$ and $\Delta x = 0.66$ with $\nu = 100$, $\mu = 1$, $\beta_x = 100$ and $\theta_{B,x} = 0.2$ yields the values $a(0.33) = 0.8338$ and $a(0.66) = 0.8337$, respectively. We can then derive higher order approximations to a and the leading order error a_1 on using Richardson extrapolation as

$$a = \frac{2^2 a(0.33) - a(0.66)}{2^2 - 1} + O(\Delta x^5), \approx 0.83387 \tag{2.9}$$

$$a_1 = \frac{a(0.33) - a(0.66)}{1 - \frac{0.66}{2^2}} + O(\Delta x^5) \approx 1.72 \times 10^{-4}. \tag{2.10}$$

From these we can calculate that the discretization error when $\Delta x = 0.33$ is $a - a(0.33) \approx 4.75 \times 10^{-5}$. The stopping condition ϵ should then be less than $\mathrm{O}(10^{-5})$ and greater than the round-off error. Hence, we choose $\epsilon = 10^{-10}$, which is suitable for the choice $\Delta x = 0.33$ and also for much smaller choices of Δx.

2.6 (2+1)-D numerical performance

To solve the system of thermal equations (1.23) with the boundary conditions (1.24) we tested two numerical methods for convergence and speed, the Newton-CG method and the ITEM. Figure 2.4 shows the maximum error, ϵ, between each iteration versus the iteration number, n. Both numerical schemes converge with a comparable number of iterations when using a stopping condition of $\epsilon = 10^{-10}$. However, each iteration of the Newton-CG method was significantly faster, so we have used this method throughout the solution space for the coupled system. A detailed description of the Newton-CG method is included in Section 2.1. The computation time required to solve the case where $\theta = 0$ at all four boundaries was approximately 53 minutes with the ITEM method using a desktop PC with dual Intel Core i5-2500K processors

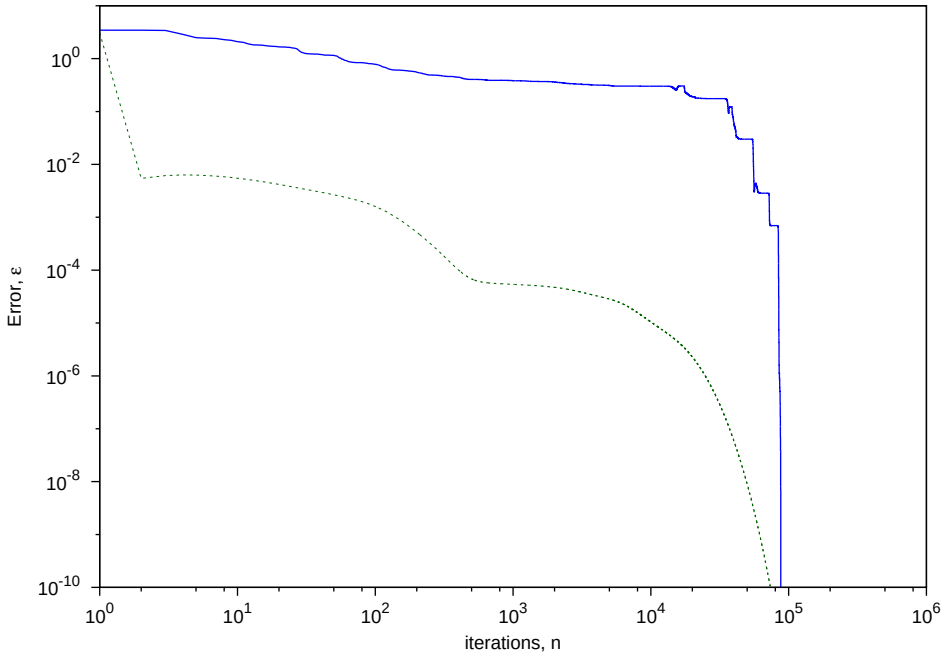

Figure 2.4: Comparison of convergence rates for the numerical schemes, with the maximum error between each iteration and the numerical solution, ϵ, versus the number of iterations, n. Shown are the results for the Newton-CG method (solid line, blue) and ITEM method (dashed line, green).

and 8GB of RAM. This is about two orders of magnitude slower than the Newton-CG method, which reached the solution in 20 seconds.

Chapter 3

Steady State Thermal Solitary Waves

In the previous section it was shown that the Newton-CG technique is the most efficient and versatile iterative method for finding solitary wave solutions of the coupled thermal system (1.23) and (1.24). In this section the Newton-CG method shall be used to explore the solution space for our coupled system and the effects of non-symmetric temperature boundary conditions for the cell on a solitary wave. The results for the (1+1)-D governing equations are presented in Section 3.1 and also in Louis et al. [73]. The results for the (2+1)-D governing equations are presented in Section 3.2 and also in Louis et al. [72].

3.1 (1+1)-D Solitary Waves

In all the examples considered here we use a non-dimensional cell of length $L = 30$ and choose $\Delta x = 0.33$. We consider the large thermal conductivity limit, with $\nu = 100$.

Figure 3.1 shows thermal solitary wave solutions of (1.25) for large Biot number β_x. Shown are the electric field amplitude, u, and temperature, θ, versus x. The three solitary waves are for $\theta_{B,x} = 0$, 0.2 and 0.6. The other parameters are $\beta_x = 100$ and $\mu = 1$. When $\theta_{B,x} = 0$ both cell boundaries are at the same temperature and the solitary wave is symmetric, with the peak of the solitary wave, of amplitude $a = 0.96$, located at the centre of the cell, $x = 0$. In this case the thermal solitary waves are equivalent to nematic solitary waves in a finite cell (nematicons), described in [6]. As the ambient temperature, $\theta_{B,x}$, of the left-hand cell boundary increases,

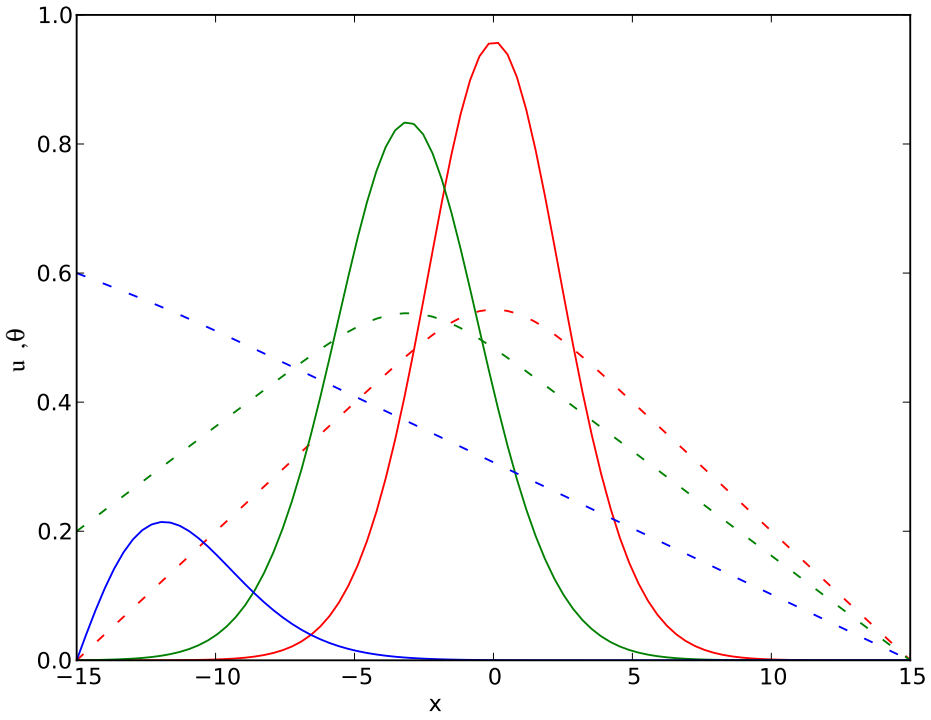

Figure 3.1: Thermal solitary waves, large Biot number case. Shown are the electric field amplitude, u (solid), and temperature, θ (dashed), versus x. The three solitary waves are $\theta_{B,x} = 0$ (red, center), $\theta_{B,x} = 0.2$ (green, slightly offset) and $\theta_{B,x} = 0.6$ (blue, near boundary). The other parameters are $\beta_x = 100$ and $\mu = 1$.

the peak of the solitary wave decreases in amplitude and moves towards the warmer boundary, as found in [9]. For the $\theta_{B,x} = 0.2$ case the peak amplitude has decreased to $a = 0.83$ and is located at $x = -3.2$. For $\theta_{B,x} = 0.6$ the wave is located at $x = -11.9$, close to the cell boundary, and the amplitude is much reduced, to $a = 0.215$. In this case the temperature profile is a near linear variation between the two ambient values of $\theta = 0.6$ and 0. For small values of $\theta_{B,x}$ the peak values of u and θ are co-located. However, as $\theta_{B,x}$ becomes large this is no longer the case and the peak θ value is found closer to the edge of the cell. It may also be noted that for small $\theta_{B,x}$ the slope of the temperature profile near the left cell boundary is positive, whereas for the large $\theta_{B,x}$ case this slope is negative. For the small $\theta_{B,x}$ examples the electric field amplitude is large and the pulse causes significant internal heating of the medium. The positive temperature profile at the left hand cell boundary indicates that some of this generated heat is being lost at the cell boundary. For the $\theta_{B,x} = 0.6$ case, however, little internal heat generation occurs, as the electric

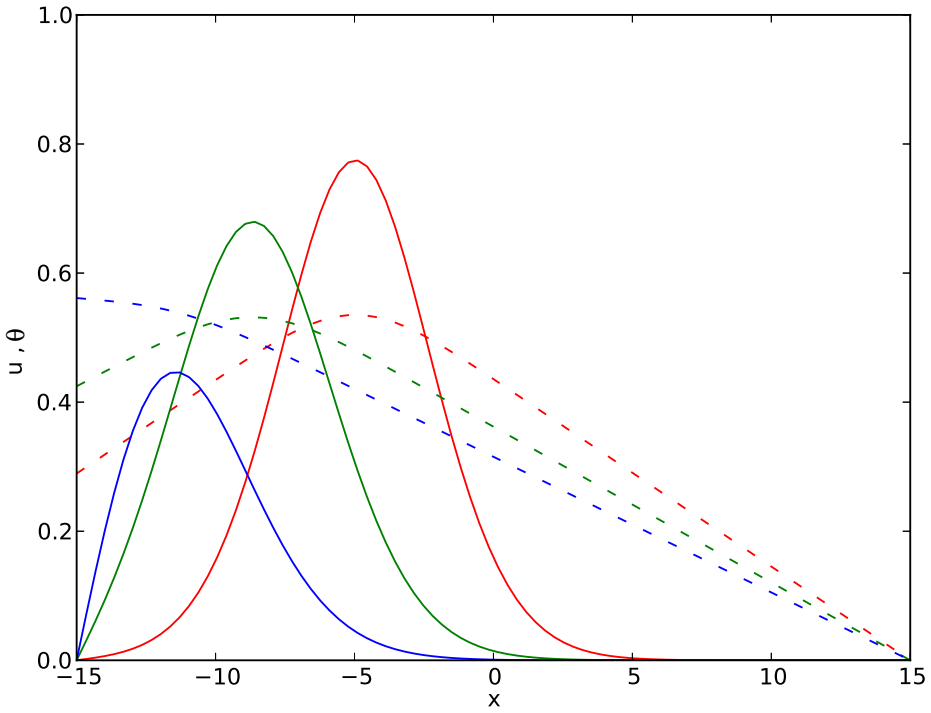

Figure 3.2: Thermal solitary waves, small Biot number case. Shown are the electric field amplitude, u (solid), and temperature, θ (dashed), versus x. The three solitary waves are $\theta_{B,x} = 0$ (red, nearest to center), $\theta_{B,x} = 0.2$ (green) and $\theta_{B,x} = 0.6$ (blue, nearest to boundary). The other parameters are $\beta_x = 0.1$ and $\mu = 1$.

field amplitude is small, and the negative slope of the temperature profile indicates the cell is being heated via the warmer cell boundary.

Figure 3.2 shows thermal solitary wave solutions of (1.25) for small Biot number β_x. Shown are the electric field amplitude, u, and temperature, θ, versus x. The three solitary waves are for $\theta_{B,x} = 0$, 0.2 and 0.6. The other parameters are $\beta_x = 0.1$ and $\mu = 1$. For this figure the parameters are the same as for Figure 3.1, except for the Biot number, which is small. In this case, when $\theta_{B,x} = 0$ the steady-state temperature at the left cell boundary is $\theta(-15) = 0.29$ and the peak of the solitary wave, of amplitude $a = 0.77$, which is located at $x = -5.1$. This wave shows some qualitative and quantitative differences compared with the $\theta_{B,x} = 0$ wave for the large Biot number example of Figure 3.1. The wave is non-symmetric, being located closer to the left hand cell boundary, and its amplitude is lower. As $\theta_{B,x}$ increases, the steady state temperature at the left cell boundary increases and approaches $\theta_{B,x}$. As for the large Biot number case, the waves migrate towards the left hand

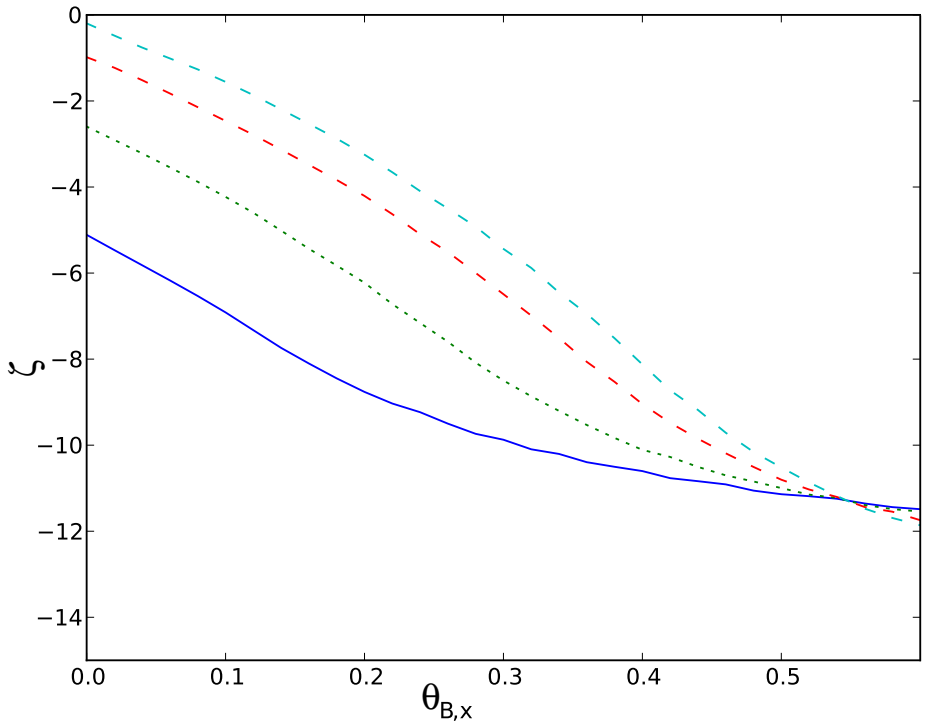

Figure 3.3: Location of the peak of thermal solitary wave, ζ, versus the ambient temperature, $\theta_{B,x}$, for $\mu = 1$. The curves correspond to $\beta_x = 0.1$ (solid line, dark blue), $\beta_x = 0.2$ (dotted line, green), $\beta_x = 0.6$ (dashed line, red) and $\beta_x = 10$ (dashed line, light blue).

cell boundary as this edge of the cell heats up. For the $\theta_{B,x} = 0.2$ case the peak amplitude has decreased to $a = 0.68$ and is located at $x = -8.75$. For $\theta_{B,x} = 0.6$, the amplitude of the solitary wave is further reduced, to $a = 0.45$ and the solitary wave peak is now located much closer to the cell boundary, at $x = -11.5$. The temperature at the left cell boundary is $\theta(-15) = 0.56$, close to the ambient value and the temperature profile is near linear, with negative slope, for the same reason as the equivalent large Biot number case. Again, as in the large Biot number case, the u and θ maxima are co-located for small $\theta_{B,x}$, and the temperature maximum is close to the edge of the cell for large $\theta_{B,x}$.

Figure 3.3 shows the location of the peak of the thermal solitary wave, ζ, versus the ambient temperature, $\theta_{B,x}$, for $\mu = 1$. The curves correspond to $\beta_x = 0.1$, 0.2, 0.6 and 10. The $\beta_x = 10$ curve is very close to the result obtained in the large Biot number limit $\beta_x \to \infty$. As the ambient temperature at the left hand cell boundary, at $x = -15$, is increased, the thermal solitary wave migrates towards the

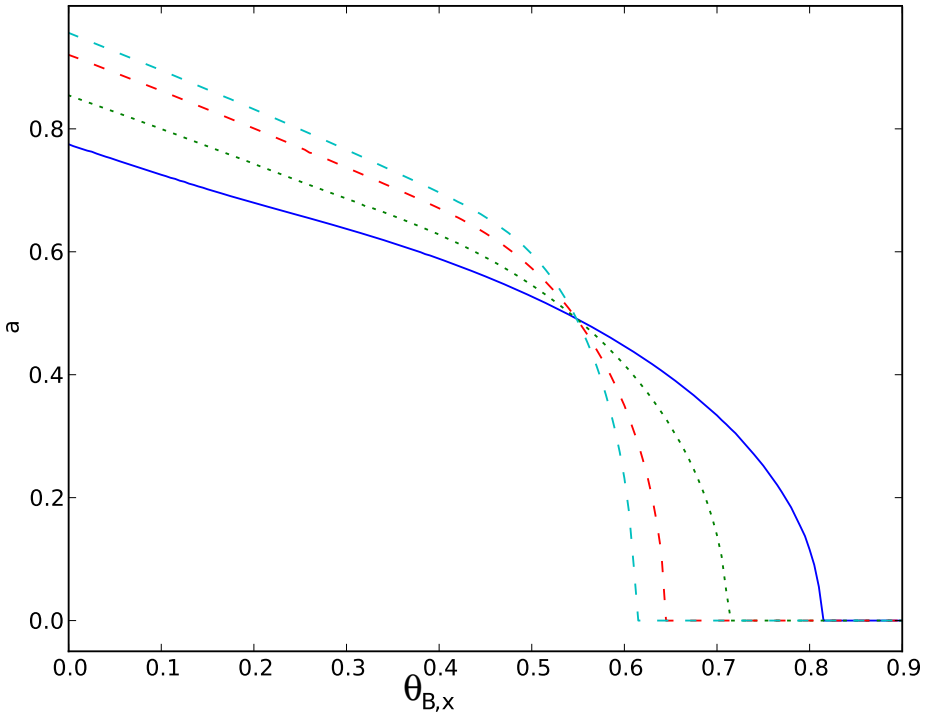

Figure 3.4: Amplitude of the thermal solitary wave, a, versus the ambient temperature, $\theta_{B,x}$, for $\mu = 1$. The curves correspond to $\beta_x = 0.1$ (solid line, dark blue), $\beta_x = 0.2$ (dotted line, green), $\beta_x = 0.6$ (dashed line, red) and $\beta_x = 10$ (dashed line, light blue).

left hand edge of the cell. Once $\theta_{B,x}$ exceeds 0.6, the numerical scheme converges to $u = 0$. It is likely that no thermal solitary waves exist once the difference in ambient temperatures between the two sides of the cell is greater than a certain limit. Physically, this may be due to the fact that the temperature profile begins to be dominated by the linear boundary diffusion solution, which does not support the solitary wave. Increasing the Biot number, β_x, also causes the solitary wave to shift towards the left hand cell boundary.

Figure 3.4 shows the amplitude of the thermal solitary wave, a, versus the ambient temperature, $\theta_{B,x}$, for $\mu = 1$. The curves correspond to $\beta_x = 0.1$, 1, 10 and 100. For a given choice of β_x, the solitary wave amplitude decreases as $\theta_{B,x}$ increases. The solitary wave amplitude decreases to $a \approx 0$ at a given value of $\theta_{B,x}$, after which thermal solitary waves do not exist. This threshold value of $\theta_{B,x}$ decreases as β_x increases from $\theta_{B,x} = 0.82$ at $\beta_x = 0.1$, to $\theta_{B,x} = 0.6$ at $\beta_x = 100$.

Figures 3.5(a) and (b) show the thermal solitary wave amplitude, a and location,

ζ, respectively, in the $(\theta_{B,x}, \beta_x)$ parameter space for $\mu = 1$. Note that, as expected, increasing $\theta_{B,x}$ causes the amplitude of the solitary wave to decrease, as well causing it to migrate towards the left hand edge of the cell. For the range of Biot number $0 \leq \beta_x \leq 1.2$ shown in the figure, the solitary wave amplitude is non-zero for $0 \leq \theta_{B,x} \leq 0.6$. As the Biot number increases, the solitary wave amplitude also increases and approaches a constant value for a given $\theta_{B,x}$. In addition, the solitary wave position migrates towards the left hand cell boundary with decreasing Biot number. Physically, decreasing Biot number corresponds to lower heat loss at the boundary, which allows the temperature at the boundary to increase. This results in similar behaviour of the optical pulse to directly changing the temperature.

The Newton C-G method can also be used to solve for excited state thermal solitary waves. This ability is another advantage of the Newton-CG method, as the imaginary time methods do not converge to these excited state solutions. Figure 3.6 shows excited state thermal solitary wave solutions of (1.25). Shown are the electric field amplitude, u, and temperature, θ, versus x. The three solitary wave solutions are for $\theta_{B,x} = 0$, 0.1 and 0.2. The other parameters are $\beta_x = 100$ and $\mu = 0.2$. This figure shows that the electric field amplitude, u, has three peaks, so that the waves correspond to the first excited state. In contrast, the temperature response θ has a single peak. This is due to heat diffusion, which smooths out the temperature response for large ν. For $\theta_{B,x} = 0$ the solitary wave is symmetric, with a peak of amplitude $a = 0.36$ located at $x = 0$ and a peak of amplitude $a = 0.401$ located at $x = \pm 5.3$. This example is equivalent to the (symmetric) first excited state nematicon in a nematic liquid crystal [75]. For the case $\theta_{B,x} = 0.1$ the peaks have shifted towards the left hand cell boundary and decreased in amplitude, with peaks of $a = 0.316$ at $x = 4.1$, $a = 0.28$ at $x = -3.4$, and $a = 0.3$ at $x = -10.9$. For the $\theta_{B,x} = 0.2$ the temperature profile is now nearly linear and the peak amplitudes are $a = 0.18$ at $x = 0.54$, $a = 0.15$ at $x = -6.9$, and $a = 0.135$ at $x = -13.7$. Beyond this, for $\theta_{B,x} > 0.24$, the excited state solitary waves do not exist. Excited state thermal solitary waves exist for a smaller range of ambient temperatures $\theta_{B,x}$ than do the ground state waves, as they break down faster as the left most peak approaches the left hand boundary.

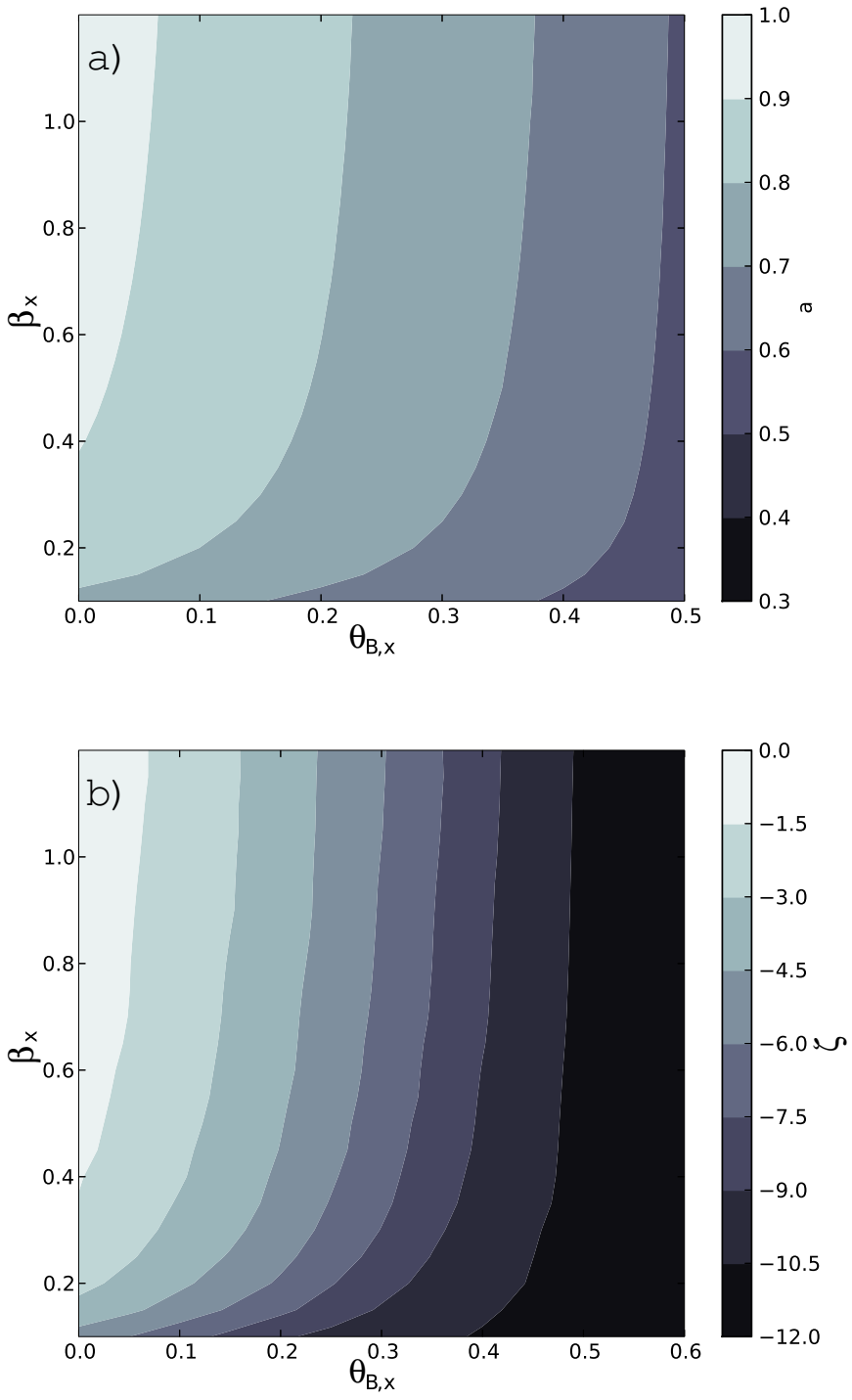

Figure 3.5: Thermal solitary wave (a) amplitude a and (b) position ζ in the $(\theta_{B,x}, \beta_x)$ parameter space for $\mu = 1$.

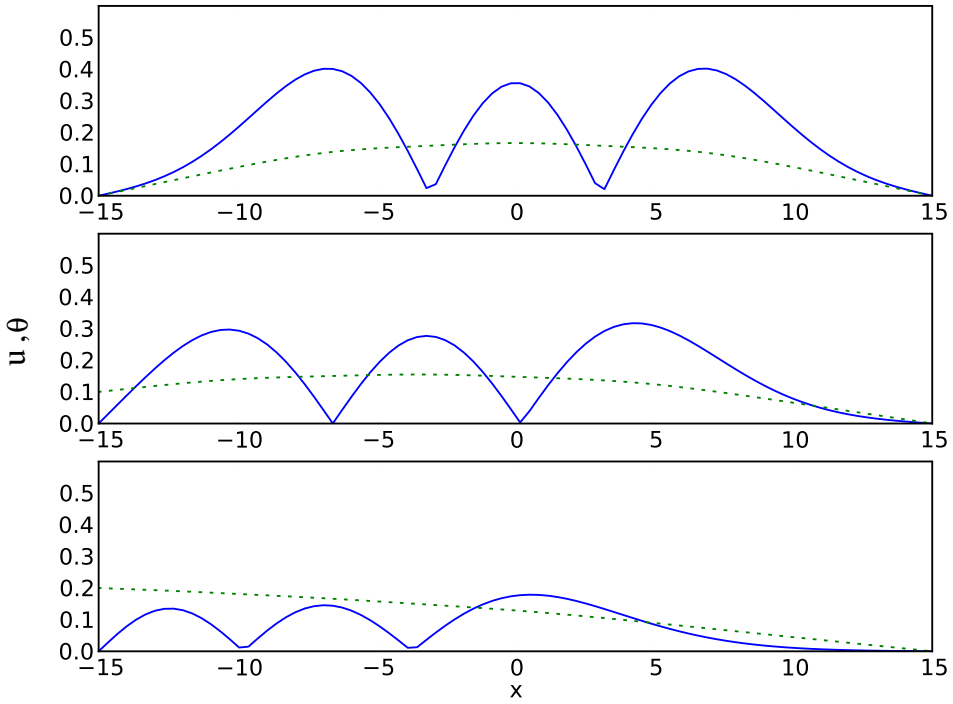

Figure 3.6: Excited state thermal solitary waves. Shown are the electric field amplitude, u (blue, solid lines), and temperature, θ (green, dotted lines), versus x. The three solitary waves are $\theta_{B,x} = 0$ (top panel), $\theta_{B,x} = 0.1$ (middle) and $\theta_{B,x} = 0.2$ (bottom). The other parameters are $\beta_x = 100$ and $\mu = 0.2$.

3.2 (2+1)-D Solitary Waves

We now consider the steady solitary waves obtained from the (2+1)-D cell geometry. In all of the examples considered we have used a cell of length $L = 30$ and choose $\Delta x = \Delta y = 0.682$. The large thermal conductivity limit is also considered, with $\nu = 100$.

3.2.1 Single boundary with non-zero ambient temperature

In this section we consider the behaviour of the solitary wave solution as the temperature on the $y = -\frac{L}{2}$ cell boundary changes. The other boundaries are fixed at the ambient temperature. The boundary conditions used are (1.24) for u, but with $\beta_x \to \infty$ and $\theta_{B,x} = 0$, so that we have

$$\theta = 0 \quad \text{at} \quad x = \pm\frac{L}{2}, \quad y = \frac{L}{2}; \theta_y - \beta_y\left(\theta - \theta_{B,y}\right) = 0, \quad \text{at} \quad y = -\frac{L}{2} \tag{3.1}$$

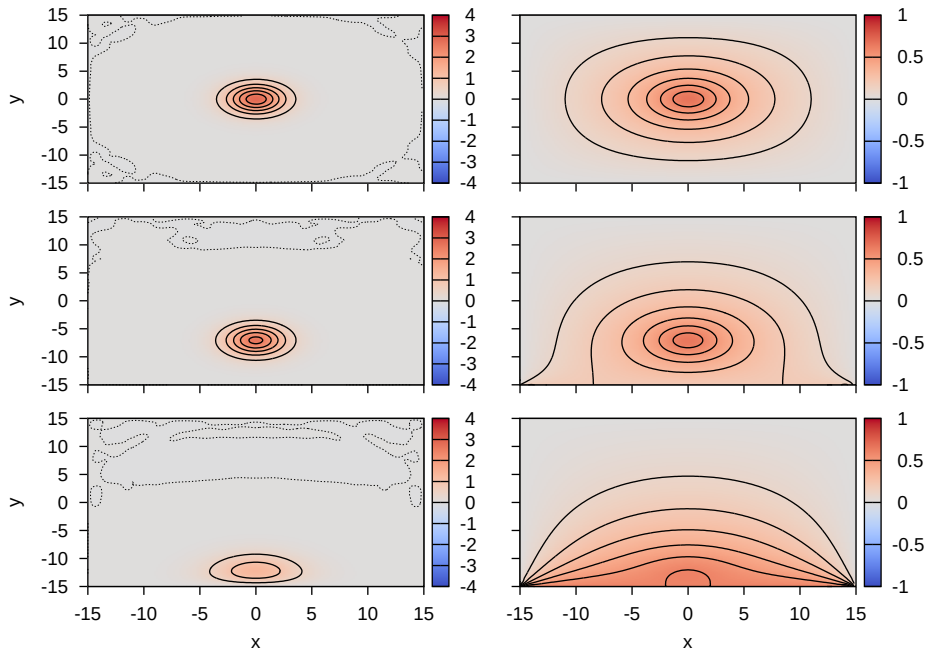

Figure 3.7: Thermal solitary waves, large Biot number case. Shown are the electric field amplitude, u (left column), and temperature, θ (right column), in the (x, y) plane for the cases where $\theta_{B,y} = 0$ (top row), $\theta_{B,y} = 0.2$ (middle row) and $\theta_{B,y} = 0.6$ (bottom row). Contours are positive values at intervals of 0.5 for the u figures, and values at intervals of 0.1 for the θ figures. Solid contours are positive values and the zero contour is dotted. The other parameters are $\beta_y = 100$ and $\mu = 1$.

Figure 3.7 shows thermal solitary wave solutions of (1.23) with boundary conditions (3.1) for one large heat loss boundary and three boundaries at ambient temperature. Shown are contour plots of the electric field amplitude, u, and temperature θ in the (x, y) plane. The three solitary waves are for $\theta_{B,y} = 0$, 0.2 and 0.6. The other parameters are $\beta_y = 100$ and $\mu = 1$. When $\theta_{B,y} = 0$ all four of the cell boundaries are at the same temperature and the solitary wave is symmetric, with the peak of the solitary wave, of amplitude $a = 2.86$, located at the centre of the cell, $(x, y) = (0, 0)$. As the ambient temperature $\theta_{B,y}$ of the warm cell boundary increases, the peak of the solitary wave decreases in amplitude and moves towards the warmer boundary. For the $\theta_{B,y} = 0.2$ case the peak amplitude has decreased to $a = 2.65$ and is located at $(x, y) = (0, -7.0)$. For $\theta_{B,y} = 0.6$ the amplitude has decreased further to $a = 1.35$, while the wave peak has migrated further towards the warmer boundary and is located at $(x, y) = (0, -12.2)$.

Figure 3.8 shows a one dimensional cross-section of the (2+1)-D solitary waves shown in Figure 3.7, taken along the $x = 0$ axis through the centre of the cell. The

behaviour of the solitary wave is qualitatively similar to the (1+1)-D solitary waves in Figure 3.1, but there are some differences. The temperature profile is not linear away from the solitary wave peak in the (2+1)-D case, due to two dimensional heat diffusion, and higher values of $\theta_{B,y}$ are needed at the boundary to achieve the same offset from a centred wave position.

To further consider the difference in θ profiles between the (1+1)-D and (2+1)-D cases we can make use of the fact that $u \approx 0$ for regions of the cell a moderate distance from the solitary wave peak. In the (1+1)-D case the temperature equation in (1.23) reduces to $\theta_{xx} = 0$, which implies a linear solution of the form $\theta = Ax + B$ in this field region. In the (2+1)-D case the temperature equation of (1.23) reduces to $\theta_{xx} + \theta_{yy} = 0$, which can (ignoring the square cell geometry) be converted to the form $\theta_{rr} + \frac{1}{r}\theta_r = 0$ in polar coordinates. Hence $\theta = A\ \ln(r) + D$, indicating an approximately logarithmic profile in the region where u is small.

The peak values of u and θ are co-located for small values of $\theta_{B,y}$. However, for large values of $\theta_{B,y}$ this is not the case. It may also be noted that for small values of $\theta_{B,y}$ the gradient of θ is positive at the warm cell boundary, indicating heat flow from the cell. For the $\theta_{B,y} = 0.6$ case the gradient is nearly zero. For the small $\theta_{B,y}$ the electric field is large, causing significant internal heating of the medium, with the heat lost at the cell boundary. For the $\theta_{B,y} = 0.6$ case the electric field and the internal heating is smaller, leading to near equilibrium between the medium and the warm cell boundary.

Figures 3.9 and 3.10 show the thermal wave solitary solutions for (1.23), with a mixed boundary condition (3.1) with low heat loss ($\beta_y = 0.2$). In Figure 3.9 contour plots of electric field amplitude u and temperature θ are shown in the (x, y) plane. The three solitary waves are, from top to bottom, for $\theta_{B,y} = 0$, 0.2 and 0.6. The other parameters are the same as in Figure 3.7, except for the Biot number at the mixed boundary, which is small. In this case when $\theta_{B,y} = 0$ the steady state temperature at the warm cell boundary is $\theta(-15) = 0.1$, while the peak of the solitary wave, amplitude $a = 2.77$, is located at $(x, y) = (0, -2.83)$. This wave shows a number of differences compared with the $\theta_{B,y} = 0$ large Biot number case shown in Figure 3.7. The wave is non-symmetric, being located closer to the warm cell boundary, and the amplitude is slightly lower. As $\theta_{B,y}$ increases the temperature at the warm cell

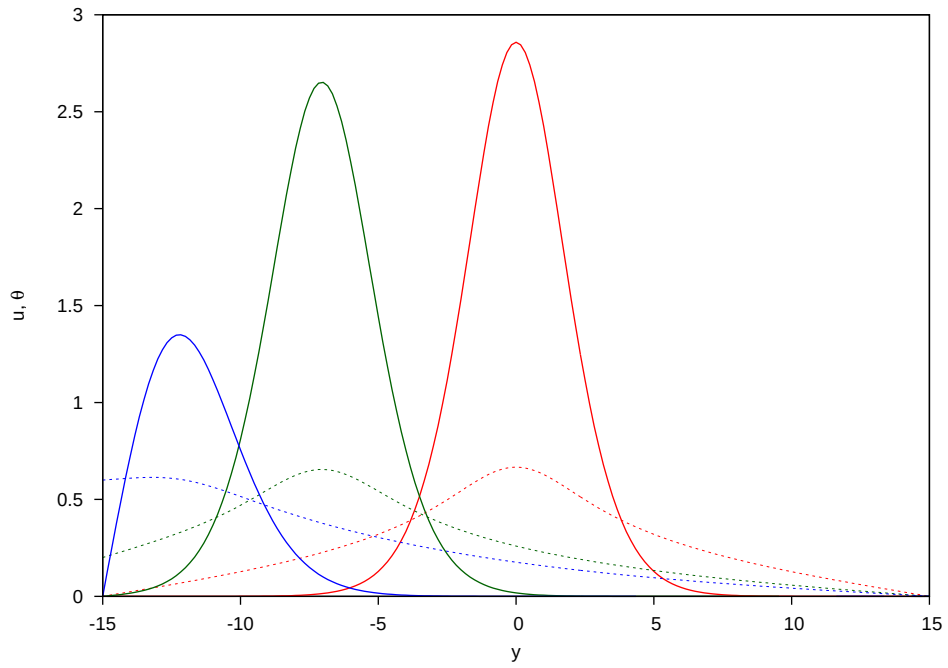

Figure 3.8: One dimensional cross-section of (2+1)-D thermal solitary waves, taken along $x = 0$, large Biot number case. Shown are the electric field amplitude, u (solid), and temperature, θ (dashed), versus y. The three solitary waves are $\theta_{B,y} = 0$ (red, centre), $\theta_{B,y} = 0.2$ (green, slightly offset) and $\theta_{B,y} = 0.6$ (blue, near boundary). The other parameters are $\beta_y = 100$ and $\mu = 1$.

boundary increases and approaches $\theta_{B,y}$, and, as in the large Biot number case, the solitary waves decrease in amplitude and migrate closer to the warm cell boundary. For the $\theta_{B,y} = 0.2$ case the wave amplitude is $a = 2.58$ and the wave is located at $(x, y) = (0, -11.0)$. For the $\theta_{B,y} = 0.6$ case the wave amplitude has decreased to $a = 1.80$ with the peak location $(x, y) = (0, -12.3)$ close to the cell boundary.

Figure 3.11 shows the location of the thermal solitary wave peak, ζ_y, along the $x = 0$ cell axis versus the ambient temperature $\theta_{B,y}$ at the warmer cell boundary, $y = -15$, with $\mu = 1$. Shown are curves corresponding to $\beta_y = 0.2, 0.6$ and 100, with the $\beta_y = 100$ case very close to the result obtained as the Biot number $\beta_y \to \infty$. As the ambient temperature at the cell boundary is increased, the thermal solitary wave migrates towards the warmer boundary, approaching $\zeta_y \approx -12.7$. Increasing the ambient temperature causes the amplitude of the solitary wave to decrease to zero, suggesting that no solitary wave solution exists once the thermal gradient between cell boundaries becomes too large. For a given ambient temperature at the mixed boundary, decreasing the Biot number also causes the thermal solitary wave to shift towards the warmer boundary. These results are qualitatively similar to

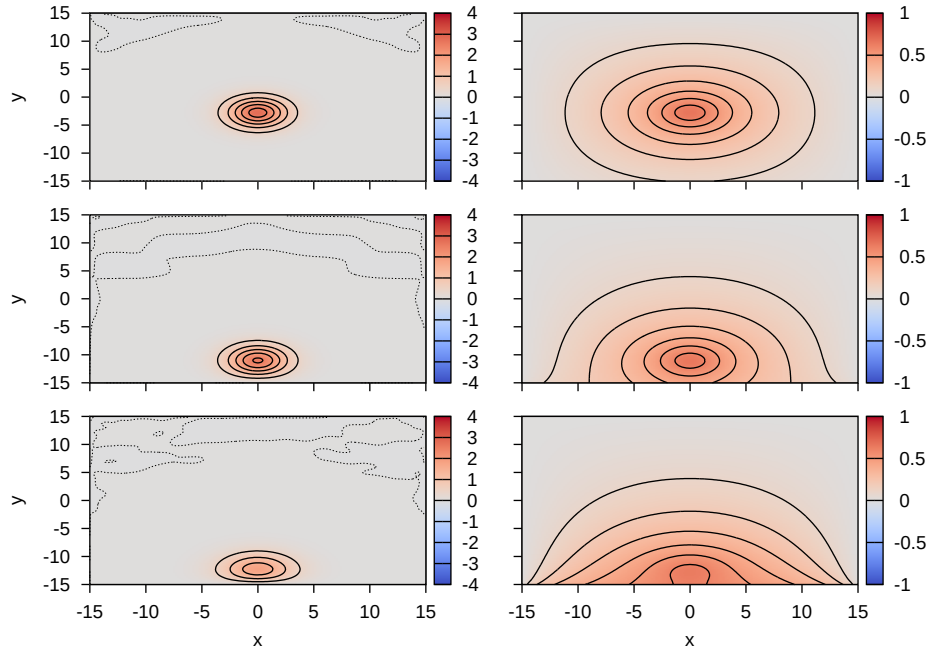

Figure 3.9: Thermal solitary waves, small Biot number case. Shown are the electric field amplitude, u (left column), and temperature, θ (right column), for the cases where $\theta_{B,y} = 0$ (top row), $\theta_{B,y} = 0.2$ (middle row) and $\theta_{B,y} = 0.6$ (bottom row). Contours are positive values at intervals of 0.5 for the u figures, and values at intervals of 0.1 for the θ figures. Solid contours are positive values and the zero contour is dotted. The other parameters are $\beta_y = 0.2$ and $\mu = 1$.

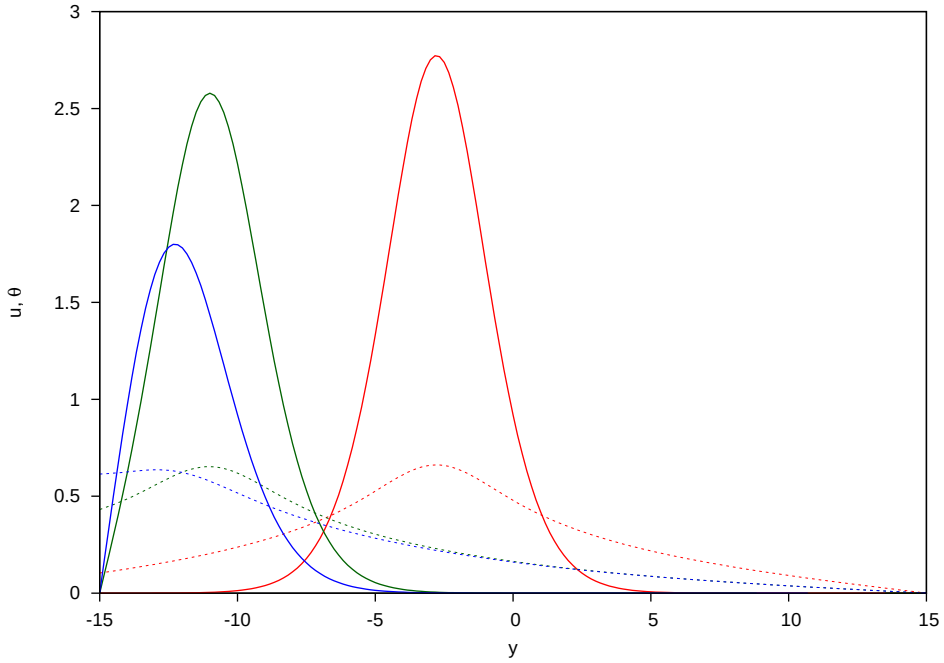

Figure 3.10: One dimensional cross-section of (2+1)-D thermal solitary waves, taken along $x = 0$, small Biot number case. Shown are the electric field amplitude, u (solid), and temperature, θ (dashed), versus y. The three solitary waves are $\theta_{B,y} = 0$ (red, centre), $\theta_{B,y} = 0.2$ (green, slightly offset) and $\theta_{B,y} = 0.6$ (blue, near boundary). The other parameters are $\beta_y = 0.2$ and $\mu = 1$.

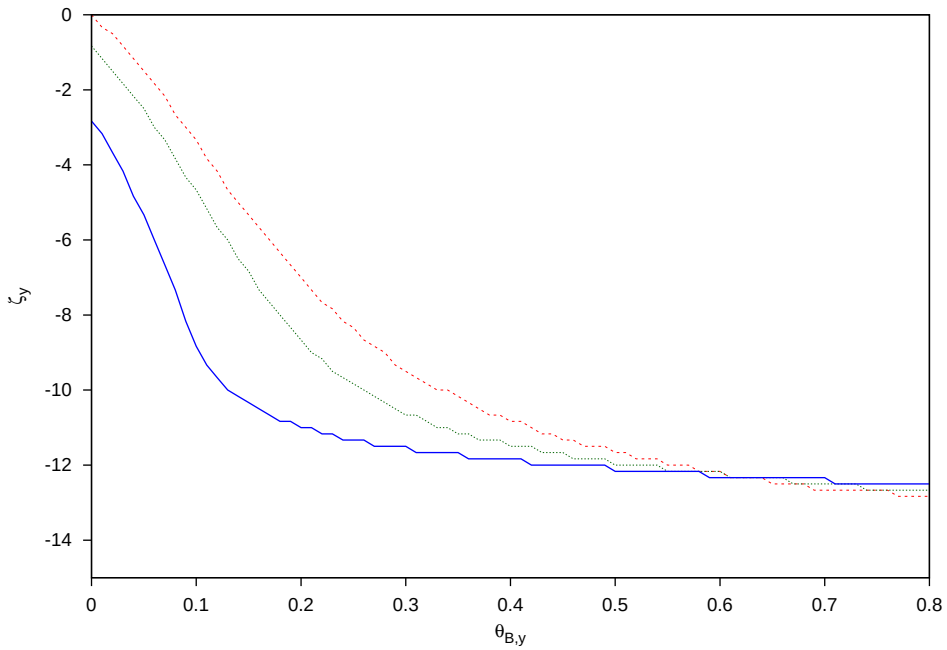

Figure 3.11: (Colour online) Location of the peak of thermal solitary wave, ζ_y, versus the ambient temperature, $\theta_{B,y}$, for $\mu = 1$. The curves correspond to $\beta_y = 0.2$ (solid line, dark blue); $\beta_y = 0.6$ (dotted line, green); $\beta_y = 100$ (dashed line, red).

the (1+1)-D solitary wave case of Figure 3.3, with both showing that the solitary wave positions approach a location around 80% of the distance to the cell boundary. However, the migration towards the boundary appears to be faster with respect to increasing $\theta_{B,y}$ in the (2+1)-D case.

Figure 3.12 shows the amplitude of the thermal solitary wave, a, versus the ambient temperature, $\theta_{B,y}$, for $\mu = 1$. The curves correspond to $\beta_y = 0.2, 0.6$ and 100. For a given choice of Biot number the solitary wave amplitude decreases as $\theta_{B,y}$ increases. The solitary wave amplitude decreases to $a \approx 0$ at a given value of $\theta_{B,y}$, after which thermal solitary waves do not exist. This threshold value of $\theta_{B,y}$ decreases as the Biot number increases, in particular it decreases from $\theta_{B,y} = 1.04$ for $\beta_y = 0.2$ to $\theta_{B,y} = 0.71$ for $\beta_y = 10$. Hence, if the heat loss rate at the Newton cooling boundary is too great, then a solitary wave cannot exist. This result is similar to the (1+1)-D case shown in Figure 3.4, with the main difference that the value of $\theta_{B,y}$ for which the solitary wave amplitude reaches zero for a given value of Biot number is higher in the (2+1)-D case.

Figure 3.13 shows the first order excited state solitary wave solutions of (1.23) and (1.22). Shown are contour plots of the electric field u and temperature θ in

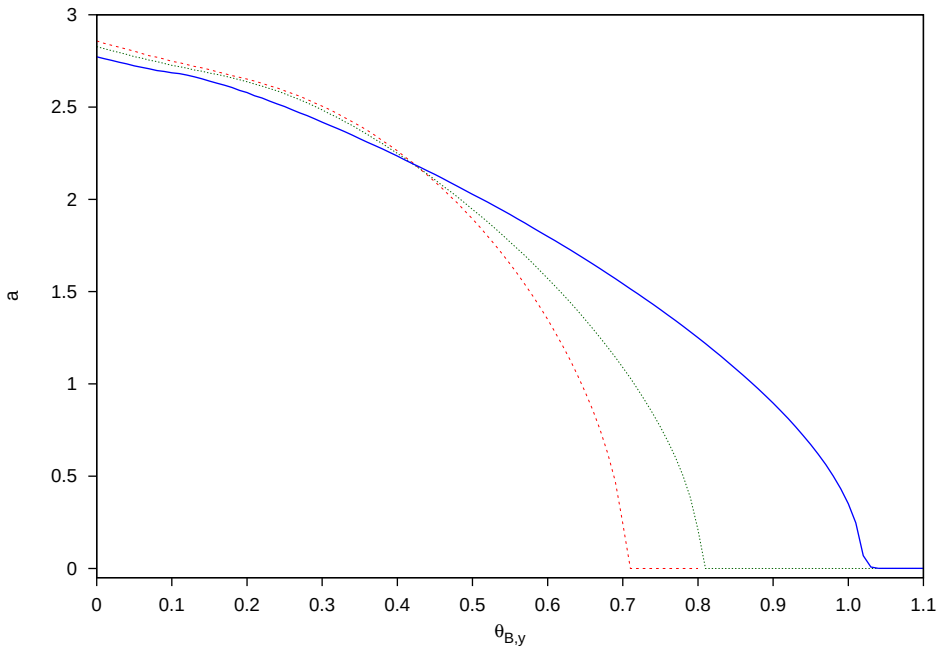

Figure 3.12: Amplitude of the thermal solitary wave, a, versus the ambient temperature, $\theta_{B,y}$, for $\mu = 1$. The curves correspond to $\beta_y = 0.2$ (solid line, dark blue), $\beta_y = 0.6$ (dotted line, green), and $\beta_y = 100$ (dashed line, red).

the (x, y) plane. The three solitary waves are for $\theta_{B,y} = 0, 0.1$ and 0.2. The other parameters are $\beta_y = 100$ and $\mu = 0.1$. As $\theta_{B,y}$ increases, the structure of the electric field amplitude, u, changes. For $\theta_{B,y} = 0$ the solitary wave is symmetric, with a single maximum $a = 1.11$ at $(x, y) = (0, 0)$, and an annular shaped minima at $a = -0.50$ at a radial distance of $\zeta_r = 0.65$ from the centre of the cell. For $\theta_{B,y} = 0.1$ the solitary wave has a maximum of $a = 0.94$ at $(x, y) = (0, -5.17)$, with three discrete minima. One of the minima is on the $x = 0$ axis, with $a = -0.55$ at $y = 2.17$, while the other two minima both have $a = -0.62$ at locations $(x, y) = (\pm 6.17, -9.0)$. For the $\theta_{B,y} = 0.2$ case the the maximum with $a = 0.45$ is pushed closer to the boundary, at $(x, y) = (0, -6.5)$. There are now two discrete minima, both lying on the $x = 0$ axis, with $a = -0.68$ at $(x, y) = (0, 0.83)$, and $a = -0.60$ at $(x, y) = (0, -12.17)$. In contrast to the electric field amplitude, in all cases the temperature response θ has a single maximum. This is a result of the nonlocal heat diffusion, which smoothes out the temperature response for large ν.

Figure 3.14 shows a one dimensional cross-section through $x = 0$ of the (2+1)-D solitary waves shown in Figure 3.13. For the cases where $\theta_{B,y} = 0$ and $\theta_{B,y} = 0.2$ the slice along the $x = 0$ axis passes through the local maxima and minima in

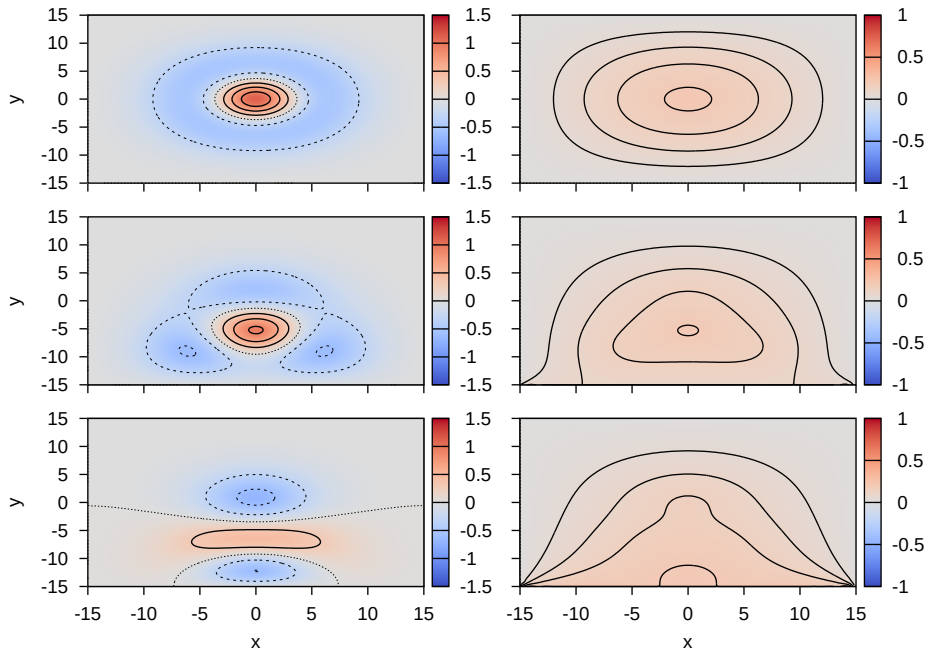

Figure 3.13: Thermal solitary waves, first excited state. Shown are the electric field, u (left column), and temperature, θ (right column), for the cases where $\theta_{B,y} = 0$ (top row), $\theta_{B,y} = 0.1$ (middle row) and $\theta_{B,y} = 0.2$ (bottom row). Contours are values at intervals of 0.3 for the u figures, and values at intervals of 0.05 for the θ figures. Solid contours are positive values, the zero contours are dotted and negative contours are dashed. The other parameters are $\beta_y = 100$ and $\mu = 0.1$.

(x, y) space, so the maximum and minima for Figure 3.14 are as in Figure 3.13. For the $\theta_{B,y} = 0.1$ case, the maximum at $y = -5.17$ and minimum at $y = 2.17$ both correspond to local extrema in Figure 3.13, while the minimum $a = -0.215$ at $y = 11.83$ does not.

Figure 3.15 shows the fundamental solitary wave, and first three excited steady state solitary waves for $\theta_{B,x} = \theta_{B,y} = 0$ and $\beta_x = \beta_y = 0$. The first two excited state solitary waves were obtained by adjusting the propagation constant μ, and the third excited state solitary wave required adjusting both μ and also the amplitude of the initial guess for u and θ provided to the Newton-CG method (from 18 to 380). The fundamental solitary wave (top left) for the case where $\mu = 0.5$ is qualitatively similar to the $\mu = 1$ case shown in Figure 3.7 and Figure 3.9, with maximum amplitude $a = 1.67$, located at the centre of the cell, $(x, y) = (0, 0)$. The first excited state solitary wave (top right), with propagation constant $\mu = 0.1$ is the same as in Figure 3.13, as discussed above. The second excited state solitary wave (bottom left), with propagation constant $\mu = 0.04$, has five maxima and four minima. The absolute

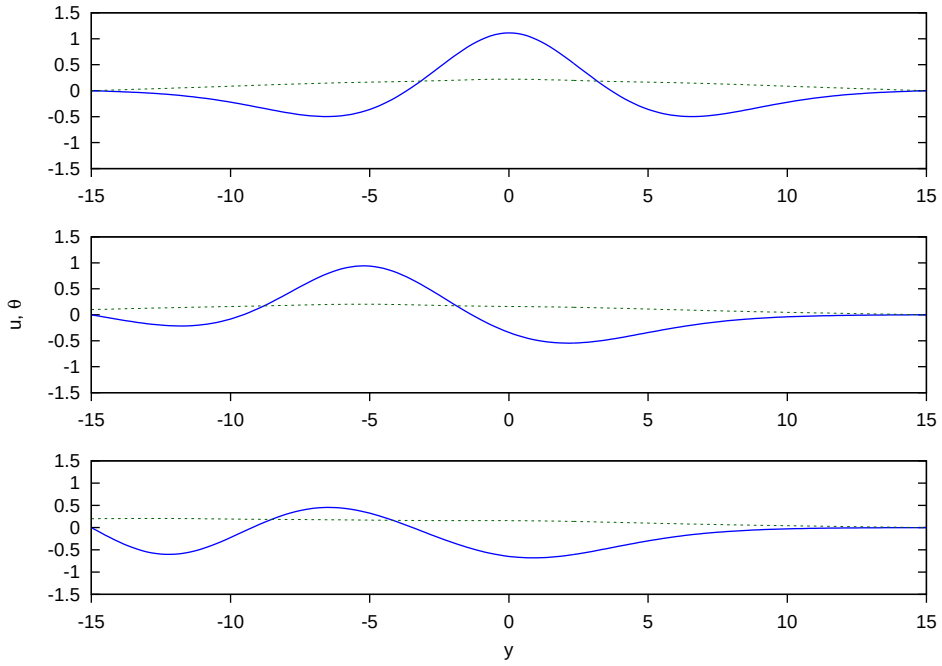

Figure 3.14: One dimensional cross-section of (2+1)-D excited state thermal solitary waves. Shown are the electric field amplitude, u (solid), and temperature, θ (dashed), versus y. The three solitary waves are $\theta_{B,y} = 0$ (red, centre), $\theta_{B,y} = 0.1$ (green, slightly offset) and $\theta_{B,y} = 0.2$ (blue, near boundary). The other parameters are $\beta_y = 100$ and $\mu = 0.1$.

maximum is $a = 0.88$ at the centre of the cell, $(x, y) = (0, 0)$, with the other four local maxima $a = 0.651$ located symmetrically at $(x, y) = (\pm 10.2, 0)$ and $(x, y) = (0, \pm 10.2)$. The four minima $a = -0.592$ are located at $(x, y) = (\pm 4.3, \pm 4.3)$. The third excited state solitary wave (bottom right), with propagation constant $\mu = 0.0001$, has five maxima and eight local minima. The absolute maxima is $a = 0.97$ at the centre of the cell, $(x, y) = (0, 0)$, with the other four local maxima $a = 0.64$ located at $(x, y) = (\pm 5.8, \pm 5.8)$. There are a set of four local minima $a = -0.67$ located at $(x, y) = (\pm 5.2, 0)$ and $(x, y) = (0, \pm 5.2)$ and another set of four minima $a = -0.795$ located at $(x, y) = (\pm 10.2, \pm 10.2)$.

3.2.2 Two adjacent boundaries with non-zero ambient temperature

In this section we consider the scenario of two adjacent sides with a mixed boundary condition, $x = y = -\frac{L}{2}$, with the other two boundary conditions at the ambient

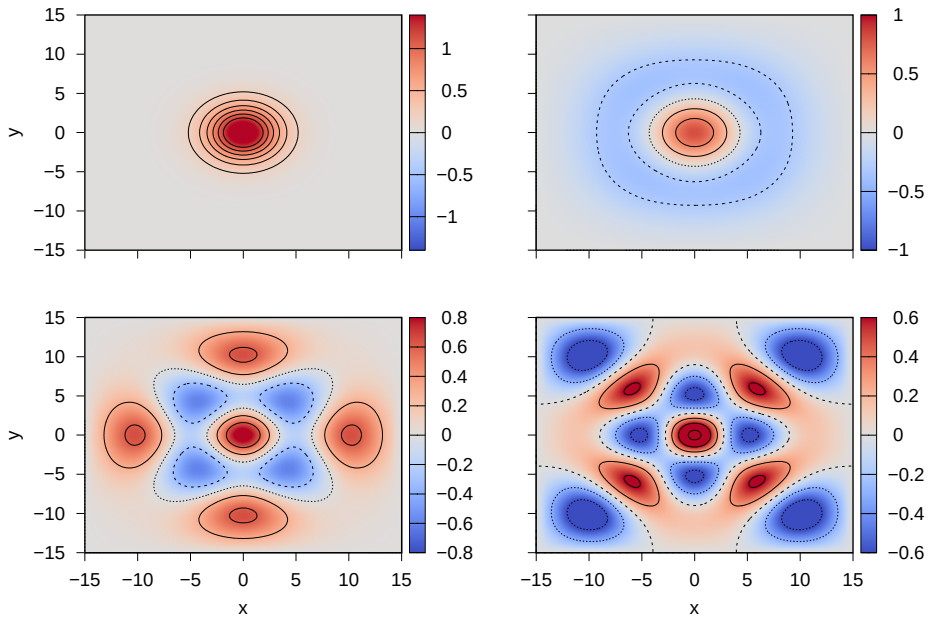

Figure 3.15: Fundamental and higher order solitary waves. Shown is the electric field amplitude, u, in the (x, y) plane for the cases where $\mu = 0.5$ (top left), $\mu = 0.1$ (top right), $\mu = 0.04$ (bottom left) and $\mu = 0.0001$ (bottom right). Contours are positive values at intervals of 0.3, where solid contours are positive values, the zero contour is dotted and negative contours ar dashed. The other parameters are $\beta_x = \beta_y = 100$.

temperature. The boundary conditions are as in (1.24) for u, and for θ are

$$\begin{aligned} \theta = 0, \quad \text{at} \quad x = \frac{L}{2}, \quad y = \frac{L}{2}, \\ \theta_x - \beta_x \left(\theta - \theta_{B,x}\right) = 0, \quad \text{at} \quad x = -\frac{L}{2}, \\ \theta_y - \beta_y \left(\theta - \theta_{B,y}\right) = 0, \quad \text{at} \quad y = -\frac{L}{2}. \end{aligned} \tag{3.2}$$

Figure 3.16 shows two thermal solitary waves cases with Newton cooling on two adjacent boundaries. Shown are the electric field, u, and the temperature, θ for a ground state solitary wave with $\theta_{B,y} = 0.5$, $\theta_{B,x} = 0.3$ and $\mu = 1$, and for the first excited state solitary wave with $\theta_{B,y} = 0.2$, $\theta_{B,x} = 0.1$ and $\mu = 0.1$. The other parameters are $\beta_y = \beta_x = 100$. This choice of boundary conditions pushes the peak of the thermal solitary wave towards the corner of the cell at $(x, y) = (-15, -15)$. The peak amplitude is $a = 1.45$ at $(x, y) = (-4.17, -11.17)$, which is almost, but not quite, co-located with the maximum cell temperature $\theta_{max} = 0.59$. For the first excited state the structure of the electric field amplitude, u, is complicated, with two main local maxima and two local minima. The main solitary wave maximum of

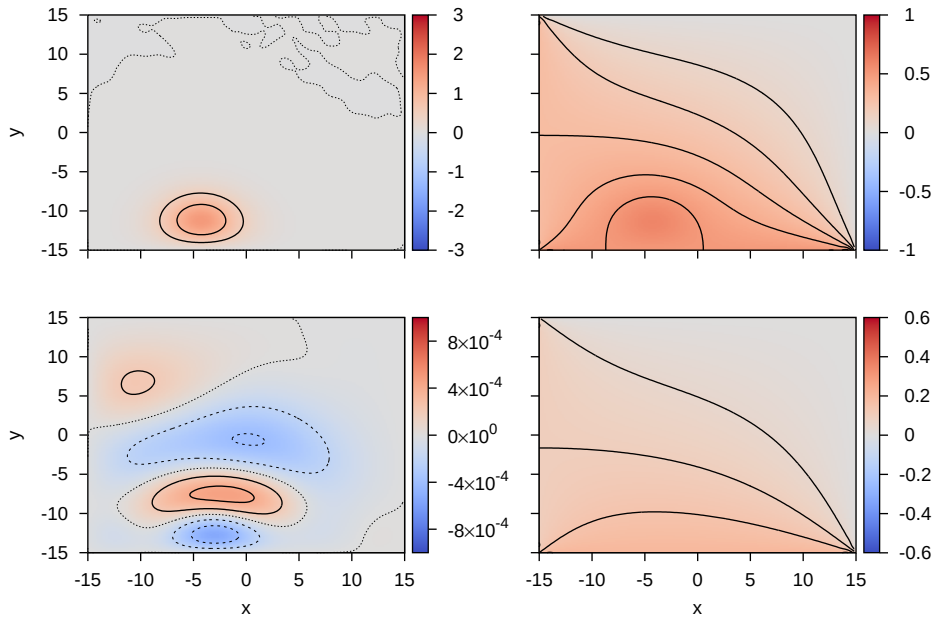

Figure 3.16: Thermal solitary waves, case with Newton cooling on two adjacent boundaries. Shown are the electric field, u (left column), and temperature, θ (right column). The top row shows the ground state soliton with $\theta_{B,y} = 0.5$ and $\theta_{B,x} = 0.3$ and $\mu = 1$, while the bottom row shows the first excited state soliton with $\theta_{B,y} = 0.2$ and $\theta_{B,x} = 0.1$ with $\mu = 0.1$. The other parameters are $\beta_x = \beta_y = 100$ (on both boundaries). Contours are at intervals of 0.5 for the top left figure, 0.1 for top right, 2×10^{-4} for the bottom left and 0.05 for the bottom right. Solid contours are positive values, the zero contour is dotted and negative contours are dashed.

$a = 4.61 \times 10^{-4}$ is at $(x, y) = (-2.0, -7.5)$, with another maximum $a = 2.2 \times 10^{-4}$ at $(x, y) = (-10.3, 6.7)$. The minima are $a = -4.11 \times 10^{-4}$ at $(x, y) = (0.17, -0.5)$ and $a = -5.36 \times 10^{-4}$ at $(x, y) = (-3.0, -12.67)$. As with the excited state solitary wave solutions in Figure 3.13, the temperature response θ has a single maximum as a result of the large thermal conductivity ν.

Figure 3.17 shows the amplitude, a, of the ground state thermal solitary wave in $(\theta_{B,x}, \theta_{B,y})$ parameter space, while Figure 3.18 shows the position of the ground state thermal solitary wave for values in $(\theta_{B,x}, \theta_{B,y})$ parameter space, with offset along the x-axis (ζ_x) and offset along the y-axis (ζ_y). The other parameters are $\beta_x = \beta_y = 100$. As expected, increasing $\theta_{B,x}$ or $\theta_{B,y}$ causes the amplitude of the solitary wave to decrease, as well as causing its peak to migrate towards the respective cell boundaries. The solitary wave response is symmetric about the line $\theta_{B,x} = \theta_{B,y}$, but the value of $r = \sqrt{\theta_{B,x}^2 + \theta_{B,y}^2}$ at which the solitary wave amplitude a reaches zero is not constant. The values of r at which $a = 0$ range from $r = 0.71$ along the

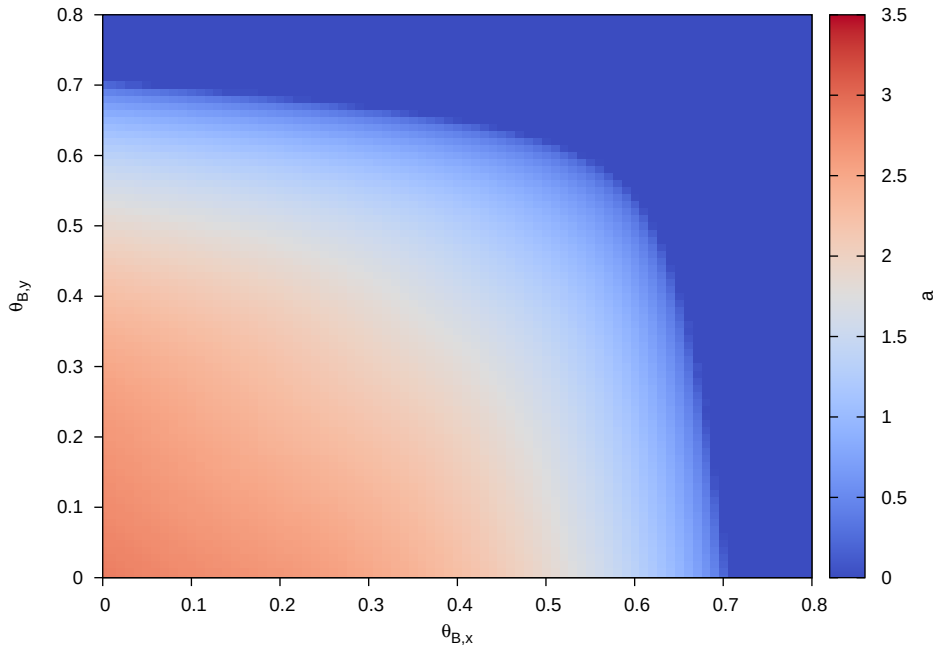

Figure 3.17: Amplitude, a, of the ground state thermal solitary wave for values in $(\theta_{B,x}, \theta_{B,y})$ parameter space. The other parameters are $\beta_x = \beta_y = 100$.

$\theta_{B,x} = 0$ and $\theta_{B,y} = 0$ axes in Figure 3.17 to $r = 0.83$ for $\theta_{B,x} = \theta_{B,y} = 0.59$, with the difference in values likely a result of the square cell geometry.

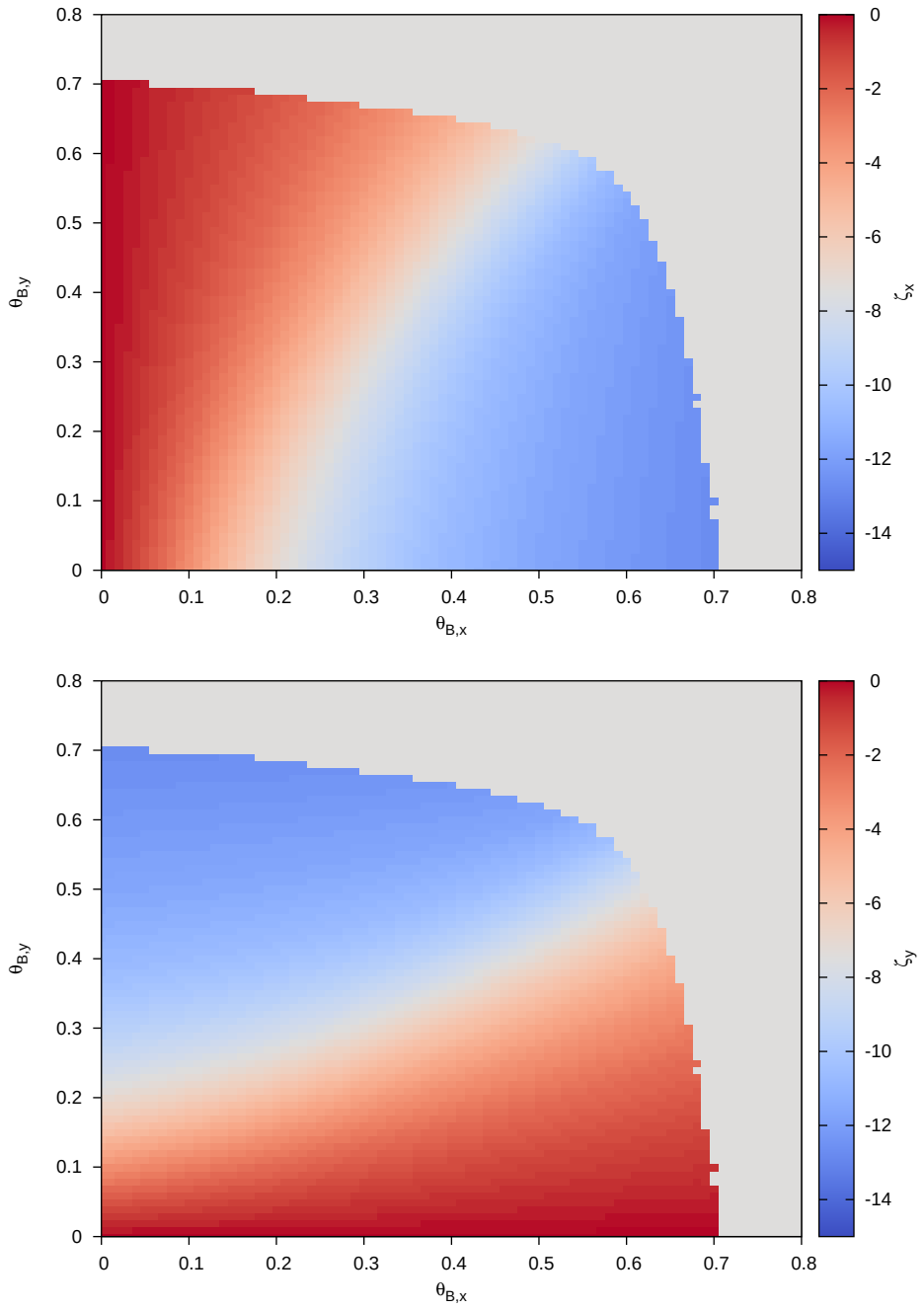

Figure 3.18: Position of the ground state thermal solitary wave for values in $(\theta_{B,x}, \theta_{B,y})$ parameter space. a) shows offset along the x-axis, ζ_x and b) shows offset along the y-axis ζ_y. The other parameters are $\beta_x = \beta_y = 100$. Location is not shown where $a < 10^{-2}$.

Chapter 4

Stability for Thermal Solitary Waves

The stability of the thermal solitary waves is now investigated in both (1+1)-D and (2+1)-D, both analytically and numerically, using three different methods. All the results presented in this section are for the case of a single cell boundary with non-zero ambient temperature, as described in section 3.1 for the (1+1)-D case, and at the start of section 3.2.1 with boundary condition (3.1) for the (2+1)-D case. All examples presented in this section use the parameter $\nu = 100$, with $\beta_x = \beta_y = 100$. So the presented results explore the effect of the boundary temperature $\theta_{B,y}$ and propagation constant μ on stability. The results for the (1+1)-D case, in section 4.2, are presented in [73], while the results for the (2+1)-D case, in section 4.3, are presented in [72].

4.1 Methods

4.1.1 Vakhitov-Kolokolov (VK) Stability Criterion

The stability of the thermal solitary waves is investigated using the Vakhitov-Kolokolov (VK) method. The self-focussing mechanism for these solitary waves derives from the increase of the refractive index of the medium with the temperature increase due to the optical heating. This relationship is analogous to the optical Kerr effect and can result in MI of a perturbed propagating solitary wave. To investigate this, power versus propagation constant curves are calculated for the families

of thermal solitary waves given by (1.23). The optical power in the (2+1)-D case,

$$P = \int_{-L/2}^{+L/2} \int_{-L/2}^{L/2} |E|^2 \, dxdy, \tag{4.1}$$

is calculated using the numerical solitary wave solutions found using the Newton-CG method. The VK stability criterion [62] is a necessary, but not sufficient, condition for MS of solitary wave solutions of generalised NLS equations on an infinite domain. The condition is that the solution falls within a region of parameter space for which the power versus propagation constant curve has positive slope ($\frac{dP}{d\mu} > 0$), see, for example, [42, 43, 56]. This result has not been theoretically proven for the governing equations (1.15)–(1.22), which is an NLS-type system on a finite domain, but the results presented here are consistent with the infinite domain theory. Assessment of the VK stability criterion in the (1+1)-D case is the same, but for the 1D optical power (2.6) and the corresponding governing equations (1.25).

4.1.2 Spectral Stability Analysis

In Section 4.1.1 the VK condition, a necessary condition for MS of thermal solitary waves, was examined. However, it is still possible that amplitude or drift instabilities may occur, see [54]. To assess this possibility, we shall use a linearized stability analysis following the technique outlined in [112]. Instabilities occur if there are negative eigenvalues. In this analysis a perturbation to the steady state solution is expressed as a superposition of linear modes. Note that we are not considering perturbations resulting from the boundary conditions. We hence express u and θ as

$$u = u_s + \epsilon((v-w)e^{\imath\lambda z} + (v^*+w^*)e^{-\imath\lambda^* z})e^{\imath\mu z}, \quad \theta = \theta_s + \epsilon\Theta(e^{\imath\lambda z} + e^{-\imath\lambda^* z}), \tag{4.2}$$

where u_s and θ_s are the steady state solutions and ϵ is a small parameter. Calculating the components of (1.23), eliminating steady state terms at $O(1)$ and higher order

terms in ϵ we obtain

$$\begin{aligned} \imath u_z &= -\epsilon(\mu+\lambda)(v-w)e^{\imath\lambda z} + \epsilon(-\mu+\lambda^*)(v^*+w^*)e^{-\imath\lambda^* z}, \\ \frac{1}{2}\nabla^2 u &= \frac{1}{2}\epsilon(\nabla^2 v - \nabla^2 w)e^{\imath\lambda z} + \frac{1}{2}\epsilon(\nabla^2 v^* + \nabla^2 w^*)e^{-\imath\lambda^* z}, \\ 2\theta u &= 2\epsilon\theta_s((v-w)e^{\imath\lambda z} + (v^*+w^*)e^{-\imath\lambda^* z}) + 2\epsilon u_s\Theta(e^{\imath\lambda z} + e^{-\imath\lambda^* z}) \end{aligned} \tag{4.3}$$

Combining the components gives

$$\begin{aligned} &[(-\mu-\lambda)(w-v) + \frac{1}{2}(\nabla^2 v - \nabla^2 w) + 2\theta_s(v-w) + 2u_s\Theta]e^{\imath\lambda z} \\ &+[(-\mu+\lambda^*)(v^*+w^*) + \frac{1}{2}(\nabla^2 v^* + \nabla^2 w^*) + 2\theta_s(v^*+w^*) + 2u_s\Theta]e^{-\imath\lambda^* z} = 0 \end{aligned} \tag{4.4}$$

So,

$$(-\mu-\lambda)(w-v) + \frac{1}{2}(\nabla^2 v - \nabla^2 w) + 2\theta_s(v-w) + 2u_s\Theta = 0 \tag{4.5}$$

To set this into the appropriate form for an eigenvalue problem, we need to eliminate the temperature perturbation Θ. Substituting the perturbation expansions for u and θ into the temperature equation of (1.23) gives,

$$\nu(\nabla^2\Theta e^{\imath\lambda z} + \nabla^2\Theta e^{-\imath\lambda^* z}) + 4u_s(ue^{\imath\lambda z} + u^* e^{-\imath\lambda^* z}) = 0 \tag{4.6}$$

Taking the coefficients of $e^{\imath\lambda z}$ from (4.6) and solving for Θ gives

$$\nu\nabla^2\Theta + 4u_s u = 0, \tag{4.7}$$

which implies

$$\Theta = [\nabla^2]^{-1}\frac{4u_s u}{\nu}. \tag{4.8}$$

Then substituting (4.8) back into (4.5) and converting to the form of the eigenvalue problems $L_0 v = \lambda w$ and $L_1 w = \lambda v$, we find

$$L_0 = (\mu - \frac{1}{2}\nabla^2 - 2\theta_s - \frac{8u_s^2}{\nu}[\nabla^2]^{-1}), \quad L_1 = (\mu - \frac{1}{2}\nabla^2 - 2\theta_s). \tag{4.9}$$

Now substituting $L_1 w = \lambda v$ into $L_0 v = \lambda w$ produces

$$L_0 L_1 w = \lambda^2 w. \tag{4.10}$$

We require the eigenvalues, λ^2 to be all positive for stability. The eigenvalues of $L_0 L_1$ were calculated for a range of parameters. We found that the matrix $L_0 L_1$ typically had condition number of $O(10^{10})$, indicating that the eigenvalue problem is very ill-conditioned. Standard single and double precision variable types can provide 7 or 16 decimal digits of precision, respectively. Rounding errors introduced in the derivation of the eigenvalues meant that these precisions were found not to be sufficient to calculate all minimum eigenvalues accurately. In many cases the error in the computed minimum eigenvalue is sufficient that its sign would be incorrect, leading to an incorrect inference about the stability of the solitary wave system. To determine a suitable numerical precision to use for calculating the minimum eigenvalues, a number of cases were tested using the BigFloat type in the Julia language, which is based on the GNU MFPR library (multiple-precision binary floating-point library with correct rounding) [44].

Figure 4.1 shows the minimum eigenvalue, $log(|\lambda^2|)$, versus numerical floating point precision for two (2+1)-D cases, $\mu = 0.5$ and 1. The other parameter is $\theta_{B,y} = 0$. Note that in Figures 4.1, 4.4-4.5 and 4.10-4.11, which show minimum eigenvalues, the plots are constructed to display the negative and positive eigenvalues on a log scale by first taking the absolute value. The upper panel in each plot represents the region where the minimum eigenvalue λ^2 is positive, while the bottom panel shows the region where λ^2 is negative. There is a discontinuity on the y axis, given by a solid line, representing the transition from negative to positive values.

The case $\mu = 1$ has a negative minimum eigenvalue for all precisions, converging to a value of $\lambda^2 = -4.9319 \times 10^{-2}$. In this case the solution converged to a consistent result to 5 significant digits with a numerical precision of 64 bits. For the case where $\mu = 0.5$ the standard single precision of 32 bits resulted in an incorrect sign of the computed minimum eigenvalue, with convergence to a value of $\lambda^2 = 1.08975 \times 10^{-8}$ to 5 significant digits occurring at a numerical precision of 64 bits. Based on these trials the minimum eigenvalues were calculated using numerically extended precision to 128 bits, to ensure that rounding errors did not have a significant impact. The use of extended precision added significantly to the computation costs for these calculations, as a result of the extra overheads inherent in these variable types in programming languages.

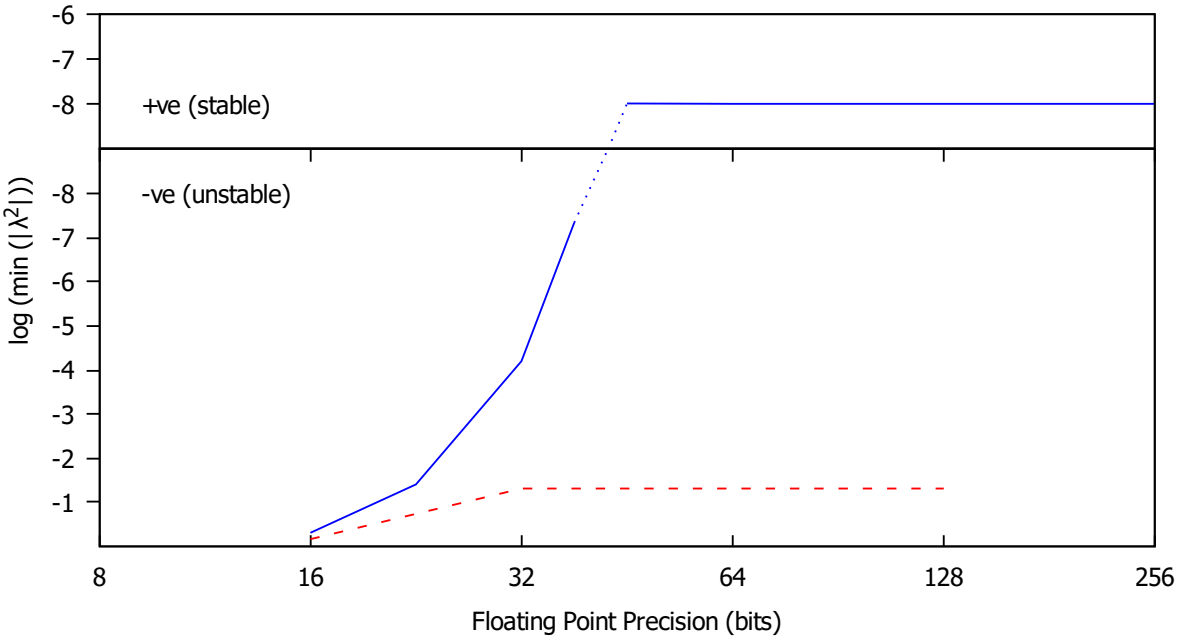

Figure 4.1: Minimum eigenvalue, plotted as $log(|\lambda^2|)$, versus numerical floating point precision for ground state thermal solitary waves. The parameters are $\theta_{B,y} = 0$ and $\mu = 1$: red (dashed) line; $\mu = 0.5$ blue (solid) line.

4.1.3 Numerical Simulations

The analytical stability predictions in Sections 4.1.1 and 4.1.2 are compared with the results of numerical simulations of the original governing thermal system (1.15)–(1.22), using the numerical steady state solution, with a small perturbation added, as an initial condition. The initial condition used for the (2+1)-D case is then

$$E(x, y, 0) = u_s(x, y) + \epsilon_0 \times \phi(x, y), \theta(x, y, 0) = \theta_s(x, y), \tag{4.11}$$

where $u_s(x, y)$ and $\theta_s(x, y)$ are the thermal solitary wave solution found using the Newton-CG method. The ϕ function generates a random normally distributed value between 0 and 1 for all x and y. For the examples considered below, ϵ_0 is taken as 0.01, or about 0.3% of the amplitude of the solitary wave in the (2+1)-D simulations and about 0.5% of the amplitude of the solitary wave in the (1+1)-D case. The numerical solution of the electric field equation is obtained using a hybrid numerical method, where the spatial derivatives are discretized using central finite differences and the fourth order Runge-Kutta method is used to advance in the time-like variable

z. Gauss-Seidel iteration is used to solve for the temperature at each z-step [13]. The spatial discretizations used are $\Delta z = 0.03$ and $\Delta x = \Delta y = 0.682$ for the (2+1)-D case and $\Delta x = 0.33$ for the (1+1)-D case.

4.2 (1+1)-D System Stability

Figure 4.2 shows the power P versus propagation constant μ curve for (1+1)-D ground state thermal solitary waves. The three curves correspond to $\theta_{B,x} = 0$, 0.2 and 0.4. For non-zero ambient temperature $\theta_{B,x}$ the solitary wave solution branch only exists over a finite range of μ. All three curves are monotonic with positive slope indicating that, for a given value of the ambient temperature, there is a single stable solution branch. Figure 4.3 shows the power P versus propagation constant μ for ground and excited state thermal solitary waves, with $\theta_{B,x} = 0.2$. The three curves correspond to the ground state and the first two excited states. In all three cases the curves are monotonic with positive slope, indicating MS across the entire range of μ values for both the ground and excited state solitary waves. Hence, it is predicted that the thermal solitary waves are stable for all possible parameter values.

Figure 4.4 shows the minimum eigenvalue, $\log(\lambda^2)$, versus boundary temperature $\theta_{B,x}$ for $\mu = 1.0, 0.7$ and 0.5 for the (1+1)-D steady state solitary wave. All eigenvalues are positive (where the solution exists), showing that the solitary wave is stable for all values of $\theta_{B,x}$ where the steady state solution is non-zero. In each case, the minimum eigenvalue increases with increasing $\theta_{B,x}$ to a maximum value, then decreases until the amplitude of the solitary wave becomes zero. For $\mu = 0.5$ with $\theta_{B,x} > 0.3$ and $\mu = 0.7$ with $\theta_{B,x} > 0.42$ the steady state solution has zero amplitude. For $\mu = 1.0$ the minimum eigenvalue reaches a maximum of 3.9×10^{-4} at $\theta_{B,x} = 0.52$, for $\mu = 0.7$ the maximum is 2.2×10^{-4} at $\theta_{B,x} = 0.38$, and for $\mu = 0.5$ the maximum is 1.3×10^{-4} at $\theta_{B,x} = 0.26$.

Figure 4.5 shows the minimum eigenvalue, $\log(\lambda^2)$, versus propagation constant μ for $\theta_{B,x} = 0, 0.1$ and 0.2 for the (1+1)-D steady state solitary wave. The solitary wave is stable for all values of $\theta_{B,x}$ where the steady state solution is non-zero. In each case, the minimum eigenvalue increases with decreasing μ to a maximum value,

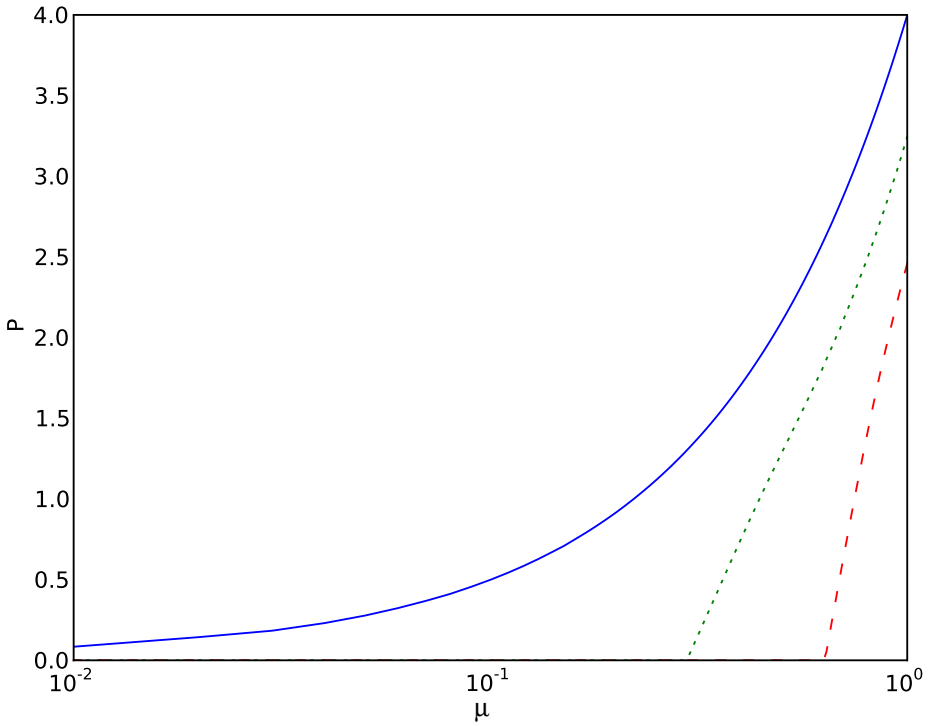

Figure 4.2: Power, P, versus propagation constant μ, for (1+1)-D ground state thermal solitary waves. Shown are $\theta_{B,x} = 0$: blue (solid) line; $\theta_{B,x} = 0.2$: green (dotted) line; $\theta_{B,x} = 0.4$: red (dashed) line.

then decreases until the amplitude of the solitary wave becomes zero for small μ. For $\theta_{B,x} = 0.2$ with $\mu < 0.3125$ the steady state solution has zero amplitude. For $\theta_{B,x} = 0.1$ the smallest eigenvalue reaches a maximum of 2.9×10^{-5} at $\mu = 0.2$, and for $\theta_{B,x} = 0.2$ the maximum is 8.5×10^{-5} at $\mu = 0.39$.

Figure 4.6 shows the electric field amplitude, $|E|$, and temperature, θ, in the (x, z) plane, as given by the full numerical solution of the thermal system (1.25). Shown is the numerical evolution of a perturbed solitary wave, for z up to 10000. The parameters are $\theta_{B,x} = 0.2$ and $\mu = 1$. The initial thermal solitary wave corresponds to a non-symmetric case in Figure 3.1. In this case the thermal solitary wave is a ground state beam centred at $x = -3.19$ with an amplitude of $a = 0.833$. The positions of the peaks of the electric field amplitude $|E|$ and temperature θ both remain steady out to $z = 10000$. The electric field amplitude oscillates between $|E| = 0.844$ and 0.828, indicating a variation of around 1% about the mean. This example corresponds to the parameter choice marked A on Figures 4.4 and 4.5, so

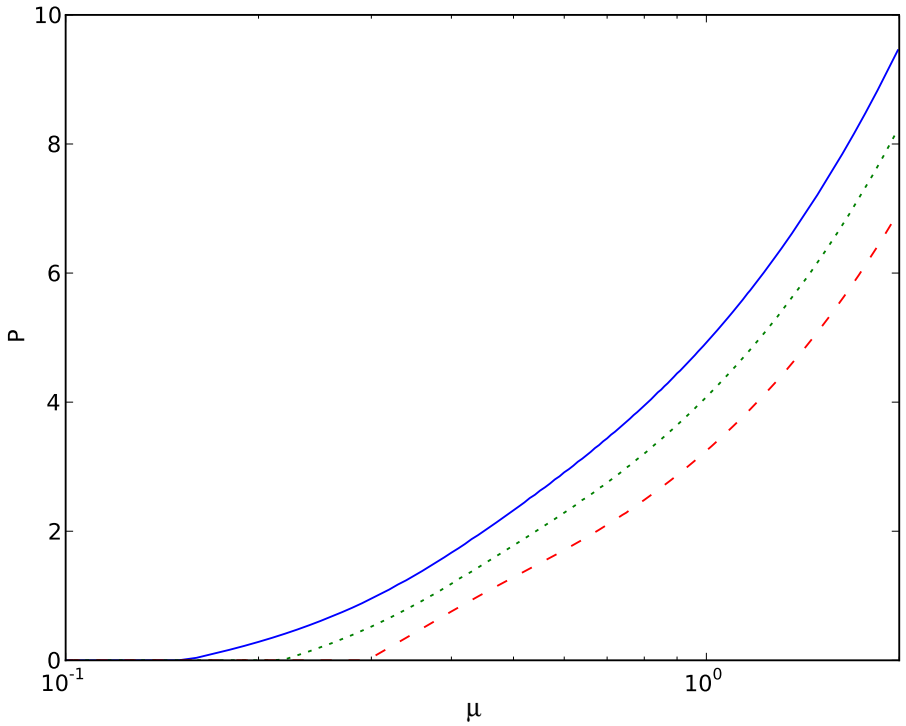

Figure 4.3: Power, P, versus propagation constant, μ, for (1+1)-D ground and excited state thermal solitary waves, with $\theta_{B,x} = 0.2$. Shown are the ground state: red (dashed) line; first excited state: green (dotted) line; second excited state: blue (solid) line.

the spectral analysis has a positive eigenvalue for this case, which implies stability. The theoretical prediction of stability is consistent with the numerical solution.

Figure 4.7 shows the electric field amplitude, $|E|$, and temperature, θ, in the (x, z) plane. Shown is the numerical evolution of a perturbed solitary wave for z up to 10000. The parameters are $\theta_{B,x} = 0.6$ and $\mu = 1$. The initial thermal solitary wave corresponds to the highly non-symmetric case in Figure 3.1. In this example the thermal solitary wave is a ground state beam centred at $x = -11.87$, which is very close to the cell boundary at $x = -15$. In this case, the electric field peak amplitude is $a = 0.217$, which is much lower than the example considered in Figure 4.6 for which the solitary wave peak is near the center of the cell. This is a more challenging example as the position offset is large and the solitary wave is qualitatively quite different to near symmetric solitary waves or those in an infinite domain. There is a variation in $|E|$ of 2% about the mean, which is higher than for the previous example. This example corresponds to the parameter choice marked B

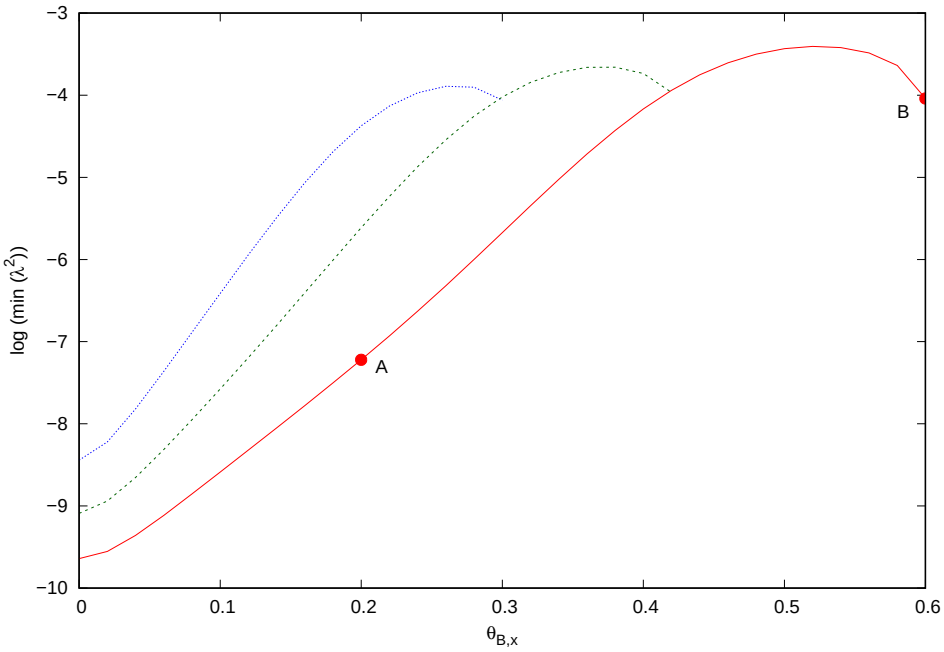

Figure 4.4: Minimum eigenvalue, $log(\lambda^2)$, versus boundary temperature $\theta_{B,x}$ for the (1+1)-D steady state solitary wave. Shown are $\mu = 1.0$: red (solid) line; $\mu = 0.7$: green (dashed) line; $\mu = 0.5$: blue (dotted) line.

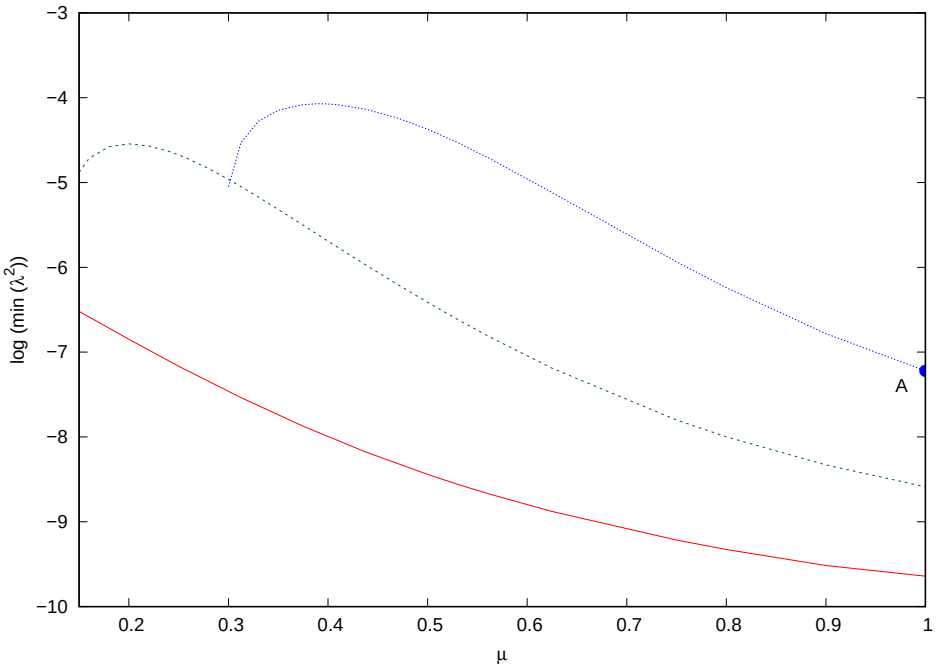

Figure 4.5: Minimum eigenvalue, $\log(\lambda^2)$, versus propagation constant μ for the (1+1)-D steady state solitary wave. Shown are $\theta_{B,x} = 0$: red (solid) line; $\theta_{B,x} = 0.1$: green (dashed) line; $\theta_{B,x} = 0.2$: blue (dotted) line.

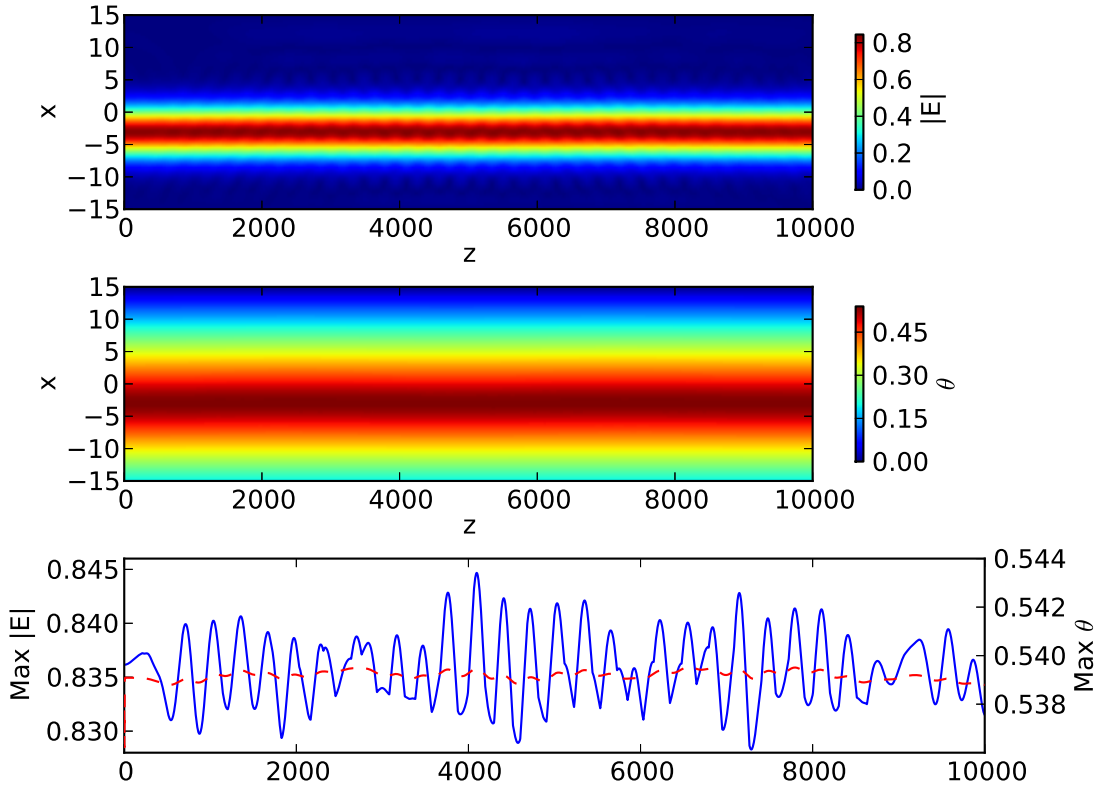

Figure 4.6: Electric field amplitude, $|E|$, and temperature, θ, in the (x, z) plane, as given by the full numerical solution of the thermal system (1.25), up to $z = 10000$. The parameters are $\mu = 1.0$ and $\theta_{B,x} = 0.2$. Upper panel: $|E|$; Middle panel: θ; Lower panel: Maximum value of $|E|$ blue (solid) line and θ red (dashed) line.

on Figure 4.4, so the spectral analysis has a positive eigenvalue for this case, which implies stability. The theoretical prediction of stability is again consistent with the numerical solution.

Figure 4.8 shows the electric field amplitude, $|E|$, and temperature, θ, in the (x, z) plane. Shown is the numerical evolution of a perturbed solitary wave for z up to 10000. The parameters are $\theta_{B,x} = 0.2$ and $\mu = 0.28$. The initial thermal solitary wave corresponds to a non-symmetric excited state. For this example, the electric field amplitude has two peaks, one of $|E| = 0.222$ at $x = -4.36$ and the other peak of $|E| = 0.187$ nearer to the boundary at $x = -11.76$. It is of interest to determine whether excited state thermal solitary waves are numerically stable, as excited state solitary waves tend to be unstable, particularly for local equations [62].

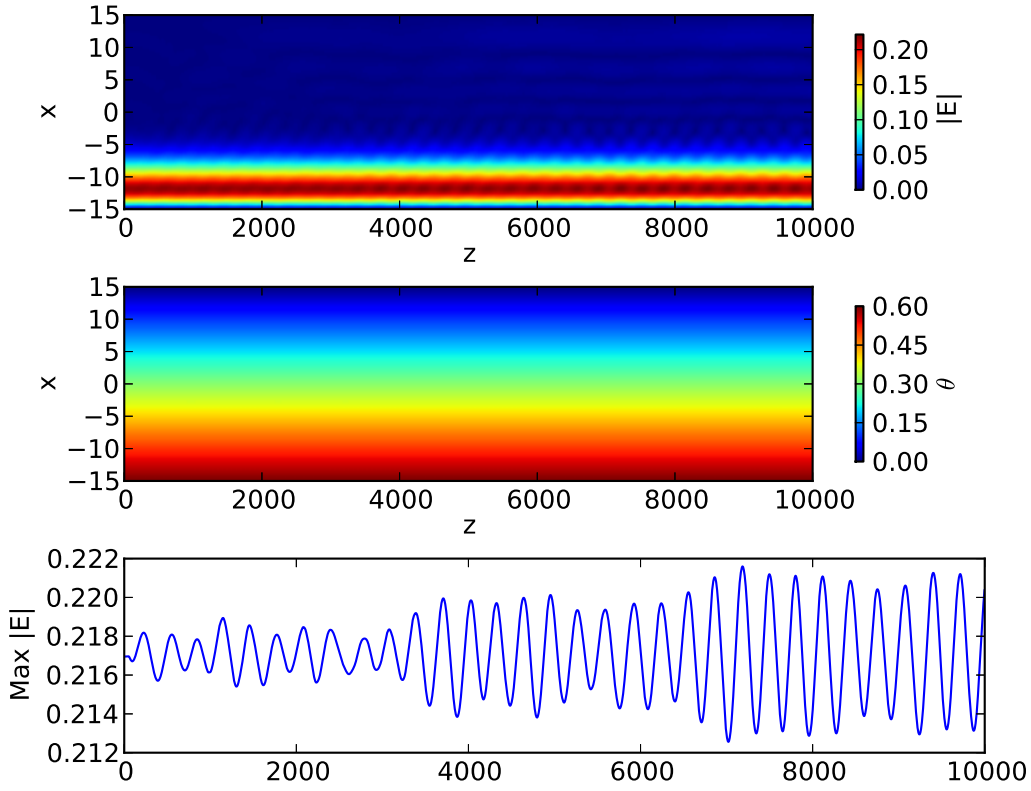

Figure 4.7: Electric field amplitude, $|E|$, and temperature, θ, in the (x, z) plane, as given by the full numerical solution of the thermal system (1.25), up to $z = 10000$. The parameters are $\theta_{B,x} = 0.6$ and $\mu = 1.0$. Upper panel: $|E|$; Middle panel: θ; Lower panel: Maximum value of $|E|$ blue (solid) line).

The maximum value reached for the larger peak is $|E| = 0.224$, with a variation of around 1%, which indicates that it is stable to perturbations.

Note that although the evolution is shown in all these figures up to $z = 10000$, the initial conditions used were found to be stable for much longer z. Hence, the numerical results confirm that (1+1)-D thermal solitary waves are MS, even for higher-order waves and extremely non-symmetric cases, for which the wave is close to one cell boundary. For each of the fundamental solitary wave cases the numerical stability was also in agreement with the finding of stability implied by positive eigenvalues in the spectral stability analysis and positive slope of the power versus propagation constant curves.

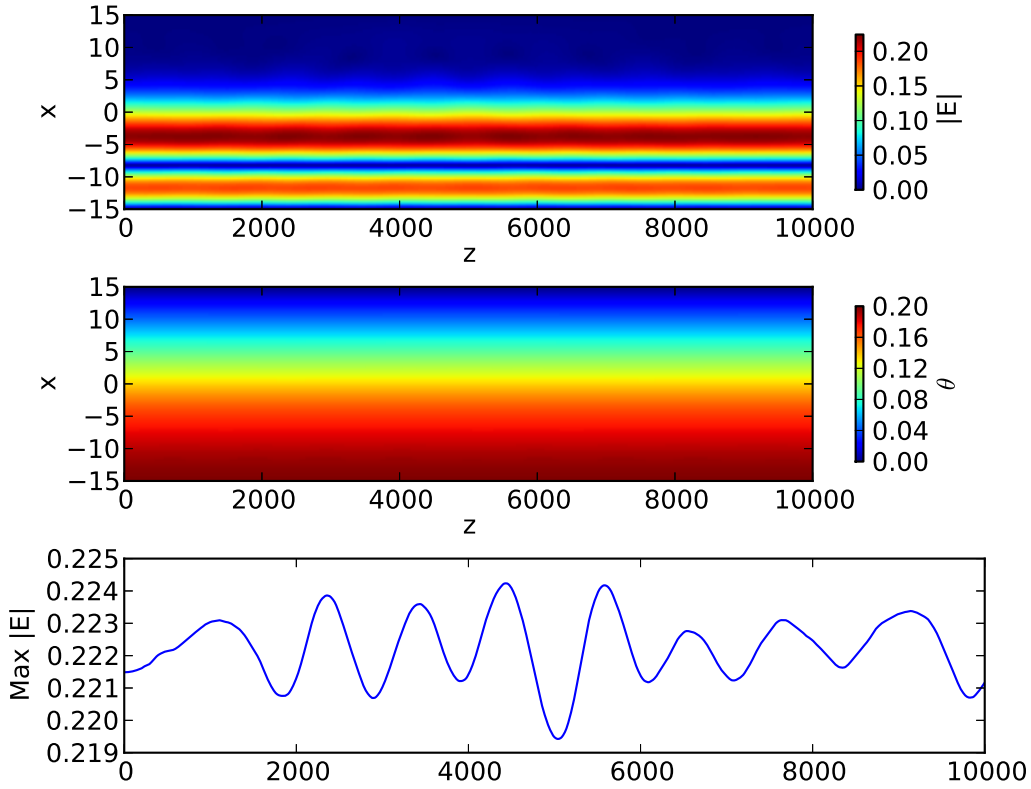

Figure 4.8: Electric field amplitude, $|E|$, and temperature, θ, in the (x, z) plane, as given by the full numerical solution of the thermal system (1.25), up to $z = 10000$. The parameters are $\theta_{B,x} = 0.2$ and $\mu = 0.28$. Upper panel: $|E|$; Middle panel: θ; Lower panel: Maximum value of $|E|$ blue (solid) line.

4.3 (2+1)-D System Stability

Figure 4.9a shows the power P versus propagation constant μ for ground state thermal solitary waves in (2+1)-D. The three curves correspond to $\theta_{B,y} = 0$, 0.2 and 0.4. For non-zero ambient temperature $\theta_{B,y}$ the solitary wave solution branch only exists over a finite range of μ. All three curves are monotonic with positive slope indicating that, for a given value of the ambient temperature, there is a single stable solution branch. Figure 4.9b shows the power P versus propagation constant μ for ground and excited state thermal solitary waves for $\theta_{B,y} = 0.2$. The three curves correspond to the ground state and the first two excited states. In all three cases the curves are monotonic with positive slope, fulfilling the necessary condition for MS across the entire range of μ values for both the ground and excited state solitary

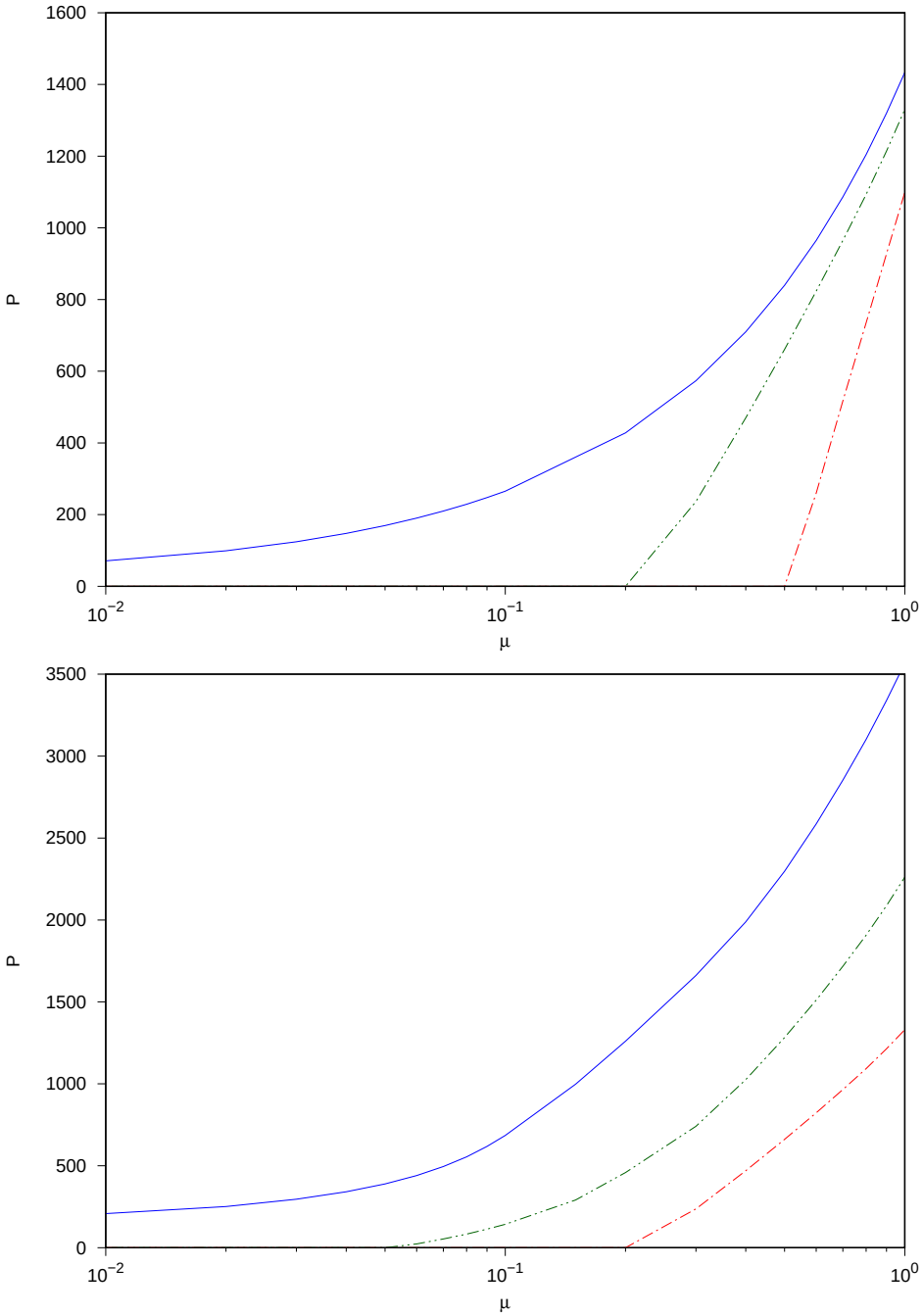

Figure 4.9: a) Power, P, versus propagation constant μ, for (2+1)-D ground state thermal solitary waves. Shown are $\theta_{B,y} = 0$: blue (solid) line; $\theta_{B,y} = 0.2$: green (dash-dot-dot) line; $\theta_{B,y} = 0.4$: red (dash-dot) line. b) Power, P, versus propagation constant, μ, for (2+1)-D ground and excited state thermal solitary waves with $\theta_{B,y} = 0.2$. Ground state wave: red (dash-dot) line; first excited state: green (dash-dot-dot) line; second excited state: blue (solid) line.

waves.

Figure 4.10(a) shows the minimum eigenvalue, $\log(|\lambda^2|)$, versus $\theta_{B,y}$ for (4.10). Shown are $\mu = 0.5, 0.7$ and 1. Figure 4.10(b) shows amplitude a versus $\theta_{B,y}$, with stable region shown as solid line and the unstable region shown as dashed lines. The symbols A, B, C and D refer to the parameter choices used for Figures 4.12, 4.13, 4.14 and 4.15 respectively. In the case $\mu = 1.0$, the smallest eigenvalue is negative for values of $\theta_{B,y}$ up to 0.175, after which all the eigenvalues are positive. For the case $\mu = 0.5$ the eigenvalues are positive for all values of $\theta_{B,y}$ up to 0.5, suggesting stability for $\theta_{B,y}$ in this range. For $\mu = 0.7$ the threshold value for the sign change of the minimum eigenvalue is $\theta_{B,y} = 0.075$, with stability for large values of $\theta_{B,y}$. The figures show that higher amplitude solitary waves are generally unstable while lower amplitude waves are generally stable. Increasing $\theta_{B,y}$ stabilizes the solitary waves, as the amplitudes are lower for off-centred waves, while increasing μ destabilizes the waves, as their amplitude increases.

Figure 4.11(a) shows the minimum eigenvalue, $\log(|\lambda^2|)$, versus propagation constant μ for (4.10). Figure 4.11(b) shows the amplitude versus μ for (4.10). Shown are $\theta_{B,y} = 0.0, 0.05$ and 0.1. The symbols A, B, C and D refer to the parameter choices used for Figures 4.12, 4.13, 4.14 and 4.15 respectively. The solitary wave is not stable for larger values of the propagation constant, indicating that regions of parameter space corresponding to large amplitude solitary waves are unstable, according to linearized stability analysis. To assess whether the negative eigenvalue is associated with an amplitude stability or a drift instability it is necessary to check whether the associated eigenmode is symmetric or asymmetric [54]. In this case the negative eigenvalues possess a symmetric eigenmode, indicating that for values of $\mu > 0.55$ the solitary wave possesses an amplitude instability. For values of $\mu < 0.55$ the solitary wave is stable.

Figure 4.12 shows the electric field amplitude, $|E|$, and temperature, θ, in the (y, z) plane, as given by the full numerical solution of the thermal equations (1.15) with boundary conditions (1.19)–(1.22), with a profile taken along the $x = 0$ axis. Shown is the numerical evolution of a perturbed solitary wave, for z up to 4000. The parameters are $\theta_{B,x} = \theta_{B,y} = 0.0$ and $\mu = 1$. The initial thermal solitary wave corresponds to the symmetric case in Figure 3.7. The thermal solitary wave is

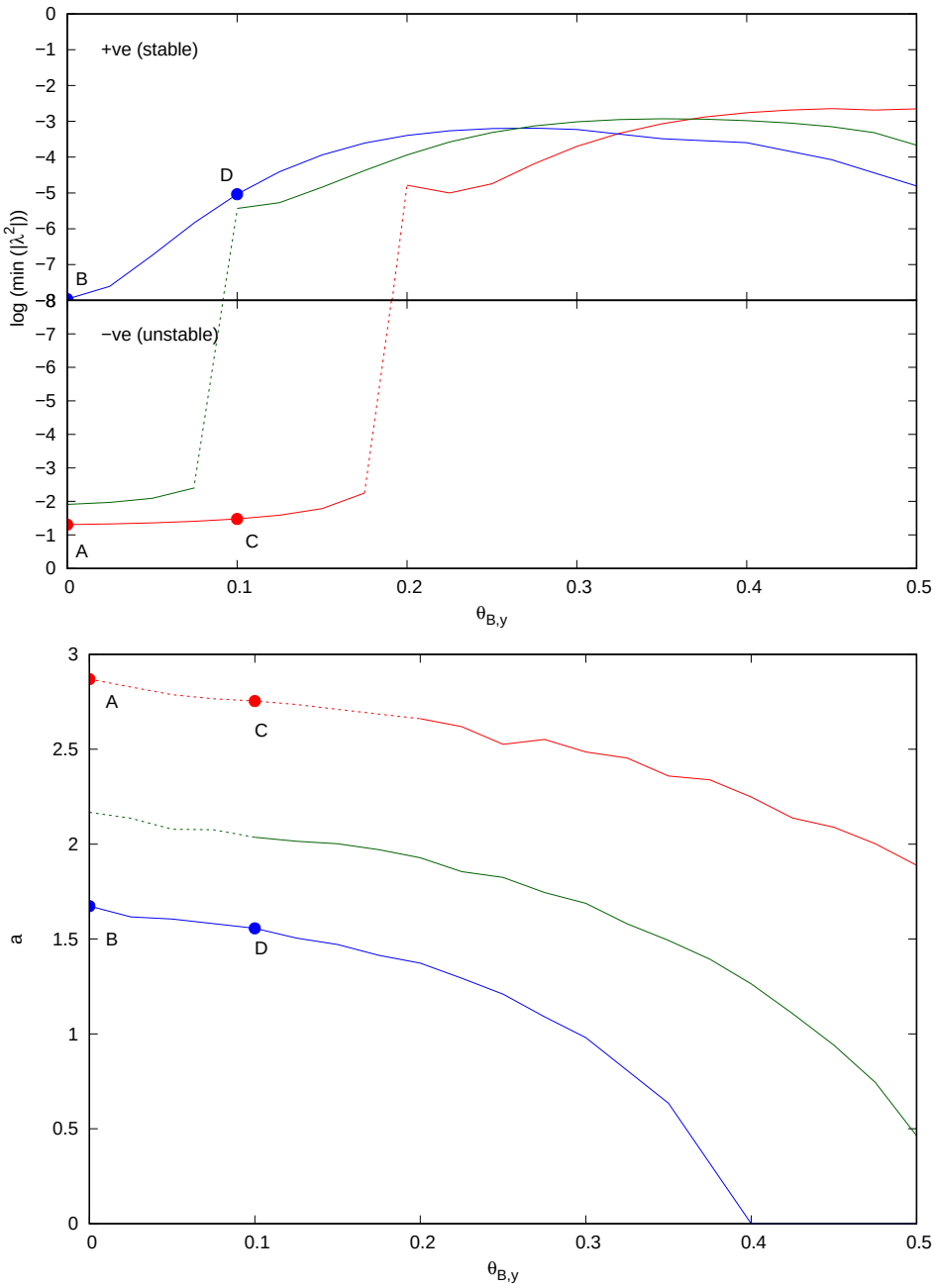

Figure 4.10: a) Minimum eigenvalue, plotted as $\log(|\lambda^2|)$, versus $\theta_{B,y}$ for Equation 4.10. Shown are $\mu = 1.0$: red (right) line; $\mu = 0.7$: green (middle) line; and $\mu = 0.5$: blue (left) line. The dashed red line shows the discontinuity where the minimum eigenvalue changes sign. b) Amplitude, a, versus $\theta_{B,y}$, with stable region shown as solid line and the unstable region shown as dashed lines. Shown are $\mu = 1.0$: red (top) line; $\mu = 0.7$: green (middle) line; and $\mu = 0.5$: blue (bottom) line

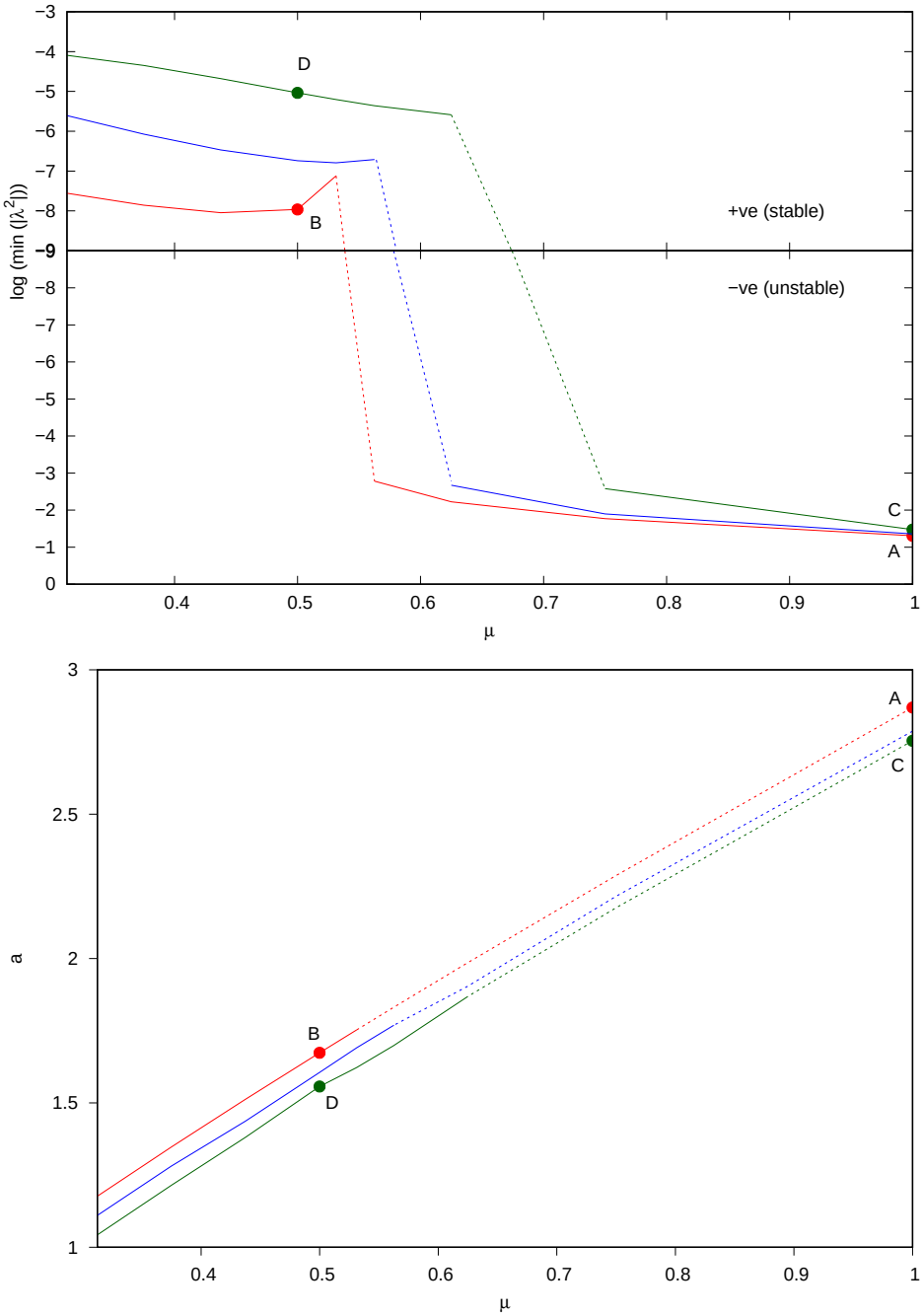

Figure 4.11: a) Minimum eigenvalue, plotted as $\log(|\lambda^2|)$, versus μ for Equation 4.10. Shown are $\theta_{B,y} = 0.0$: red (left) line; $\theta_{B,y} = 0.05$: blue (middle) line; $\theta_{B,y} = 0.1$: green (right) line. b) Amplitude, a, versus μ, with stable region shown as solid line and the unstable region shown as dashed lines. Shown are $\theta_{B,y} = 0.0$: red (top) line; $\theta_{B,y} = 0.05$: blue (middle) line; $\theta_{B,y} = 0.1$: green (bottom) line.

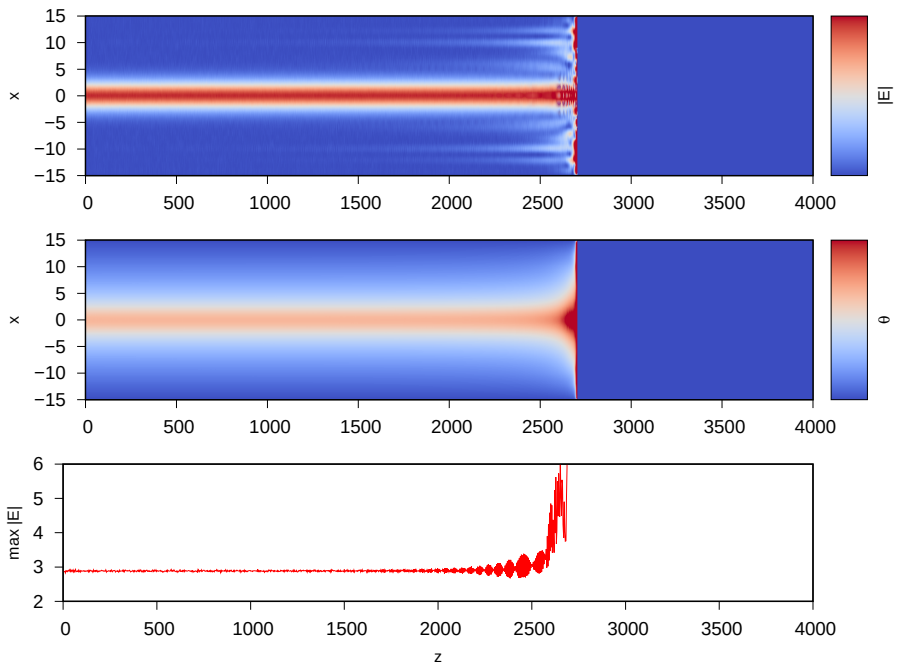

Figure 4.12: Time evolution of centred thermal solitary wave, demonstrating amplitude modulational instability. Shown are $|E|$ (top), and θ (middle) both taken along y = 0, along with the maximum value of $|E|$ (bottom) from $z = 0$ to $z = 4000$. The parameters are $\theta_{B,y} = 0$ and $\mu = 1.0$.

initially a ground state beam centred on $(x, y) = (0, 0)$ with an amplitude of $a = 2.86$. Instability develops from around $z = 2000$, before the numerical solution breaks down completely after around $z = 2500$. This example corresponds to the parameter choices marked A on Figures (4.10) and (4.11), so the spectral stability analysis in this case has a negative eigenvalue, which implies instability. The theoretical prediction of a slow rate of amplitude drift instability is consistent with the numerical solutions.

Figure 4.13 shows the electric field amplitude, $|E|$, and temperature, θ, in the (y, z) plane, as given by the full numerical solution of the thermal equations (1.15) with boundary conditions (1.19)–(1.22), with a profile taken along the $x = 0$ axis, for the case $\mu = 0.5$. This represents a case where all the eigenvalues are positive (see Figure 4.11, for $\mu = 0.5$). Shown is the numerical evolution of a perturbed solitary wave, for z up to 6000. The parameters are $\theta_{B,x} = \theta_{B,y} = 0$ and $\mu = 1$. The initial thermal solitary wave corresponds to the symmetric case in Figure 3.7. In this case the thermal solitary wave is a ground state beam centred on $(x, y) = (0, 0)$ with an amplitude of $a = 1.68$, with the solitary wave remaining stable until at least

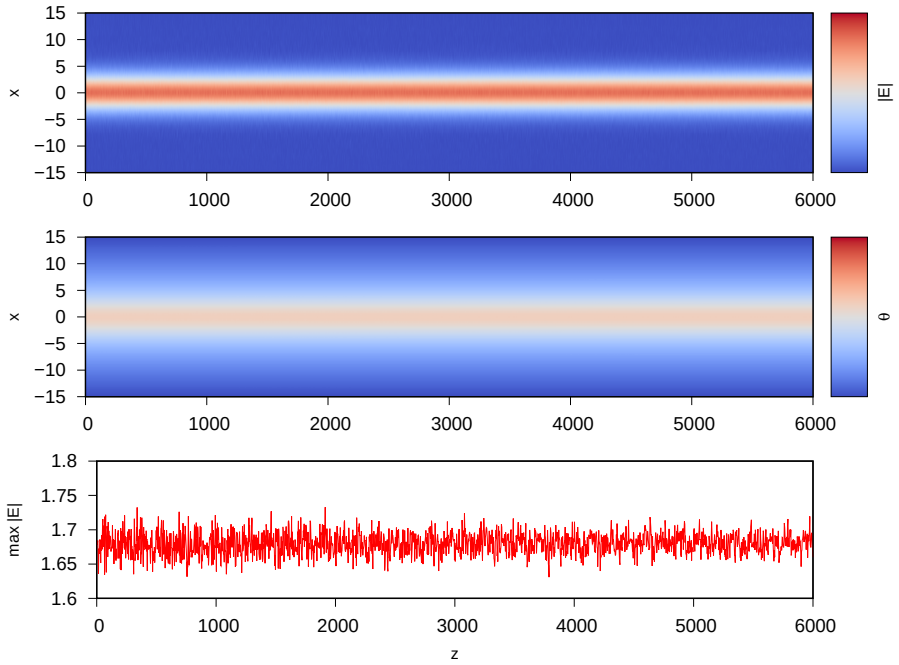

Figure 4.13: Time evolution of centred thermal solitary wave, demonstrating stability of the solution. Shown are $|E|$ (top), and θ (middle) both taken along y = 0, along with the maximum value of $|E|$ (bottom) from $z = 0$ to $z = 6000$. The parameters are $\theta_{B,y} = 0$ and $\mu = 0.5$.

$z = 6000$. This example corresponds to the parameter choices marked B on Figures 4.10 and 4.11, so the spectral analysis in this case has a positive minimum eigenvalue which implies stability. The theoretical prediction of stability is consistent with the numerical solution.

Figure 4.14 shows the electric field amplitude, $|E|$, and temperature, θ, in the (y, z) plane, as given by the full numerical solution of the thermal equations (1.15) with boundary conditions (1.19)–(1.22), with a profile taken along the $x = 0$ axis. The other parameters are $\theta_{B,y} = 0.1$ and $\mu = 1$. The thermal solitary wave solution is a ground state beam off-centred on $(x, y) = (0, -3)$ with an amplitude $a = 2.7$. Instability develops from around $z = 600$, before the numerical solution breaks down completely after $z = 800$. This example corresponds to the parameter choices marked C on Figures 4.10 and 4.11, so the spectral analysis in this case has a negative minimum eigenvalue which implies instability, which is consistent with the numerical solutions.

Figure 4.15 shows the electric field amplitude, $|E|$, and temperature, θ, in the (y, z) plane, as given by the full numerical solution of the thermal equations (1.15)

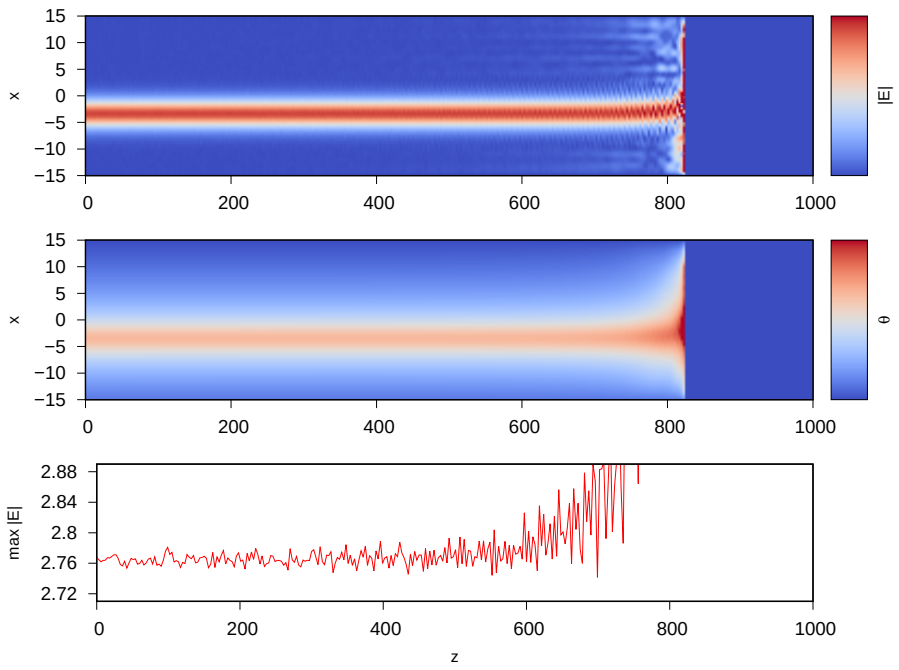

Figure 4.14: Time evolution of off-centre thermal solitary wave, demonstrating instability of the solution. Shown are $|E|$ (top), and θ (middle) both taken along y = 0, along with the maximum value of $|E|$ (bottom) from $z = 0$ to $z = 1000$. The parameters are $\theta_{B,y} = 0.1$ and $\mu = 1.0$.

with boundary conditions (1.19)–(1.22), with a profile taken along the $x = 0$ axis. The parameters are $\theta_{B,y} = 0.1$ and $\mu = 0.5$. The thermal solitary wave solution is a ground state beam off-centred on $(x, y) = (0, -6.18)$ with an amplitude of $a = 1.55$. Here the beam is much closer to the boundary than the example considered in Figure 4.14. For this case, no instability develops by $z = 2000$, although it seems from the plot of $\max|E|$ that instability is beginning to develop by $z = 2500$ for this off-centre case. This example corresponds to the parameter choices marked D on Figures 4.10 and 4.11, so the spectral stability analysis in this case has a positive minimum eigenvalue which implies stability. The correspondence between the theoretical stability prediction and the numerical solutions is not clear cut. Whilst this example exhibits numerical stability for a much longer $z \approx 3000$ than does Figure 4.14 (which exhibits instability at $z \approx 700$), numerical instability does eventually develop. This instability may be numerical, and due to difficulties in a propagating off-centred wave, or perhaps an influence from the boundary, not captured in our stability analysis.

It is known that stable higher order solitary waves are possible in (2+1)-D geo-

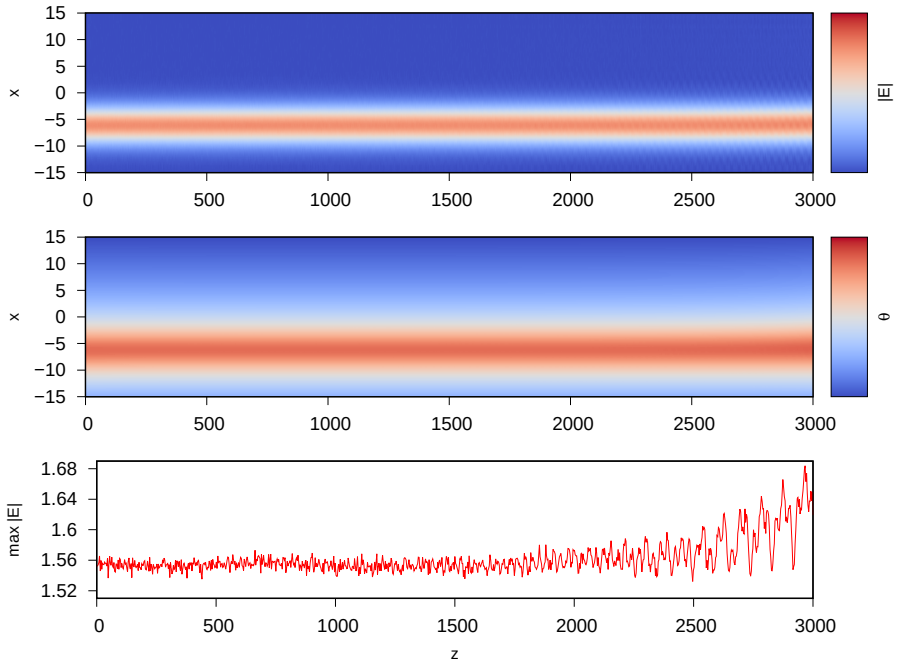

Figure 4.15: Time evolution of off-centre thermal solitary wave, demonstrating stability of the solution. Shown are $|E|$ (top), and θ (middle) both taken along y = 0, along with the maximum value of $|E|$ (bottom) from $z = 0$ to $z = 3000$. The parameters are $\theta_{B,y} = 0.1$ and $\mu = 0.5$.

metry for many NLS-type equations, where nonlocality permits a broad enough waveguide. Figure 4.16 shows a higher order steady solitary wave solution with electric field amplitude, $|E|$, and temperature, θ, in the (y, z) plane, given by the full numerical solution of the thermal equations (1.15) with boundary conditions (1.19)–(1.22), with a profile taken along the $x = 0$ axis (upper panels in Figure 3.13). The parameters are $\theta_{B,x} = \theta_{B,y} = 0$ and $\mu = 0.1$. The solitary wave initially has a local maximum at the centre and an annular local minimum, which translates to three local maxima of $|u|$ along the cross section at $y = 0$. After around $z = 500$ the higher order solitary wave decays to a ground state solitary wave with amplitude of $a = 1.41$ and a variation of around 1.3%, consistent with the behaviour expected for solitary waves with topological charge ≥ 3 [57]. The ground state wave propagates stably until at least $z = 12000$ (not shown).

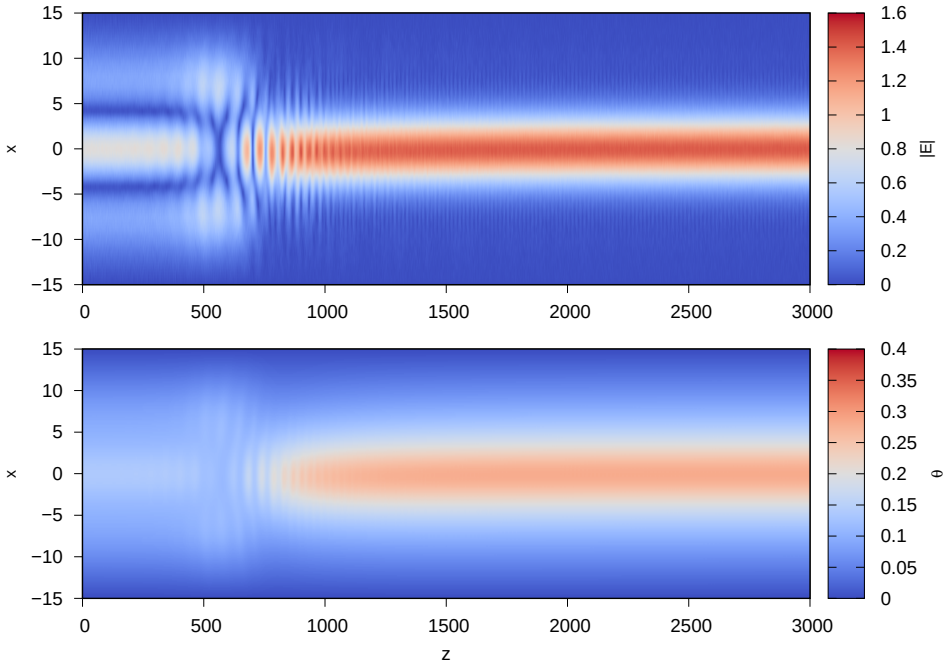

Figure 4.16: Time evolution of higher order thermal solitary wave, demonstrating decay into ground state solitary wave and subsequent stability. Shown are $|E|$ (top), and θ (bottom) both taken along y $= 0$ from $z = 0$ to $z = 3000$. The parameters are $\theta_{B,y} = 0$ and $\mu = 0.1$.

Chapter 5

Conclusions and Future Work

In this thesis we have considered optical solitary waves propagating through a nonlinear thermal medium, for both a line (1+1)-D cell geometry and a square (2+1)-D cell geometry.

We have compared the performance of three different numerical schemes for finding steady-state thermal solitary wave solutions. We found that the Newton-CG method can be used to efficiently find the steady state solitary waves, including cases where one or more of the cell boundaries is kept warmer than the ambient temperature. We explored several options for implementation of the Newton-CG scheme, including the order of the spatial discretizations and the use of preconditioning matrices, and found that a fourth-order discretization with no preconditioning produced the best results. The Newton-CG method was shown to be able to produce higher order solitary waves in both (1+1)-D and (2+1)-D.

The solutions derived in this thesis show that the location of an optical beam within a cell migrates towards the warmer boundaries, and can be guided towards the corner of the cell when more than one adjacent boundary is kept warm. Solitary waves closer to the cell boundary tend to be lower in amplitude, in both the (1+1)-D and (2+1)-D cases, and there was a limit to how close to the cell boundary a solitary wave could be supported. Control of the solitary wave location via the warm boundary can be achieved by either changing the ambient temperature at the boundary or via a scenario with different Biot numbers at the boundaries, as in the steady state a lower Biot number also produces a higher temperature at the cell boundary. Excited state solitary waves also migrated towards the warmer boundary

or boundaries, but experienced changes in the geometric structure of the electric field in the (2+1)-D case.

It was shown that both (1+1)-D and (2+1)-D solitary waves met the VK criterion for stability in the parameter space that we explored. As the VK stability criterion is only a necessary condition for stability we also conducted a spectral stability analysis, finding that the (1+1)-D thermal solitary waves are stable for all parameter values, and that (2+1)-D waves are stable for some combinations of boundary temperature and propagation constant. We checked these theoretical stability results by comparing with the numerical evolution of perturbed solitary waves, finding agreement with the theoretical results in most cases.

There are many opportunities to extend the work of this thesis. We could investigate steady state solitary wave solutions for

- Defocussing thermal media. The propagation of stable solitary waves in defocussing thermal media have been studied experimentally, e.g. [51, 107, 108]. This will generate families of dark and grey thermal solitary waves and we can explore how these respond to different conditions at the cell boundary, and whether these forms of solitary wave are stable in both (1+1)-D and (2+1)-D geometries.

- Circular cell geometry including vortex modes. This would produce (2+1)-D solitary waves with radial symmetry, where the governing equation could be reduced from a function in three variables (x, y, z) to a function in two variables (r, z) though a variable transformation, e.g. [59]. While differential temperature at the boundary may not be experimentally practical, we can investigate the effect of boundary temperature and propagation constant on the stability of the solitary waves in this geometry.

- Rectangular cell geometry to calculate elliptical thermal solitary wave solutions, as found experimentally by [97], and the effect of differential temperature at the cell boundaries on these elliptical waves. We could also investigate other irregular cell geometries to find the effect on the form of the solitary wave.

- Other higher order solitary waves, including multipole types. e.g. [28] showed

the effect of the boundary on non-steady state dynamics of quadrupole necklace solitary waves. We could explore whether the Newton-CG method can produce thermal solitary waves of this form, and the effect of differential temperature of the cell boundaries.

In addition, further work is needed to investigate the sources of numerical errors propagating in from the cell boundaries, as we have been unable to completely resolve discrepancies arising between the spectral and numerical stability analyses in some off-centred (2+1)-D cases. In this thesis we have used the fact that information from the boundary conditions is present in the steady state solution to undertake the spectral stability analysis, but it may be worth investigating ways to explicitly incorporate the boundary condition in this stability analysis. It would be of value to calculate gain curves for modulational instabilities to better understand this mode of instability in the off-centred case.

Another future component of work could be to identify candidate experimental regimes, including details such as the type of thermal media and configuration at the cell boundary, in which the boundary temperature effects identified in this thesis could be tested.

This work, and suggested associated future work, may have direct applications for experiments into the control and steering of light beams in photonic devices, including experiments in optical switching and optical computing systems.

Bibliography

[1] A.B. Aceves, J.V. Moloney and A.C. Newell. "Theory of light-beam propagation at nonlinear interfaces. I. Equivalent-particle theory for a single interface". In: *Phys. Rev. A* 39.4 (1989), pp. 1809–1827.

[2] J.S. Aitchison, A.M. Weiner, Y. Silberberg, M.K. Oliver, J.L. Jackel, D.E. Leaird, E.M. Vogel and P.W.E. Smith. "Observation of spatial optical solitons in a nonlinear glass waveguide". In: *Opt. Lett.* 15.9 (1990), pp. 471–473.

[3] N.N. Akhmediev, M.J. Lederer and B. Luther-Davies. "Exact localized solution for nonconservative systems with delayed nonlinear response". In: *Phys. Rev. E* 57.3 (1998), pp. 3664–3667.

[4] S.A. Akmanov, A.P. Sukhurukov and R.V. Khokhlov. "Self-focussing and self-trapping of intense light beams in a nonlinear medium". In: *Sov. Phys. JETP* 23.6 (1966), pp. 1025–1033.

[5] A. Alberucci and G. Assanto. "Propagation of optical spatial solitons in finite-size media: interplay between nonlocality and boundary conditions". In: *J. Opt. Soc. Am. B* 24 (2007), pp. 2314–2320.

[6] A. Alberucci, G. Assanto, D. Buccoliero, A. Desyatnikov, T.R. Marchant and N.F Smyth. "Modulation analysis of boundary-induced motion of optical solitary waves in a nematic liquid crystal". In: *Phys. Rev. A* 79.043816 (2009).

[7] A. Alberucci, C.P. Jisha, N.F. Smyth and G. Assanto. "Spatial optical solitons in highly nonlocal media". In: *Phys. Rev. A* 91.013841 (2015).

[8] A. Alberucci, M. Peccianti and G. Assanto. "Nonlinear bouncing of nonlocal spatial solitons at the boundaries". In: *Opt. Lett.* 32 (2007), pp. 2795–2797.

[9] B. Alfassi, C. Rotschild, O. Manela, M. Segev and D. Christodoulides. "Boundary force effects exerted on solitons in highly nonlocal media". In: *Opt. Lett.* 32 (2007), pp. 154–156.

[10] D. Anderson. "Variational approach to nonlinear pulse propagation in optical fibers". In: *Phys. Rev. A* 27.6 (1983), pp. 3135–3145.

[11] A. Ashkin, J.M. Dziedzic and P.W. Smith. "Continuous-wave self-focusing and self-trapping of light in artificial Kerr media". In: *Opt. Lett.* 7.6 (1982), pp. 276–278.

[12] G.A. Askar'yan. "Cerenkov radiation and transition radiation from electromagnetic waves". In: *Sov. Phys. JETP* 15.5 (1962), pp. 943–946.

[13] G. Assanto, T.R. Marchant, A.A. Minzoni and N.F. Smyth. "Reorientational versus Kerr dark and grey solitary waves using modulation theory". In: *Phys. Rev. E.* 84.6 (2011).

[14] G. Assanto, M. Peccianti and C. Conti. "Nematicons: Optical Spatial Solitons in Nematic Liquid Crystals". In: *Optics and Photonics News* 14.2 (2003), pp. 44–48.

[15] O. Bang, Y.S. Kivshar, A.V. Buryak, A. De Rossi and S. Trillo. "Two-dimensional solitary waves in media with quadratic and cubic nonlinearity". In: *Phys. Rev. E* 58.4 (1998), pp. 5057–5069.

[16] O. Bang, W. Krolikowski, J. Wyller and J. Rasmussen. "Collapse arrest and soliton stabilization in nonlocal nonlinear media". In: *Phys. Rev. E* 66.4 (2002).

[17] C. Barsi, W. Wan, C. Sun and J. Fleischer. "Dispersive shock waves with nonlocal nonlinearity". In: *Opt. Lett.* 32 (2007), pp. 2930–2932.

[18] R. Bekenstein and M. Segev. "Self-accelerating optical beams in highly nonlocal nonlinear media". In: *Opt. Exp.* 19.24 (2011), pp. 23706–23715.

[19] T.B. Benjamin. "Instability of periodic wavetrains in nonlinear dispersive systems". In: *Proc. Roy. Soc. A* 299.1456 (1967), pp. 59–76.

[20] T.B. Benjamin and J.E. Feir. "The disintegration of wave trains on deep water. Part 1. Theory". In: *J. Fluid Mech.* 27.3 (1967), pp. 417–430.

[21] V.I. Bespalov and V.I. Talanov. "Filamentary structure of light beams in nonlinear liquids". In: *ZhETF Pis'ma* 3.11 (1966), pp. 471–476.

[22] J. Bezanson, A. Edelman, S. Karpinski and V.B. Shah. "Julia: A Fresh Approach to Numerical Computing". In: *SIAM Rev.* 59.1 (2017), pp. 65–98.

[23] A. Bezryadina, T. Hansson, R. Gautam, B. Wetzel, G. Siggins, A. Kalmbach, J. Lamstein, D. Gallardo, E.J. Carpenter, A. Ichimura, R. Morandotti and Z. Chen. "Nonlinear self-action of light through biological suspensions". In: *Phys. Rev. Lett.* 119.058101 (2017).

[24] J. Boussinesq. "Théorie de l'intumescence appelée onde solitaire ou de translation se propageant dans un canal rectangulaire". In: *Comptes Rendus* 72 (1871), pp. 755–759.

[25] J. P. Boyd. "Why Newton's method is hard for travelling waves: Small denominators, KAM theory, Arnold's linear Fourier problem, non-uniqueness, constraints and erratic failure". In: *Math. Comput. Simul.* 74.2-3 (2007), pp. 72–81.

[26] E. Braun, L.P. Faucheux and A. Libchaber. "Strong self-focussing in nematic liquid crystals". In: *Phys. Rev. A* 48.1 (1993), pp. 611–622.

[27] D. Briedis, D.E. Petersen, D. Edmundson, W. Krolikowski and O. Bang. "Ring vortex solitons in nonlocal nonlinear media". In: *Opt. Exp.* 13.2 (2005), pp. 435–443.

[28] D. Buccoliero, A. Desyatnikov, W. Krolikowski and Y.S. Kivshar. "Boundary effects on the dynamics of higher-order optical spatial solitons in nonlocal thermal media". In: *J. Opt. A: Pure Appl. Opt.* 11.094014 (2009).

[29] D. Buccoliero, S. Lopez-Aguayo, S. Skupin, A. Desyatnikov, O. Bang, W. Krolikowski and Y.S. Kivshar. "Spiraling solitons and multipole localized modes in nonlocal nonlinear media". In: *Phys. B* 394.2 (2007), pp. 351–356.

[30] R.L. Carman, A. Mooradian, P.L. Kelley and A. Tufts. "Transient and steady state thermal self-focusing". In: *Appl. Phys. Lett.* 14.4 (1969), pp. 136–139.

[31] Z. Chen, M. Mitchell, M. Segev, T.H. Coskun and D.N. Christodoulides. "Self-trapping of dark incoherent light beams". In: *Science* 280.5365 (1998), pp. 889–892.

[32] R.Y. Chiao, E. Garmire and C.H. Townes. "Self trapping of optical beams". In: *Phys. Rev. Lett.* 13.15 (1964), pp. 479–482.

[33] M.C. Chiofalo, S. Succi and M.P. Tosi. "Ground state of trapped interacting Bose-Einstein condensates by an explicit imaginary-time algorithm". In: *Phys. Rev. E* 62.5 (2000), pp. 7438–7444.

[34] C. Conti, A. Fratalocchi, M. Peccianti, G. Ruocco and S. Trillo. "Observation of a Gradient Catastrophe Generating Solitons". In: *Phys. Rev. Lett.* 102.083902 (2009).

[35] C. Conti, M. Peccianti and G. Assanto. "Observation of optical spatial solitons in a highly nonlocal medium". In: *Phys. Rev. Lett.* 92.113902 (2004).

[36] C. Conti, M. Peccianti and G. Assanto. "Route to nonlocality and observation of accessible solitons". In: *Phys. Rev. Lett.* 91.073901 (2003).

[37] F.W. Dabby and J.R. Whinnery. "Thermal self-focusing of laser beams in lead glasses". In: *Appl. Phys. Lett.* 13.8 (1968), pp. 284–286.

[38] A.S. Desyatnikov, A.A. Sukhorukov and Y.S. Kivshar. "Azimuthons: Spatially modulated vortex solitons". In: *Phys. Rev. Lett.* 20.20 (95), p. 203904.

[39] J.R. Douglas and H.H. Rachford. "On the numerical solution of heat conduction problems in two and three space variables". In: *Trans. Amer. Math. Soc.* 82.2 (1956), pp. 421–439.

[40] A. Dreischuh, G.G. Paulus, F. Zacher, F. Grasbon and H. Walther. "Generation of multiple-charged optical vortex solitons in a saturable nonlinear medium". In: *Phys. Rev. E.* 60.5 (1999), pp. 6111–6117.

[41] G. Duree, J.L. Shultz, G. Salamo, M. Segev, A. Yariv, B. Crosignani, P. DiPorto, E. Sharp and R.R. Neurgaonkar. "Observation of self-trapping of an optical beam due to the photorefractive effect". In: *Phys. Rev. Lett.* 71.4 (1993), pp. 533–536.

[42] R.H. Enns, S.S. Rangnekar and A.E. Kaplan. "Bistable-soliton pulse propagation: stability aspects". In: *Phys. Rev. A* 36.3 (1987), pp. 1270–1279.

[43] R.H. Enns, S.S. Rangnekar and A.E. Kaplan. "Robust bistable solitons of the highly nonlinear Shrodinger equation". In: *Phys. Rev. A.* 35.1 (1987), pp. 466–469.

[44] L. Fousse, G. Hanrot, V. Lefevre, P. Pelissier and P. Zimmermann. "MPFR: A multiple precision binary floating-point library with correct rounding". In: *ACM Trans. Math. Softw.* 33.2 (2007).

[45] N. Ghofraniha, C. Conti, G. Ruocco and S. Trillo. "Shocks in Nonlocal Media". In: *Phys. Rev. Lett.* 99.043903 (2007).

[46] V.L. Ginzburg and L.P. Pitaevskii. "On the theory of superfluidity". In: *Sov. Phys. JETP* 34.5 (1958), pp. 858–861.

[47] L.P. Gor'kov. "Microscopic derivation of the Ginzburg-Landau equations in the theory of superconductivity". In: *Sov. Phys. JETP* 39.6 (1959), pp. 1364–1367.

[48] A.H. Guth, M.P. Hertzberg and C. Prescod-Weinstein. "Do dark matter axions form a condensate with long-range correlation?" In: *Phys. Rev. D* 92.10 (2015), p. 103513.

[49] J.P. Hansen and I.R McDonald. *Theory of simple liquids*. London: Academic Press, 1976. ISBN: 012323851X.

[50] A. Hasegawa and F. Tappert. "Transmission of stationary nonlinear optical pulses in dispersive dielectric fibres. I. Anomalous dispersion". In: *App. Phys. Lett.* 23.3 (1973), pp. 142–144.

[51] A. Hasegawa and F. Tappert. "Transmission of stationary nonlinear optical pulses in dispersive dielectric fibres. II. Normal dispersion". In: *App. Phys. Lett.* 23.4 (1973), pp. 171–172.

[52] C. Huang. "Propagation of coupled dipole-mode beams in nonlocal thermal media". In: *Opt. Commun.* 284.24 (2011), pp. 5786–5791.

[53] X. Hutsebaut, C. Cambournac, M. Haelterman, A. Adamski and K. Neyts. "Single-component higher-order mode solitons in liquid crystals". In: *Opt. Commun.* 233.1-3 (2004), pp. 211–217.

[54] B. Ilan, Y. Sivan and G. Fibich. "A quantitative approach to soliton instability". In: *Opt. Lett.* 36.3 (2011), pp. 397–399.

[55] Y. Izdebskaya, G. Assanto and W. Krolikowski. "Observation of stable-vector vortex solitons". In: *Opt. Lett.* 40.17 (2015), pp. 4182–4185.

[56] A.E. Kaplan. "Bistable Solitons". In: *Phys. Rev. Lett.* 55.12 (1985), pp. 1291–1294.

[57] Y.V. Kartashov, V.A. Vysloukh and L. Torner. "Stability of vortex solitons in thermal nonlinear media with cylindrical symmetry". In: *Opt. Exp.* 15.15 (2007), pp. 9378–9384.

[58] W.L. Kath and N.F. Smyth. "Soliton evolution and radiation loss for the nonlinear Schrodinger equation". In: *Phys. Rev. E* 51.2 (1995), pp. 1484–1492.

[59] P.L. Kelley. "Self-focusing of optical beams". In: *Phys. Rev. Lett.* 15.26 (1965), pp. 1005–1008.

[60] R.K. Khokhlov. "On nonlinear wave processes". In: *Sov. Phys. Usp.* 8.5 (1966), pp. 642–645.

[61] I. Khoo. *Liquid Crystals*. 2nd ed. Pure and Applied Optics. Hoboken, New Jersey: John Wiley and Sons, 2007. ISBN: 978-0-471-75153-3.

[62] Y.S. Kivshar and G. Agrawal. *Optical Solitons: From Fibers to Photonic Crystals*. San Diego. Academic, 2003.

[63] Y.S. Kivshar and B. Luther-Davies. "Dark Optical Solitons: Physics and Application". In: *Phys. Rep.* 298.2-3 (1998), pp. 81–197.

[64] W. Krolikowski, O. Bang, J.J. Rasmussen and J. Wyller. "Modulational instability in nonlocal nonlinear Kerr media". In: *Phys. Rev. E* 64.1 (2001).

[65] W. Krolikowski, C. Denz, A. Stepken, M. Saffman and B. Luther-Davies. "Interaction of spatial photorefractive solitons". In: *Quantum Semiclass. Opt.* 10.6 (1998), pp. 823–837.

[66] V.I. Kruglov. "Spiral self-trapping propagation of optical beams in media with a cubic nonlinearity". In: *Phys. Lett. A* 111.8-9 (1985), pp. 401–404.

[67] E. Kuznetsov, A. Rubenchik and V. Zakharov. "Soliton stability in plasmas and hydrodynamics". In: *Phys. Rep.* 142.3 (1986), pp. 103–165.

[68] P. Lallemand and N. Bloembergen. "Self-focussing of laser beams and stimulated Raman gain in liquids". In: *Phys. Rev. Lett.* 15.26 (1965), pp. 1010–1012.

[69] W.M. Lee, El-Ganainy R., D.N. Chrisodoulides, K. Dholakia and E.M. Wright. "Nonlinear optical response of colloidal suspensions". In: *Opt. Exp.* 17.12 (2009), pp. 10277–10289.

[70] A.G. Litvak. "Self-focusing of powerful light beams by thermal effects". In: *Sov. Phys. JETP Lett.* 4 (1966), pp. 230–233.

[71] A.G. Litvak, V.A. Mironov, G.M. Fraiman and A.D. Yunakovskii. "Thermal self-effect of wave beams in a plasma with a nonlocal nonlinearity". In: *Fiz. Plazmy* 1 (1975), pp. 60–71.

[72] S.A. Louis, T.R. Marchant and N.F. Smyth. "2-D solitary waves in thermal media with non-symmetric boundary conditions". In: *Stud. Appl. Math.* (2018), pp. 1–22.

[73] S.A. Louis, T.R. Marchant and N.F. Smyth. "Optical solitary waves in thermal media with non-symmetric boundary conditions". In: *J. Phys. A.:Math. Theor.* 46.055201 (2013).

[74] S. Maneuf, R. Desailly and C. Froehly. "Stable self-trapping of laser beams: Observation in a nonlinear planar waveguide". In: *Opt. Comm.* 65.3 (1988), pp. 193–198.

[75] T.R. Marchant and N.F. Smyth. "Nonlocal validity of an asymptotic one dimensional nematicon solution". In: *J. Phys A.:Math. Theor.* 41.365201 (2008).

[76] T.R. Marchant and N.F. Smyth. "Solitary Waves and their stability in colloidal media: Semi-analytical solutions". In: *Dyn. Cont. Disc. Impul. Sys.* 19 (2012), pp. 525–541.

[77] M. Matuszewski, W. Krolikowski and Y.S. Kivshar. "Soliton interactions and transformations in colloidal media". In: *Phys. Rev. A* 79.023814 (2009).

[78] M. Matuszewski, W. Krolikowski and Y.S. Kivshar. "Spatial solitons and light-induced instabilities in colloidal media". In: *Opt. Exp.* 16.2 (2008), pp. 1371–1376.

[79] D.M. McLaughlin, D.J. Muraki, M.J. Shelley and X. Wang. "A paraxial model for optical self-focussing in a nematic liquid crystal". In: *Physica D* 88.1 (1995), pp. 55–81.

[80] A.A. Minzoni, L.W. Sciberras, N.F. Smyth and A.L. Worthy. "Propagation of optical spatial solitary waves in bias-free nematic-liquid-crystal cells". In: *Phys. Rev. A* 84.043823 (2011).

[81] A.A. Minzoni, N.F. Smyth and A.L. Worthy. "Modulation solutions for nematicon propagation in nonlocal liquid crystals". In: *J. Opt. Soc. Am. B* 24 (2007), pp. 1549–1556.

[82] A.A. Minzoni, N.F Smyth, A.L. Worthy and Y.S. Kivshar. "Stabilization of vortex solitons in nonlocal nonlinear media". In: *Phys. Rev. A* 76.063803 (2007).

[83] M. Mitchell, Z. Chen, M. Shih and M. Segev. "Self-trapping of partially spatially incoherent light". In: *Phys. Rev. Lett.* 77.3 (1996), pp. 490–493.

[84] M. Mitchell and M. Segev. "Self-trapping of incoherent white light". In: *Nature* 387.6636 (1997), pp. 880–883.

[85] L.F. Mollenauer, R.H. Stolen and J.P. Gordon. "Experimental observation of picosecond pulse narrowing and solitons in optical fibres". In: *Phys. Rev. Lett.* 45.13 (1980), pp. 1095–1098.

[86] S.O. Olsen. "Self-focussing and self-trapping of gravitational waves". In: *Nat. Phys. Science.* 238 (1972), pp. 12–13.

[87] A. Paredes and H. Michinel. "Interference of dark matter solitons and galactic offsets". In: *Phys. Dark Universe* 12 (2016), pp. 50–55.

[88] M. Peccianti and G. Assanto. "Nematicons". In: *Phys. Reports* 516.4-5 (2012), pp. 147–208.

[89] M. Peccianti, C. Conti and G. Assanto. "Optical modulational instability in a nonlocal medium". In: *Phys. Rev. E* 68.025602 (2003).

[90] M. Peccianti, C. Conti, G. Assanto, A. De Luca and C. Umeton. "Routing of anisotropic spatial solitons and modulational instability in liquid crystals". In: *Nature* 432.7018 (2004), pp. 733–737.

[91] M. Peccianti, A. Dyadyusha, M. Kaczmarek and G. Assanto. "Escaping solitons from a trapping potential". In: *Phys. Rev. Lett.* 101.15 (2008), p. 153902.

[92] M. Peccianti, A. Fratalocchi and G. Assanto. "Transverse dynamics of nematicons". In: *Opt. Exp.* 12.26 (2004), pp. 6524–6529.

[93] D.E. Pelinovsky and Y.A. Stepanyants. "Convergence of Petviashvili's Iteration method for numerical approximation of stationary solutions on nonlinear wave equations". In: *SIAM J. Numer. Anal.* 42.3 (2004), pp. 1110–1127.

[94] M. Quiroga-Teixeiro and H. Michinel. "Stable azimuthal stationary state in quintic nonlinear optical media". In: *J. Opt. Soc. Am. B* 14.8 (1997), pp. 2004–2009.

[95] P.D. Rasmussen, O. Bang and W. Krolikowski. "Theory of nonlocal soliton interaction in nematic liquid crystals". In: *Phys. Rev. E* 72.066611 (2005).

[96] C. Rotschild, B. Alfassi, O. Cohen and M. Segev. "Long-range interactions between optical solitons". In: *Nature Phys.* 2 (2006), pp. 769–774.

[97] C. Rotschild, O. Cohen, O. Manela, M. Segev and T. Carmon. "Solitons in nonlinear media with an infinite range of nonlocality: First observation of coherent elliptic solutions and vortex ring solutions". In: *Phys. Rev. Lett.* 95.213904 (2005).

[98] C. Rotschild, T. Schwartz, O. Cohen and M. Segev. "Incoherent spatial solitons in effectively instantaneous nonlinear media". In: *Nat. Photonics* 2 (2008), pp. 371–376.

[99] S. Russell. *Report on waves*. Tech. rep. York: Report on the fourteenth meeting of the British Association for the Advancement of Science, 1845.

[100] J. Satsuma and N. Yajima. "Initial value problems of one-dimensional self-modulation of nonlinear waves in dispersive media". In: *Prog. Theor. Phys. Supp.* 55 (1974), pp. 284–306.

[101] M. Segev, B. Crosignani, A. Yariv and B. Fischer. "Spatial solitons in photorefractive media". In: *Phys. Rev. Lett.* 68.7 (1992), pp. 923–926.

[102] S. Skupin, O. Bang, D. Edmundson and W. Krolikowski. "Stability of two-dimensional spatial solitons in nonlocal nonlinear media". In: *Phys. Rev. E* 73.6 (2006).

[103] N.F. Smyth and W.L. Kath. "Radiative losses due to pulse interactions in birefringent nonlinear optical fibres". In: *Phys. Rev. E* 63.036614 (2001).

[104] G.G. Stokes. "On the theory of oscillatory waves". In: *Trans. Cambridge Philosophical Society* 8 (1847), pp. 441–455.

[105] K.S. Strecker, G.B. Partridge, A.G. Truscott and R.G. Hulet. "Bright matter wave solitons in Bose-Einstein condensates". In: *New J. Phys.* 5.73 (2003).

[106] D. Suter and T. Blasberg. "Stabilization of transverse solitary waves by a nonlocal response of the nonlinear medium". In: *Phys. Rev. A* 48.6 (1993).

[107] G.A. Swartzlander, D.R. Andresen, J.J. Regan, H. Yin and A.E. Kaplan. "Spatial dark-soliton stripes and grids in self-defocusing materials". In: *Phys. Rev. Lett.* 66.12 (1991), pp. 1583–1586.

[108] W.J. Tomlinson, R.J. Hawkins, A.M. Weiner, J.P. Heritage and R.N. Thurston. "Dark optical solitons with finite-width background pulses". In: *J. Opt. Soc. Am. B* 6.3 (1989), pp. 329–334.

[109] N.G. Vakhitov and A.A. Kolokolov. "Stationary solutions of the wave equation in a medium with nonlinearity saturation". In: *Radiophys. Quantum El.* 16.7 (1973), pp. 783–789.

[110] E.V. Vanin, A.I. Korytin, A.M. Sergeev, D. Anderson, M. Lisak and L. Vazquez. "Dissipative optical solitons". In: *Phys. Rev. A* 49.4 (1994), pp. 2806–2811.

[111] G.B. Whitham. *Linear and nonlinear waves*. New York: J. Wiley and Sons, 1974.

[112] A. Yakimenko, Y. Zaliznyak and Y.S. Kivshar. "Stable vortex solitons in nonlocal self-focusing nonlinear media". In: *Phys. Rev. E* 71.065603 (2005).

[113] J. Yang. "Newton-conjugate-gradient methods for solitary wave computations". In: *J. Comp. Phys.* 228.18 (2009), pp. 7007–7024.

[114] J. Yang and T.I. Lakoba. "Accelerated imaginary-time evolution methods for the computation of solitary waves". In: *Stud. Appl. Math.* 120.3 (2008), pp. 265–292.

[115] J. Yang and T.I. Lakoba. "Universally-convergent squared operator iteration methods for solitary waves in general nonlinear wave equations". In: *Stud. Appl. Math.* 118.2 (2007), pp. 153–197.

[116] V.E. Yashin, S.A. Chizhov, R.L. Sabirov, T.V. Starchikova, Vysotina N.V., N.N. Rozanov, V.E. Semenov, V.A. Smirnov and S.V. Fedorov. "Formation of soliton-like light beams in an aqueous suspension of polystyrene particles". In: *Opt. Spectrosc.* 98.3 (2005), pp. 466–469.

[117] V.E. Zakharov. "Stability of periodic waves of finite amplitude on a surface of deep fluid". In: *J. Appl. Mech. Tech. Phy.* 9.2 (1968), pp. 190–194.

[118] V.E. Zakharov and A.B. Shabat. "Exact theory of two-dimensional self-focusing and one-dimensional self-modulation of waves in nonlinear media". In: *Sov. Phys. JETP* 34.1 (1972), pp. 62–69.

[119] V.E. Zakharov and A.B. Shabat. "Interaction between solitons in a stable medium". In: *Zh. Eksp. Teor. Fiz.* 64 (1973), pp. 1627–1639.

Appendix

A Selected Code

Python code demonstrating the implementation of the Newton-CG method for the (1+1)-D case is included below. The file *fourthOrder.py* contains the main program loop for implementing the fourth order discretized version of the Newton-CG method. The file *conjGradOperators.py* contains operators for performing the conjugate gradient solver, interpolating to find amplitude and location, and calculation of one dimensional power. The file *fourthOrderOperators.py* contains constructors for the fourth order $L0$ and $L1$ operators. The file *parameters.py* contains key parameters governing the cell geometry, boundary conditions, and numerical methods.

```
##
## Filename: fourthOrder.py
##

from numpy import exp,copy,zeros,arange,dot
import matplotlib
matplotlib.use('agg')
import pylab as pl
from time import time

import _fourthOrderOperators
import _conjGradOperators
from _parameters import Lx,Nx,dx,nmax,errormax,beta, \
                        thetaB,mu,filename,errorfilename
```

```
# Function to call fourth order discretized Newton-CG solver
def simulation():
    st = time()
    x=arange(-Lx/2,-Lx/2+Nx*dx,dx)

    # Initial guess for steady state solution
    E=2.0*exp(-x**2)
    Theta=1.8*exp(-x**2)
    Einit=copy(E)
    Thetainit=copy(Theta)
    Eerror=zeros(nmax)

    # Outside (Newton) iteration loop
    for nn in arange(1,nmax):
        Eold = copy(E)
        Thetaold = copy(Theta)

        L1=_fourthOrderOperators.L1(Eold,Thetaold,Nx, \
                                    dx,beta,thetaB,mu)
        L0E=_fourthOrderOperators.L0(Eold,Thetaold,Nx, \
                                    dx,beta,thetaB,mu)
        L0E=dot(L1.T,L0E)
        L1=dot(L1.T,L1)

        # Inner (conjugate gradient) iteration loop
        DX=_conjGradOperators.solver(L0E,L1)
        E=Eold+DX[0:Nx]
        Theta=Thetaold+DX[Nx:2*Nx]

        # Check error
        Eerror[nn]=abs(DX[2:2*Nx-2]).max()
```

```
        if Eerror[nn] < errormax:
            print "Iterations= ",nn
            break
    P=_conjGradOperators.power(E,dx)

    ft = time()
    print "Time Taken= " ,(ft-st)/60.0," mins"
    return x,E,Theta,Einit,Thetainit,Eerror,P

# Run with custom parameters
def simulation_p(beta,thetaB,mu,errormax,Nx,Ein,Tin):
    st = time()
    dx=Lx/(Nx-1)
    x=arange(-Lx/2,-Lx/2+Nx*dx,dx)

    # Initial guess for steady state solution
    E=Ein
    Theta=Tin
    Einit=copy(E)
    Thetainit=copy(Theta)
    Eerror=zeros(nmax)

    # Outside (Newton) iteration loop
    for nn in arange(1,nmax):
        Eold = copy(E)
        Thetaold = copy(Theta)

        L1=_fourthOrderOperators.L1(Eold,Thetaold,Nx, \
                                    dx,beta,thetaB,mu)
        L0E=_fourthOrderOperators.L0(Eold,Thetaold,Nx, \
                                    dx,beta,thetaB,mu)
        L0E=dot(L1.T,L0E)
```

```
        L1=dot(L1.T,L1)

        # Inner (conjugate gradient) iteration loop
        DX=_conjGradOperators.solver(L0E,L1)
        E=Eold+DX[0:Nx]
        Theta=Thetaold+DX[Nx:2*Nx]

        # Check error
        Eerror[nn]=abs(DX[2:2*Nx-2]).max()
        if Eerror[nn] < errormax:
            break
    P=_fourthOrderOperators.Sint(E*E)

    ft = time()
    print "Time Taken= ",(ft-st),"seconds"
    return x,E,Theta,Einit,Thetainit,Eerror,P

##
## Filename: conjGradOperators.py
##

# Conjugate Gradient Iteration Solver
from numpy import zeros, dot, arange
from numpy.linalg import inv

def solver(L0E,L1):
    DX=zeros(len(L0E))
    R=-L0E
    Rerr=dot(R,R)
    Rerr0=Rerr
    D=R
    while(Rerr > 10e-2*Rerr0):
```

```
        q=dot(L1,D)
        a=Rerr/dot(D,q)
        DX=DX+a*D
        R=R-a*q
        RerrOld=Rerr
        Rerr=dot(R,R)
        b=Rerr/RerrOld
        D=R+b*D
    return DX

def midpointInterpolator(E,Nx):
    Midpoint=E.argmax()
    if (Midpoint-1)>=0 and (Midpoint+1)<=(Nx-1):
        X=(E[Midpoint]-E[Midpoint-1])/(E[Midpoint] \
            -E[Midpoint+1])
        if (E[Midpoint-1]>E[Midpoint+1]):
            Adjusted_Midpoint=Midpoint-0.5*(1-X)
        elif (E[Midpoint-1]<E[Midpoint+1]):
            Adjusted_Midpoint=Midpoint+0.5*(1-1/X)
        Adjusted_Midpoint=(Adjusted_Midpoint-Nx/2)
    elif (Midpoint-1)<0:
        Adjusted_Midpoint=-Nx/2
    else:
        Adjusted_Midpoint=Nx/2

    return Adjusted_Midpoint

def amplitudeInterpolator(x,v):
    Xc=v.argmax()
    if Xc<len(v)-1:
        mp=x[Xc]
        mpl=x[Xc-1]
```

```
            mpr=x[Xc+1]
            A=[[mpl**2,mpl,1],[mp**2,mp,1],[mpr**2,mpr,1]]
            b=[v[Xc-1],v[Xc],v[Xc+1]]
            pcoeff=dot(inv(A),b)
            xmax=-pcoeff[1]/(2*pcoeff[0])
            ymax=pcoeff[0]*xmax**2+pcoeff[1]*xmax+pcoeff[2]
        else:
            xmax=x[Xc]
            ymax=v[Xc]
        return xmax,ymax

def power(f,dx):
    f2=f**2
    mtot=f2[0]+f2[len(f)-1]
    for i in arange(1,len(f2)/2-1):
        mtot+=2*f2[i*2]+4*f2[i*2-1]
    mtot=mtot*dx/3.0
    return mtot

##
## Filename: fourthOrderOperators.py
##

from numpy import zeros, arange, hstack, vstack, \
                  dot, shape, diag,tril,triu
from numpy.linalg import inv, eig
from _parameters import nu,beta,dx


#  Conjugate Gradient operators
# Define fourth order nonlinear operator L0
def L0(E,T,Nx,dx,beta,thetaB,mu):
```

```
ETnew=zeros(2*Nx)

for i in arange(2,Nx-2):
    ETnew[i]=(-E[i-2]+16*E[i-1]-30*E[i]+ \
              6*E[i+1]-E[i+2])/(24*dx**2)+ \
              2*E[i]*T[i]-mu*E[i]
    ETnew[i+Nx]=nu*(-T[i-2]+16*T[i-1]- \
              30*T[i]+16*T[i+1]-T[i+2]) \
               /(12*dx**2)+2*abs(E[i])**2

ETnew[0]=E[0]
ETnew[1]=(10*E[0]-15*E[1]-4*E[2]+14*E[3]- \
         6*E[4]+E[5])/(24*dx**2)+2*E[1]*T[1] \
         -mu*E[1]
ETnew[Nx-2]=(E[Nx-6]-6*E[Nx-5]+14*E[Nx-4]- \
              4*E[Nx-3]-15*E[Nx-2]+10*E[Nx-1]) \
              /(24*dx**2)+2*E[Nx-2]*T[Nx-2] \
              -mu*E[Nx-2]
ETnew[Nx-1]=E[Nx-1]

ETnew[Nx]=(-3*T[4]+16*T[3]-36*T[2]+48*T[1] \
           -25*T[0])+12*beta*dx*(T[0]-thetaB)
ETnew[Nx+1]=nu*(10*T[0]-15*T[1]-4*T[2]+ \
              14*T[3]-6*T[4]+T[5])/(12*dx**2) \
              +2*abs(E[1])**2
ETnew[2*Nx-2]=nu*(T[Nx-6]-6*T[Nx-5]+14*T[Nx-4] \
              -4*T[Nx-3]-15*T[Nx-2]+10*T[Nx-1]) \
              /(12*dx**2)+2*abs(E[Nx-2])**2
ETnew[2*Nx-1]=T[Nx-1]

return ETnew
```

```
# Define fourth order linearized operator L1
def L1(E,T,Nx,dx,beta,thetaB,mu):
    L1=zeros([2*Nx,2*Nx])
    L1[0,0]=1
    L1[1,0]=10/(24*dx**2)
    L1[1,1]=-15/(24*dx**2)
    L1[1,2]=-4/(24*dx**2)
    L1[1,3]=14/(24*dx**2)
    L1[1,4]=-6/(24*dx**2)
    L1[1,5]=1/(24*dx**2)
    L1[Nx-2,Nx-6]=1/(24*dx**2)
    L1[Nx-2,Nx-5]=-6/(24*dx**2)
    L1[Nx-2,Nx-4]=14/(24*dx**2)
    L1[Nx-2,Nx-3]=-4/(24*dx**2)
    L1[Nx-2,Nx-2]=-15/(24*dx**2)
    L1[Nx-2,Nx-1]=10/(24*dx**2)
    L1[Nx-1,Nx-1]=1
    L1[Nx,Nx]=12*beta*dx-25
    L1[Nx,Nx+1]=48
    L1[Nx,Nx+2]=-36
    L1[Nx,Nx+3]=16
    L1[Nx,Nx+4]=-3
    L1[Nx+1,Nx]=10*nu/(12*dx**2)
    L1[Nx+1,Nx+1]=-15*nu/(12*dx**2)
    L1[Nx+1,Nx+2]=-4*nu/(12*dx**2)
    L1[Nx+1,Nx+3]=14*nu/(12*dx**2)
    L1[Nx+1,Nx+4]=-6*nu/(12*dx**2)
    L1[Nx+1,Nx+5]=nu/(12*dx**2)
    L1[2*Nx-2,2*Nx-6]=nu/(12*dx**2)
    L1[2*Nx-2,2*Nx-5]=-6*nu/(12*dx**2)
    L1[2*Nx-2,2*Nx-4]=14*nu/(12*dx**2)
    L1[2*Nx-2,2*Nx-3]=-4*nu/(12*dx**2)
```

```
    L1[2*Nx-2,2*Nx-2]=-15*nu/(12*dx**2)
    L1[2*Nx-2,2*Nx-1]=10*nu/(12*dx**2)
    L1[2*Nx-1,2*Nx-1]=1
    for i in arange(2,Nx-2):
        L1[i,i-2]=-1/(24*dx**2)
        L1[i,i-1]=16/(24*dx**2)
        L1[i,i]=-30/(24*dx**2)+2*T[i]-mu
        L1[i,i+1]=16/(24*dx**2)
        L1[i,i+2]=-1/(24*dx**2)
        L1[i,i+Nx+2]=2*E[i]
    for i in arange(Nx+2,2*Nx-2):
        L1[i,i-2]=-nu/(12*dx**2)
        L1[i,i-1]=nu*16/(12*dx**2)
        L1[i,i]=-30*nu/(12*dx**2)
        L1[i,i+1]=nu*16/(12*dx**2)
        L1[i,i+2]=-nu/(12*dx**2)
        L1[i,i-Nx-2]=4*E[i-Nx-2]

    return L1

# Define Simpsons numerical integration function
def Sint(f):
    mtot=f[0]+f[len(f)-1]
    for i in arange(1,len(f)/2-1):
        mtot+=2*f[i*2]+4*f[i*2-1]
    mtot=mtot*dx/3.0
    return mtot

##
## Filename: parameters.py
##
```

```
# Set up domain and parameters
Lx=30.0
Nx=90.0
nu=100
mu=0.05
beta=100.0
thetaB=0.0
errormax=1e-10
nmax=500000
dx=Lx/(Nx-1)

#Used in ITMs only
dt=0.005
c=1.5

#Fifth order Richardson extrapolation amplitude
re5=0.83425010458
```